State Estimation and Wave Excitation Force Estimation and Prediction for Wave Energy Converters Using Extended Kalman Filters

Andrew F. Davis

A dissertation
submitted in partial fulfillment of the
requirements for the degree of

Doctor of Philosophy

University of Washington

2020

Reading Committee:

Brian C. Fabien, Chair

Joseph Garbini

Santosh Devasia

Program Authorized to Offer Degree:
Mechanical Engineering

University of Washington

Abstract

State Estimation and Wave Excitation Force Estimation and Prediction for Wave Energy Converters Using Extended Kalman Filters

Andrew F. Davis

Chair of the Supervisory Committee:
Professor Brian C. Fabien
Mechanical Engineering

The analysis and control of ocean Wave Energy Converters (WECs) requires time domain models that often lack certainty. In many advanced control strategies, the wave excitation force is key to determining the control input. However, it is often difficult to measure the excitation force acting on a WEC. The use of Kalman filters to estimate the wave excitation force based on readily available measurement data can potentially fill the gap between the development of WEC control strategies and the data that is available. This work attempts to reduce the barriers to WEC deployments through validating methods of estimating and predicting the wave excitation force and through the development of systematic methods of system identification for WECs.

An extended Kalman filter (EKF) is implemented for observing the dynamic states and estimating the viscous drag coefficient of a heaving WEC float in irregular waves. Numerical data was generated to recreate the conditions of a wave tank test performed on a 1:10 scale wave energy conversion system to validate the identification of the viscous drag coefficient. Three lumped parameter models were evaluated for use in the EKF. A systematic estimate of the process noise covariance based on the steady state response of the heaving object and the incident wave was implemented.

The EKF is then applied to experimental wave tank data for a heaving semi-submerged

float to assess the ability of the Kalman filter to estimate wave excitation force. Two different estimation methods are described. The first method relies on directly including the excitation force as a state in the first order dynamics—which allows the "random walk" of the Kalman filter to identify an estimate of the excitation force. The second method of estimation involves modeling the wave excitation force as a harmonic oscillator comprised of sinusoidal components. Both methods are evaluated for a variety of incident waves and additional sensitivity analyses are performed to investigate the susceptibility of these estimation methods to changes in the model, measurement noise, and sampling rate.

Autoregressive methods are utilized to predict the wave excitation force through the use of estimated wave excitation force data, since they can be implemented in real time to adapt to changing conditions. The two models evaluated in this work are AutoRegressive (AR) and AutoRegressive with eXogenous inputs (ARX) models, which describes the wave propagation between two devices. The EKF incorporated nonlinear heave models of each body to estimate the wave excitation force, which was formulated as a harmonic disturbance to each system.

The drag identification and state observation capabilities of an extended Kalman are shown to be effective with limited sampled data and imperfect estimations of the process noise covariance. Some simplified models are shown to be effective if only state identification is needed, but a detailed model is needed for parameter identification. With the use of a sufficiently detailed model the EKF is shown to be able to identify a time varying drag coefficient of a semi-submerged floating object. The autoregressive excitation force prediction methods are evaluated for a variety of incident waves and additional sensitivity analyses are performed to investigate the susceptibility of these estimation methods to changes in the model, measurement noise, and sampling rate. The combination of the EKF and the autoregressive models presents an opportunity to evaluate the prediction capabilities of what can be currently implemented on board WECs in real time. Therefore, there is no need for of-

fline training or post-processed filtering of the incident wave. The ARX model incorporating excitation force data from other deployed bodies (the exogenous input) is shown to significantly improve the performance of the wave excitation force prediction. It is concluded that WECs in a wave farm may be able to improve their energy harvesting performance through enhancing their prediction capabilities by using wave estimation data gathered from other WECs.

Major contributions of this work include: experimental validations of various WEC models, implementation of a nonlinear Kalman filter with WEC models, and the experimentally validated estimation and prediction of the wave excitation force using methods that can be implemented on a deployed WEC.

TABLE OF CONTENTS

LIST OF FIGURES

LIST OF TABLES

ACKNOWLEDGMENTS

I would like to express my gratitude to all of the people who have made this thesis possible. First I would like to thank my advisor Brian Fabien for his guidance and training throughout my time at the University of Washington. With his patient advising I have been able to grow more as a researcher, teacher, and person than I thought possible to do in graduate school. He was particularly flexible to support me when I accepted a faculty position at LeTourneau University before my doctorate was complete.

I would like to thank my committee members, Joseph Garbini, Santosh Devasia, and Behçet Açikmeşe, who were willing to sacrifice their time to give me feedback on my research and teaching. Thank you as well to the many faculty members and students of the University of Washington Mechanical Engineering Department. Thank you to Brett Bosma for making your wave tank test data available to the public. I would like to particularly thank John Kramlich who gave me the opportunity to teach.

Thank you to the faculty and staff of LeTourneau University for your support of my research, teaching, and investment into the lives of students. Thank you Nathan Green for the discussions of stochastic processes. To the LeTourneau students, thank you so much for warmly accepting me as Mr. Davis while I teach you and finish my own studies at the same time. To the search committee that hired me, thank you for giving me the opportunity to do my dream job while I still finish the qualifications to be hired for it.

Thank you to my family for the support, care, and prayers throughout this process. Thank you to my parents for the years of encouragement, training, and patience that you have given me throughout my education. Thank you sharing your faith in God with me and helping me to continually grow. Without this faith I certainly would not finish this degree.

Josué, thank you for going through classes with me, being a research sounding board, and getting me kick started into estimation theory. Thank you for sharing grad school with Brisa and I. Countless hours, studying for class, playing Dominion, and exploring Seattle will always be fond memories. Thank you to my son Nathan and my daughter Ava your smiles and unconditional love has greatly helped me through many hard days of research.

Lastly, I would like to express my gratitude to my wife Brisa, for always being there with me through this long endeavor. The many conversations we have had hashing out details of my research on multiple whiteboards were both extremely helpful and a lot of fun. The support you have offered me has been invaluable, and I am honored to have been able to share this journey at UW with you.

DEDICATION

to my wife, Brisa

Chapter 1

INTRODUCTION

Ocean waves are a relatively underutilized source of renewable energy. Many coastal regions have high energy density waves that, if harvested, could be a significant renewable resource. Collecting energy from waves using a wave energy converter (WEC) was presented in literature during the ninteen-seventies by Stephen Salter [89]. While no single method of harvesting wave energy has become commercially viable there are currently many devices under development, as well as a significant amount of research done in the field of wave energy in recent years. Review publications intented to describe WEC technology, such as [70, 41, 25, 44], can provide an excellent foundation for understanding wave energy conversion. The upper bounds on the energy that can be converted from waves is analyzed in [43]. While the breadth of knowledge and technologies has become quite large, there are still fundamental barriers to WECs becoming commercially viable.

One such barrier is the implementation of WEC control systems. As WEC technology has developed so has the need for optimal control strategies [51]. Non linear model predictive control has become one of the most prominent control algorithms used in this field, offering optimal performance on a range of models over changing wave climates [40]. The need for state estimation has been pointed out in model predictive control literature [14], however there has been limited research actually dedicated to state estimation of WECs. The literature that does describe state estimation of WECs relies on simulation data where the exact process and measurement noises are known [64]. While it is possible to determine the measurement noise in a system it is often very difficult and potentially impossible to determine the process noise of a physical system [24]. To compound the issues of state estimation, it

is uncommon in the WEC industry to know the viscous drag coefficients of WEC bodies as they move through the water. To determine the drag coefficient the model is typically tuned after the device has been deployed. A numerical benchmarking study [8] states that when the drag coefficients were varied, presumably within a plausible range, device power production never vaired by more than 30%. This uncertainty in drag coefficient has also influenced code comparison projects and is shown to be vital to reduce non physical oscillations to enable WEC models to agree with each other [23]. As a result of drag coefficient uncertainty, experiments designed to determine WEC drag coefficients are a current area of research [17]. Chapter 4 of this work attempts to address these barriers to WEC applications.

Many optimal control algorithms rely on knowledge of the incident wave several seconds before the wave reaches the WEC [64]. The methods currently available in the literature to predict the incident wave do not appear to meet the needs of modern WEC control systems. Some preliminary work has been done to provide a prediction horizon sufficient for optimal control methods [46, 64], however to this date only a few seconds are available to a high level of certainty.

Chapter 1 of this work will describe a broad overview of wave energy conversion methods, models, and limitations of WEC development. The most common mechanisms by which WECs generate energy are discussed in section 1.1. A description of the various modeling methodologies for wave energy conversion systems are described in section 1.2. Particular emphasis is paid to the most widely applicable methods of modeling WECs. A description of the current state of WEC controls is given in section 1.3. This chapter is not sufficient for in depth study of wave energy conversion systems and control, however it provides a framework for understanding the contributions of this work in the context of the WEC field.

Chapter 2 presents a first principles model of a WEC deployed in Lake Washington. This work, "Modeling and Analysis of a Multi Degree of Freedom Point Absorber Wave Energy Converter", was published in the International Conference on Ocean, Offshore and Arctic Engineering [32]. The paper uses an experimentally validated model to perform a sensitivity analysis of the WEC design parameters on the power production of the WEC.

An analysis of the time domain forces acting on a heaving semi-submerged body is described in Chapter 3. The work of Chapter 3, "Modeling and Analysis of the Time Domain Forces of a Wave Energy Converter Model", was published in the Marine Energy Technology Symposium [29]. A comparison of the magnitude of the nonlinear viscous force and the radiated wave damping was given in [29] with comparisons making use of both experimental and analytical techniques in the accepted wave energy literature.

Chapter 4 presents a journal paper that attempts to address some of the factors that are impeding the successful deployment of optimally controlled WECs. The paper, "Systematic identification of drag coefficients for a heaving wave follower", published in the Journal of Ocean Engineering, provides several novel contributions to the observation and parameter estimation of WECs [30]. For the first time in the wave energy field a continuous-discrete extended Kalman filter is implemented to estimate the state dynamics and unknown drag coefficient. Several lumped parameter models are described, implemented and evaluated. The extended Kalman filter algorithm is modified to allow for an independent state space realization of the radiation force acting on the WEC. A novel systematic method of estimating the process noise covariance for a WEC model is described. Finally it is shown that with appropriate noise quantification and model choice a time-varying drag can be identified for a WEC. The contributions of this paper are aimed primarily at removing the barriers to a successful deployment of WECs while at the same time laying the groundwork for real time state estimation which is necessary for incident wave prediction.

The extended Kalman filters used in Chapter 4 are used for wave excitation force estimation in Chapter 5. The journal paper "Wave Excitation Force Estimation of Wave Energy Floats Using Extended Kalman Filters", published in the Journal of Ocean Engineering, makes use of data from a 1:10 scale wave tank study for evaluating mooring lines [31]. In this paper two different models to estimate the wave excitation force estimation capabilities of the extended Kalman filter for heaving semi-submerged objects. With the experimental results from [13] the method of this paper [31] is validated experimentally, then a sensitivity analysis is performed to evaluate the ability of the algorithm to handle changes in measure-

ment noise, sample rate, and model orders. This experimentally validated wave excitation force estimation provided the groundwork for a paper on the experimental validation of autoregressive models for wave excitation force prediction.

Chapter 6 presents a journal paper, which has been recommended for publication, that validates the use of autoregressive models for use in wave excitation force prediciton. The paper, "Wave excitation force prediction of a heaving wave energy converter", provides an experimental validation of methods that can be implemented in real-time on WECs. Evidence for the increased excitation force prediction capabilities of WECs is given by showing the performance improvement of autoregressive models that take into account prediction data from up-wave WECs.

Conclusions and discussion of this work is given in Chapter 7. Appendix A provides a more detailed description of the extended Kalman filter used in this work. While the extended Kalman filter used in this work is not an original creation, but rather well documented in [24], this appendix provides a description of the Kalman filter using notation consistent with this work.

1.1 Wave Energy Converters: Principles and Types

The wave energy conversion devices being studied in literature vary widely in their designs. Describing the many disparate WEC technologies as a whole requires a method of categorization. WECs can be classified by their location and orientation, the mechanism by which mechanical energy is converted to electrical energy, or, as done in this work, by the mechanical interaction with waves [43]. There are three primary categories of WECs: oscillating water columns, overtopping devices, and attenuators. Oscillating water columns rely on vertical motion of a column of water to drive a turbine. Overtopping devices trap water in a reservoir which is used to build a pressure head that can drive water in the resivoir through a turbine. Finally, attenuators rely on waves driving the motion of articulated components. A specific subset of attenuators, called point absorbers, are characterized by the facts that the relative motion of the components is primarily in heave and the characteristic dimension

of the device is much smaller than the wavelength of the incident wave. Benchmaking and review papers discussing the various WEC designs can be found in [63, 8].

1.1.1 Oscillating Water Columns

Oscillating water columns are typically large WECs that rely on trapping air in a compartment that is being pressurized by the rise and fall of a column of water. Figure 1.1 shows a cartoon of air being drawn in and forced out of a chamber by the amount of water in the chamber. The changing pressure due to waves at the water inlet drives the change in water level. The air chambers for oscillating water columns are typically large which necessitates that Osciating Water Columns are large WECs. In order to produce electricity during the entire cycle of operation electrical energy is drawn from the turbine when air is let in and forced out of the chamber. Oscillating water columns can be mounted to the shore or ocean floor as in the case of the iconic Limpet oscillating water column created by Wavegen [102]. Alternatively a floating oscillating water column is also possible as exemplifed by the Oceanlinx ocillating water column as shown in [4].

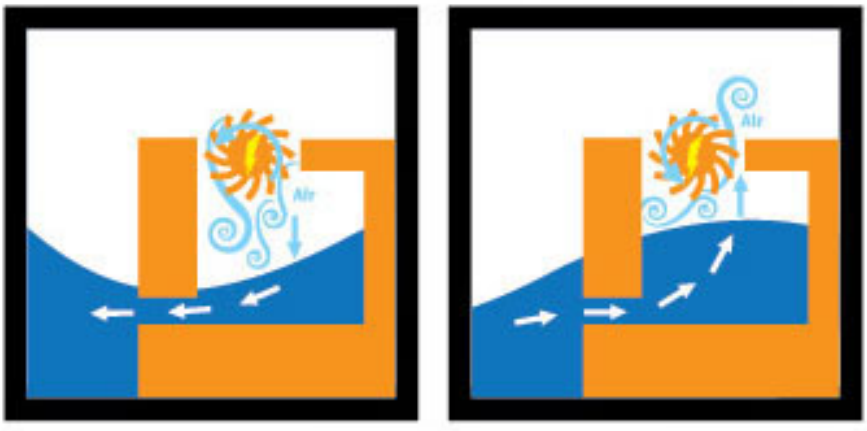

Figure 1.1: The main principle for oscillating water columns is to use the rise and fall of the water level to drive air through a turbine. [19].

1.1.2 Overtopping Devices

Overtopping devices rely on a partially submerged water reservoir that is filled with water with each passing wave. As water continues to fill the reservoir the pressure at the water outlet builds. This filling process converts the kinetic energy of the wave into potential energy which is then converted to electrical energy at the turbine located at the outlet of the resivoir. Figure 1.2 shows the flow of water into the reservoir and through an outlet that is below the mean water level. This mechanism provides the notable benefit that the power output is normalized by the fluid capacitance in the reservoir as such overtopping devices tend to suffer less from the power surges that plauge other wave energy conversion methods. The most notable example of an overtopping WEC is the Wave Dragon which utilizes a large surface area structure to focus waves towards its central reservoir [6].

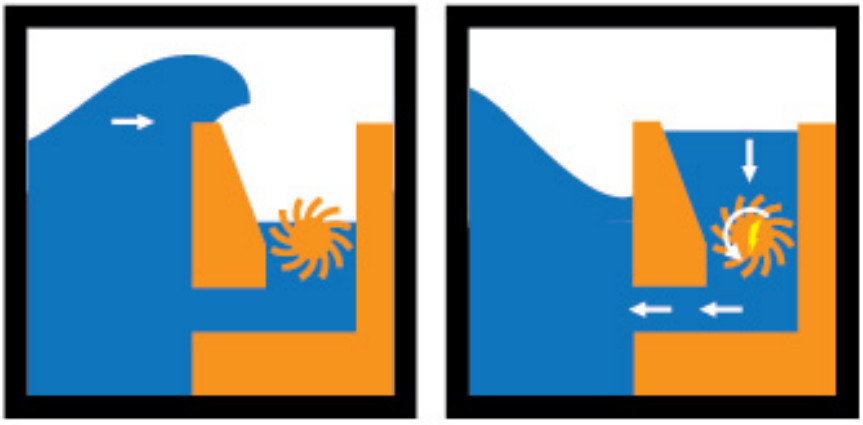

Figure 1.2: The main principle of an overtopping WEC is for the kinetic energy of waves to fill a reservoir with water. This potential energy buildup is conveted to electrical power through a turbine at the resevoir outlet [19].

1.1.3 Attenuators

Attenuators are articulated multibody devices that generate electricity through the relative motion of the different bodies. The wave induces the motion in the bodies which actuates some form of hydraulic, pneumatic, or direct electrical energy conversion. Figure 1.3 depicts a floating chain of bodies that are aligned with the wave. As the wave passes by the WEC each body is driven by the wave in turn. A fundamental principle of attenuators is that in order to be driven effectively by a wave the WEC itself must be an efficient wave generator [43]. Attenuators often interact with waves while not being fixed to to the ocean floor, as a result mooring lines are typically used for stationkeeping. It is however possible for attenuators to have components free to move with the wave while another component is fixed to the ocean floor, as with the Wavestar device [38]. One of the most iconic attenuator type wave energy converters is the Palamis wave energy converter – often described as a sea snake because its many long slender bodies would oscillate in both the heave and sway directions as the wave passed by [87].

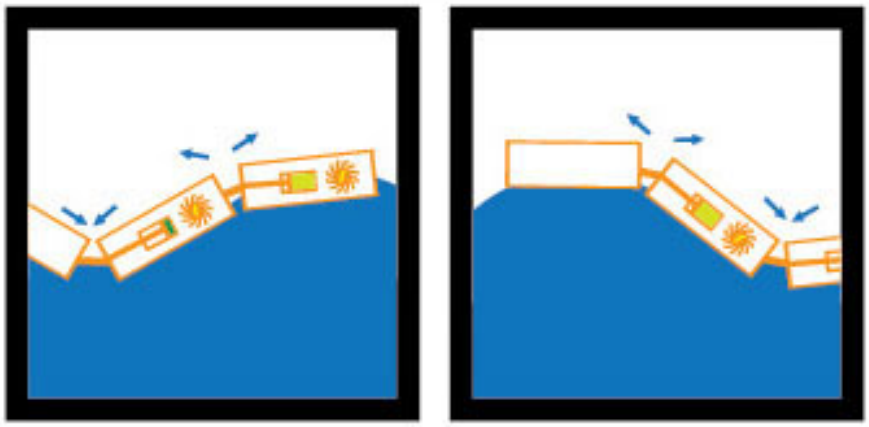

Figure 1.3: Attenuators rely on bodies being driven by the wave to produce relative motion between components. [19].

1.1.4 Point Absorbers

Point Absorbers (PA) are a specific type of attenuator where the motion is primarily in heave and the bodies are small when compared to the wavelength of the incident wave. Point absorbing WECs have become a commonly occuring WEC design because of their deployment versatility. Typically a point absorbing Wave Energy Converter has a body that is meant to act as a wave follower, this float undergoes large amplitude oscillations. Another typical component is the heave plate which is a large surface area submerged well below the surface of the water where the influence of the wave has been significantly attenuated. The heave plate experiences very little motion as it has a large drag force and very little wave forcing. Figure 1.4 shows a configuration where the lower portion of the WEC acts as a heave plate, creating drag in the vertical direction, while the top component will be a surface piercing float that will always remain above the water surface. The Power Take Off (PTO) unit is either designed to be a part of the WEC body or in some cases its own body. Examples of point absorbing WECs include the Ocean Power Technologies Powerbuoy and the Oscilla Power Triton WECs [80, 86]. A point absorbing WEC in which the PTO unit and WEC body is fixed to the ocean floor is the Lysekil project [1].

Point absorbers are well suited for a wide range of applications while at the same time providing a relatively simple mathematical analysis. Point absorbing WECs will be considered for the rest of the analysis in this work. The characteristic dimension of point absorbing WECs can vary greatly depending on the design and indended application. Table 1.1 provides the characteristic dimension of several wave followers. This context provides insight into the size ratio of the point absorbers modeled in this work. The point absorber modeled in Chapter 2 is a early scaled prototype for the Oscilla Power Triton [32, 86], and the WaveStar is modeled in Chapter 3 [29, 103]. The work of Chapters 4 through 6 make use of the Floating Power system [30, 13].

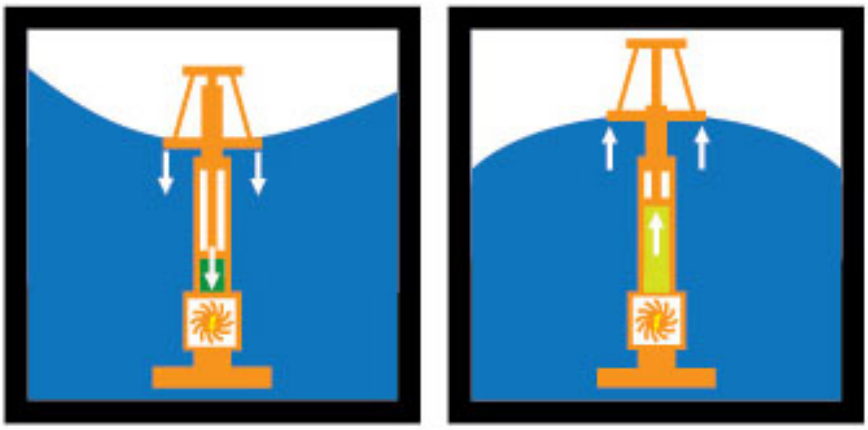

Figure 1.4: Point Absorbers are relatively small WECs that can be deployed in a wide range of environments and rely on the relative motion to generate electricity.

Name of Device	Characteristic Dimension	Reference
Ocean Power Technologies PB3	2.7 m	[80]
Oscilla Power Triton WEC	10 m	[86]
Seabased WEC	6 m	[1, 8]
Ceto Buoy	7 m	[8]
Wavebob	20 m	[8]
WaveStar	5 m	[8]
Floating Power System	5 m	[13]

Table 1.1: Characteristic dimensions of point absorbing WECs.

1.2 Modeling Methods

Just as there are numerous WEC designs under development there are a wide range of modeling approaches in the wave energy conversion industry. The wave energy industry has excelled at the development of modeling methods and design code development as experimental development is often cost prohibitive until late in the design cycle. A typical modeling method is applied to a range of WECs in [8] to establish expected energy collection benchmarks. More specifically to point absorbing WECs, a review article on the common methods

of modeling point absorbing WECs can be found in [63]. Nonlinear models are a current area of research and tend to be introduced incrementally in WEC models as in [103, 29].

Commercial packages for WEC design have become an integral part of the design cycle of WECs, however there has been limited experimental and analytical verification of commercial codes. The National Renewable Energy Laboratory in Golden, Colorado is undergoing a code comparison project to provide some comparison between commercial codes and their own open source WEC modeling package WEC-Sim [23]. Analytical models in both the frequency and time domain are implemented commonly in modeling and control literature. These analytical models can be modified using empirical terms or experimental correction factors as is necessary [12, 63]. The literature also contains purely numerical methods for evaluating WECs, including "numerical wave tanks" which are detailed numerical simulations that are treated as experiments for the purpose of system identification [27, 49].

1.2.1 WEC Design Tools

A succinct benchmark of mid fidelity commercial codes is given in [23] in which each design tool is used to model the same WEC and then the results are compared. The code comparison project shows that a tuning process was needed in order to make the numerical models agree. Commercial packages such as Inwave, WaveDyn, and ProteusDS are intended to provide a complete model that couples the multi-body dynamics of the wave energy converter, the dynamics of the PTO, and the stationkeeping of the mooring lines. These packages can be used to generate very accurate predictions of WEC behavior once there is a certain amount of verification of the parameters being used in the model.

One of the limitations of commercial packages is the tendency for the model to be obscured by the commercial software. It is not always apperant what approximations are being made in the model of a WEC. For commercial packages there is also a finite amount of options that you can have for tuning the model – you only have access to the inputs available to the user. Commercial packages also have a high potential of being cost prohibitive. Furthermore, dynamic models of wave energy converters need the solution to the potential flow problem

of each body to be computed. This is very typically done by boundary element codes such as WAMIT [60], NEMOH [7], or Ansys Aqwa among others. While some commercial codes have integrated the Boundary Element Methods (BEM) code to solve the potential flow problem for the WEC, this extra step generally adds additional overhead and expense to the modeling of a WEC. Commercial packages can provide valuable insight into the design of a WEC, however they are often unsuitable for quick design iterations and investigations of changing parameters.

1.2.2 Time Domain Models

The lumped parameter models used in the WEC industry and those evaluated in this work are described in Chapter 4 in detail. The equation of motion typically used for WEC analysis begins with the Cummins equation [26]. The Cummins equation is an integro-differential equation which was originally developed for modeling ship dynamics [77] and can be written as

$$(M + M_a)\ddot{y} = F_B + F_R + F_M + F_{ex}. \tag{1.1}$$

Where M is the mass of the body, M_a is the mass of the fluid entrained by the body, ¨is the acceleration of the body in any of the six degrees of freedom, F_B is the buoyant force, F_R is the radiation force, F_M is the mooring, or station keeping force, and F_{ex} is the excitation force of the incident wave. The analytical methods used in the Cummins equation rely on converting to the time domain from the frequency domain, which results in convolution integrals that describe the dissipation force of the radiated waves from the body and the excitation force. These convolution integrals often require ythe use BEM programs to determine frequency domain coefficients which can then be transformed into the time domain using an inverse Fourier transform. The terms given in (1.1) are explained in detail in Chapter 4 of this work. It is of interest that the Cummins equation was developed for ships that have a characteristic length on the same order as the incident wave. As a result no viscous drag force is necessary

for the original Cummins formulation, since this force is insubstantial. Use of the Cummins equation is well documented in [8, 34, 63]

Another time domain model used in ocean engineering applications is the empirically based Morison equation[1]. The Morison equation,

$$F = -\frac{1}{2}\rho A C_d(\dot{y} - U)|\dot{y} - U| - \rho \forall C_l(\ddot{y} - \dot{U}) + \rho \forall \dot{U}, \tag{1.2}$$

was developed as a description of the force exerted on a vertical slender pile being subjected to lateral loads from waves. Equation 1.2 describes the externally applied force, F, as a function of the velocity and acceleration of the body, $\dot{y}$ and $\ddot{y}$ respectively, and the surrounding water velocity and acceleration, U and $\dot{U}$ respectively. The coefficients in the Morison equation include: the fluid density, ρ, the projected area, A, the drag coefficient, C_d, the displaced volume of the body, $\forall$, and the inertia coefficient C_i. The Morison equation has been adapted to model systems with a broader range of applications, as outlined in [20]. The ocean engineering design software OrcaFlex relies on the Morison equation as the model for all of the degrees of freedom for modeling the dynamics of ocean structures [67]. The first term in the Morison equation,

$$F_D = -\frac{1}{2}\rho A C_d(\dot{y} - U)|\dot{y} - U|, \tag{1.3}$$

describes the drag force, F_D acting on the body by the surrounding water. This term is typically added to the Cummins equation to include the viscous drag forces in addition to the radiation forces as is discussed in detail in Chapter 4.

[1]Please note that the Morison equation is very commonly misspelled in literature as "Morrison equation".

1.2.3 Frequency Domain Methods

For linear models frequency domain methods can provide insight into the general response of a WEC as a function of the incident wave frequency. A representation known as the response amplitude operator is a typical tool to represent the output of a WEC to the wave input as a function of frequency. Converting from the time domain to the frequency domain can be performed relatively easily using the Laplace transform as described in [32]. A valuable resource on frequency domain methods for wave energy application is [45]. A restriction of these frequency domain methods is that the drag coefficient must necessarily be linearized about a particular operating point. However as discussed in literature [17] the drag coefficients are often unknown, and as a result linearizing can prove to be unreliable. Current optimal control strategies also require time domain WEC models which will restrict this work to only using time domain modeling methods.

1.2.4 Numerical Methods

Numerical methods can also be employed for analysis of WECs. The solution for the potential flow using Green's function or the solution to the Navier-Stokes equation can provide a description of the interaction between waves and WECs [63]. These methods are too computationally time consuming to be used for any real time applications such as model prediction or control and therefore are not used in this work.

Numerical methods however have begun to grow in influence for system identification of the time domain WEC model. In [12] computational fluid dynamics simulations are performed to determine the parameters of the time domain model that they used. This method has a significant advantage over the typical experimental validation of time domain models as you can perform computational simulations to have a good estimate of what each parameter should be prior to the experiments. Additional work is done in [27, 49] to create a numerical wave tank, which allows for numerical simulations to replace some experimental tests. "Numerical wave tank" is a general name for numerical simulators that model the free surface

waves, hydrodynamic forces and body dynamics all at the same time. To accomplish this the Navier-Stokes equation is solved, the pressure acting on the wetted body is computed, the hydrodynamics forces acting on the body are determined, and finally Newton's laws of motion are used to determine the dynamics of the body. Each of these steps are performed for every time step. While the numerical methods do not provide real time utility to WECs they do help to reduce the uncertainty of time domain models.

1.2.5 Nonlinear Modeling

Most of the terms in WEC models are well understood for the linear models that are represented in literature. However, the nonlinearities of the WEC models is a current area of research. Some implementations of nonlinear models are shown in literature, however their implementation is far from widespread [59, 88]. The most common nonlinear term is the viscous drag force given by (1.3). This drag coefficient is however not well known in wave energy applications. Methods of determining the drag coefficient are given in Chapter 4 of this work. It is typical for the drag coefficient to act as a correction factor in order to mitigate the non physical oscillations that are simulated. Reference [23] describes that tuning the drag coefficient is necessary for a commercial code comparison project, and in order to produce a reasonable code benchmark of WEC devices the drag coefficient was varied by a factor of eight in [8].

1.3 Control Methods

Historically, WECs were typically designed for regular and near regular wave conditions, which was accomplished by tuning their damped natural frequency to match the frequency of the expected waves. This tuning process was also considered for use in real time as point absorbing WECs would tune their PTO damping to match the peak frequency of the wave climate exciting the WEC [37]. These parameter tuning control systems would primarily work in regular wave situations, which do not accurately represent the waves experienced during deployments. Optimal power generation in irregular waves requires control methods

to do a wave-by-wave analysis to determine optimal control inputs.

An active method of control that was proposed very early in the development of WECs was latching control [18]. Latching control can be used on single degree of freedom WECs such as a typical point absorber. Optimal power absorption is achieved when the phase of the WEC is properly aligned with the wave excitation force, to this end latching control uses an actuator to lock a WEC in a specific position long enough for the WEC to remain at the proper phase with the excitation force. This process of locking and unlocking the WECs single degree of freedom became known as latching. Due to complications introduced by latching control, both with determining exactly when to unlatch the device and how to actuate the latching procedure, other modern control methods have been under development.

Model Predictive Control (MPC) and Nonlinear Model Predictive Control (NMPC) are control methods that solve an optimization problem over a small time horizon. This makes these methods very good at dealing with changing wave climates and determining the optimal control input for incident waves. However, a short prediction of incident wave elevation or wave excitation force is necessary in order to run this type of controller. MPC was applied to a WEC in [14], however state identification and wave prediction were mentioned only briefly. Additional work into a NMPC controller that does not allow any reactive power input into the system by the controller has been analyzed in [96]. MPC and NMPC have received a lot of focus in recent years and were shown to be experimentally viable as a WEC control methods in [97]. A review analyzing the current state of WEC control systems with a focus on model predictive methods is given in [40]. Alternative control methods are also under development, such as control methods using a linear quadratic gaussian to produce an optimized control input that does not require any wave prediction horizon [91], and further explorations into the theoretical maximums of heaving WECs [61].

1.3.1 State Estimation and Input Prediction

In modern control strategies information about the states is needed. As addressed in [14] and [64] this is possible through the use of Kalman filters as optimal state observers. In

fact, while research is currently being done to determine the best way of estimating the wave excitation force [64, 78], the most common method of determining this force is through a Kalman filter. Even though Kalman filters have widespread use, their implementation on WECs is not obvious and there are some limitations, as described in Chapter 4. The work detailed in Chapter 4 is meant to deal with the current barriers to state observation using an Extended Kalman Filter (EKF), which is the nonlinear adaptation of the Kalman filter.

The prediction of the wave excitation force is also required in a significant component of modern control work [65, 47]. Autoregressive methods which utilize only the current and past data of a given point are of primary interest to many researchers [64, 46]. A summary of controls research papers and the corresponding prediction requirements is given in [65]. While some research purposefully only assumes current and past knowledge much of the expected benefit of optimal control methods for WECs depends on anticipatory control systems. The simulation work described in [47, 62] shows the potential power production gains for WECs with predicted wave excitation. In this work, Chapter 5 addresses the problem of wave excitation force estimation for WECs while Chapter 6 addresses the problem of predicting the wave excitation force.

1.4 Current State of Wave Energy

The Ocean Energy Systems Collaboration Program (OES) was established by the International Energy Agency to enhance research, development, and demonstration of marine renewable energy. OES provides details of WEC developments of about twenty countries that are working towards developing wave energy [5]. The OES also provides details on current deployments, technological readiness, and summaries of joint development projects. While technological development proceeds, the human and legislative aspects of wave energy are also being addressed as shown in the review work [98]. The Pacific Marine Energy Center (PMEC) also has a strong focus on the integration of wave and tidal energy into society [85]. Technical reviews of the power conversion methodologies and modeling can be found in the works of [82] and [93], respectively.

Chapter 2

MODELING AND ANALYSIS OF A MULTI DEGREE OF FREEDOM POINT ABSORBER WAVE ENERGY CONVERTER

The text of the following chapter was accepted for publication in the 33rd International Conference of Ocean, Offshore and Arctic Engineering (OMAE) in 2014. With the exception of reformatting the text no changes were made to the content of the article as accepted. The citation for the paper, Ref. [32], is as follows:

Andrew F. Davis, Jim Thomson, Tim R. Mundon, and Brian C. Fabien. Modeling and analysis of a multi degree of freedom point absorber wave energy converter. In *Proceedings of the 33rd International Conference of Ocean, Offshore and Arctic Engineering*, volume 8A, 2014.

2.1 Introduction

Wave energy has strong potential for being a component of the solution to the problems presented by an increasing energy demand. While the idea of harvesting energy from waves is not new, there has been increasing research in this area. Wave energy converters (WECs) have significant potential in the marine renewable energy field, and pre-commercial prototypes of marine energy devices are being developed and implemented in test situations. However, significant research is still required to develop wave energy into a feasible renewable energy source for coastal regions [55].

The mooring and installation of a wave energy converter is a significant factor in the cost of produced energy. In shallow waters (i.e., depth less than 30 meters) it may be cost effective to use a rigid foundation, such as a monopile or jacketed pile. However at greater

depths or when the wave energy converter must respond dynamically to the water surface (as in the case of point absorbing wave energy converters), compliant moorings are necessary. Work has been done to model the dynamics of compliant and even slack mooring lines [39]. However, this must be combined with an effective model of WEC dynamics and power generation in order to optimize the configuration of the mooring lines to minimize the cost of power production.

There are several existing commercial software packages such as OrcaFlex, ProteusDS, ANSYS Aqwa, and WAMIT to model the dynamics of marine systems. However, by extending a first principles model to arrays of WECs it will be possible to create simple and generic design tools to maximize the performance of marine energy converters. To better understand the performance of the system, and thereby work towards the eventual goal of performance maximization, the final outcome of the system modeling and identification is the parameter sensitivity analysis.

Section 2.2 presents a general description and the simplifying assumptions that are used to formulate the equations of motion. Section 2.3 gives a brief description of the deployment of the prototype WEC along with the experimental resources used for validation wherein a representative wave period and amplitude are used to realistically describe the behavior of the lake deployment. In section 2.4 the numerical methods used to solve for the dynamics of the WEC are shown, then the simulated output and the experimental data is compared. Section 2.5 develops conclusions on which parameters have the greatest effect on the efficiency of the system. The study is concluded with a discussion of results in section 2.6.

2.2 System Model

The Oscilla WEC is a point absorbing wave energy converter that produces power from the rate of change of tension in the power take off (PTO) units. The simplified model presented assumes that the deflection in the PTOs and the load cell is negligible compared to the deflection in the connections between the WEC components. Because the mooring lines are placed symmetrically, and are not exerting significant tension, this initial model does not

include the mooring lines. Considering the vertical motion of the buoy while neglecting the force component of the mooring lines can still produce a reasonably accurate simulation [35].

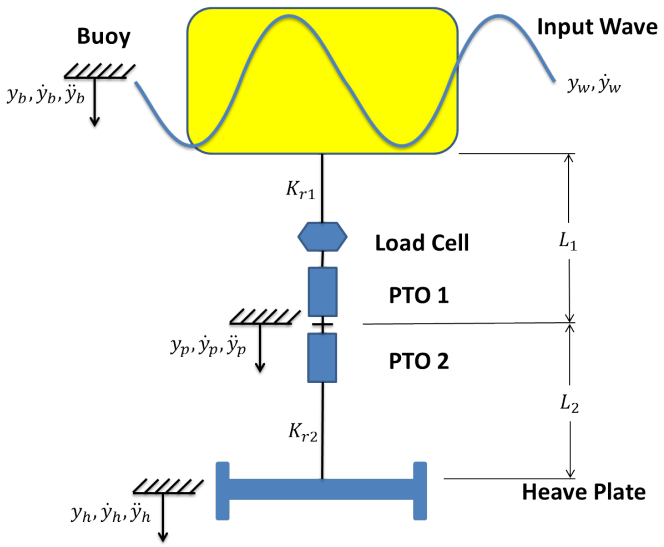

Figure 2.1: Simplified model of the Oscilla Power prototype WEC.

Figure 2.1 shows a simplified model of the prototype point absorber. Component displacements are shown from the natural length of each connection. The variable y_w is the distance from the steady water line to the surface of the water. The displacements y_b, y_p, and y_h show the positive direction of motion for the buoy, PTO units, and heave plate, respectively. Velocities are denoted with a single dot and accelerations are denoted with two dots. The variables K_{r1} and K_{r2} are the linear spring constants that are used to model the connections between the lumped mass components. The variables L_1 and L_2 denote the lengths of the connections between the buoy and the load cell and the lower PTO unit and the heave plate respectively. For the deployed system $L_2 >> L_1$.

The buoy and components will follow the motion of the wave, and the heave plate will create a significant amount of tension in the PTO units. The mass of the heave plate, as it

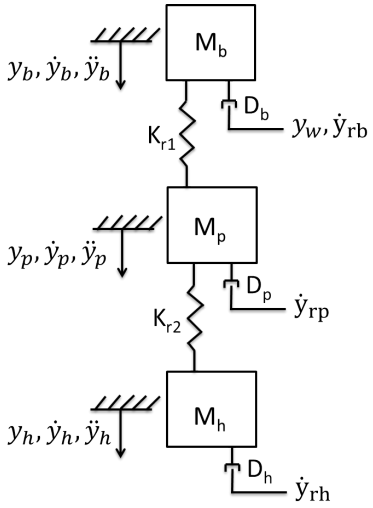

Figure 2.2: Mass-Spring-Damper model of the Oscilla Power prototype.

is submerged some distance below the surface, is subject to a greatly reduced wave forcing and its drag and inertia are large enough so that there will always be tension in the central cable. By continuously maintaining tension in the cable, destructive shock loading is avoided during deployment.

While Ref. [35] presents a similar system description to Figs. 2.1 and 2.2, it is important to note that in Ref. [35] both bodies breach the surface which results in two variable buoyant forces compared to the single variable buoyant force in this model. The PTO connection in Ref. [35] produces a damping force proportional to the relative velocity, whereas in this model the PTO force is modeled as a linear spring as shown in Fig. 2.2. In Ref. [35] the forces associated with the radiation damping of the system are computed using a state space formulation, by contrast, this model only considers the profile drag and skin friction on each body. Finally, [35] uses the commercial package, WADAM, to compute coupled added mass terms and produce the numerical validation of the model, whereas this development uses simplified body geometry to estimate the added mass and performs the validation against experimental results.

2.2.1 Equations of Motion

A simplified model of a mass-spring-damper system is created to represent the system shown in Fig. 2.1. Figure 2.2 shows how the WEC is modeled as 3 separate masses with the connections between each mass acting as springs. The displacements and spring constants are defined in Fig. 2.2. The variables M_b, M_p, and M_h are the lumped masses of the buoy, PTO units, and the heave plate, respectively. The linear drag coefficients, D_b, D_p, and D_h, are shown on each mass in reference to the relative water velocity. The relative water velocity of the buoy, $\dot{y}_{rb}$, the PTO units, $\dot{y}_{rp}$, and the heave plate, $\dot{y}_{rh}$, is given by an exponential attenuation term that models a diminishing water velocity as a function of the wave number and depth. The water displacement, y_w, is shown in reference to the buoy because the surface of the wave and the buoy displacement are measured from the same reference and the wave displacement is used to compute the variable buoyant force acting on the buoy.

The primary source of damping in the system is the fluid drag of the masses passing through the water. The dynamics of the WEC are decomposed and analyzed in a similar manner to Refs. [36, 100]. By lumping the load cell and both PTO units together as a single mass the number of equations of motion is reduced from 5 to 3 with little loss of detail. The PTO lumped mass is a reasonable approximation because the load cell and PTO units are connected with rigid links with no appreciable strain. Therefore, the displacements of the 3 smaller components are all the same as the lumped displacement y_p.

Using Newton's law to describe the equation of motion for each mass results in 3 second order ordinary differential equations. The equation of motion for each of the three masses takes the form

$$m\ddot{y} = F_{Weight} + F_{Buoyancy} + F_{Drag} + F_{Spring} \tag{2.1}$$

$$+ F_{Radiation} + F_{WaveExcitation}, \tag{2.2}$$

where the dot notation shows the number of time derivatives of a variable and the product of the mass and acceleration is equal to the sum of the forces acting on the mass.

The weight and buoyancy of each mass are included in the summation of forces according to the direction conventions established in Fig. 2.2. It is important to note that the buoy will have a variable buoyant force, whereas the other components will have a constant buoyant force. The variation in the buoyant force at the buoy is due to the fact that as more of the buoy becomes submerged the weight of the displaced fluid will increase which causes the buoyant force to increase.

The drag force is comprised of two main components, the friction drag and the profile drag. The drag force acting on a mass passing through a fluid is computed using the equation

$$F_{Drag} = \frac{1}{2} C_{drag} A \rho V |V|, \tag{2.3}$$

where C_{drag} is the coefficient of drag, the computed area, A, is the area relevant to the type of drag, V is the net velocity of the object with respect to the fluid particles surrounding it, and ρ is the density of the fluid. The friction drag coefficient, C_f, is computed by

$$C_f = \frac{0.16}{Re^{1/7}}, \tag{2.4}$$

$$Re = \frac{\hat{a}}{2} \frac{\omega d}{\nu}, \tag{2.5}$$

where Re is the Reynolds number computed in wave conditions, $\hat{a}$ is the peak to peak amplitude of the wave, d is the characteristic length of the buoy, ω is the frequency, and ν is the kinematic viscosity of the water [77]. For the system simulated below a characteristic length of 1.7 meters is used. Equation (2.4) computes the average shear stress coefficient which is used as the coefficient of skin friction. Small amounts of friction will be generated by the boundary layer effects as the water travels along the sides of the masses. Once the coefficient of skin friction, C_f, is computed (2.3) is used to compute the force acting on the mass.

The second type of drag is the profile drag, which is created when an object passes through a fluid, requiring fluid particles to pass around the mass. Equation (2.3) is also used

to compute the profile drag on each mass by using a dimensionless drag coefficient, C_D, and the projected surface area of the mass in the direction of motion. The dimensionless drag coefficients are determined using the shape and the dimension ratios of each mass [101].

Both forms of drag are computed using the relative velocity between the mass and the fluid. To accurately characterize the fluid velocity at each point in the model an attenuation term is used to describe the water particle velocity surrounding each mass. This is given by $e^{-(depth)(k)}$, where $k = \frac{\omega^2}{g}$ is the wave number [71]. The wave number is an expression of the wave frequency, ω, and the gravitational acceleration, g.

For the system considered below, the wave period that was used to compute the wave frequency is 3 seconds. While 3 seconds is a very small wave period for ocean waves, 3 seconds is a reasonable period in Lake Washington. The exponential attenuation term computes a very small velocity at the depth of the PTO units and by extension the wave velocity at the depth of the heave plate is negligible during operational conditions. Figure 2.2 illustrates that each mass will have a different surrounding water particle velocity that will be used when computing the drag. The attenuated wave velocities are computed as

$$\dot{y}_{rb} = \dot{y}_w e^{-\frac{1}{2}k}, \tag{2.6}$$

$$\dot{y}_{rp} = \dot{y}_w e^{-7k}, \tag{2.7}$$

$$\dot{y}_{rh} = \dot{y}_w e^{-14k}. \tag{2.8}$$

The attenuated wave velocities are approximated using constant values for the depths for each mass. A constant depth of $\frac{1}{2}$ meter is used for the buoy, 7 meters for the lumped PTO units, and 14 meters for the depth of the heave plate. Calculating the wave particle velocity attenuation as if each body is a single point is valid in situations where the bodies are small compared to the depth that the wave motion penetrates the water.

For this model the spring force, F_{Spring}, is given as a linear spring constant, K_{r1} or K_{r2}, multiplied by the net extension from the connections natural length to compute the spring force acting on each mass. The spring constant K_{r2} is given by the vendor estimation

of the rope used, and K_{r1} is large enough to ensure that the buoy and the PTO mass move together. Since the displacements are measured from the natural length rather than from a single reference point, the net extension is computed by finding the difference of the displacements of each body.

The radiation damping term, $F_{Radiation}$, is comprised of both an added mass term and a radiation damping term. The radiation damping term is a force that acts on the buoy during oscillatory motion in the water. Since the WEC has a very small characteristic length compared to the wavelength the radiation damping term is insignificant [77]. By contrast the added mass of the system still plays a significant role in the formulation of the equations of motion and is described below. The added mass of each body is summed with the dry mass to create a single term to describe the inertia of each body.

The heave response of an axisymmetric body when the draft of the buoy is small compared to the wavelength is $z(t) = a\,cos(\omega t + \epsilon)$, where $z(t)$ is the heave displacement of the body, a is the amplitude, ω is the wave frequency, t is the time, and ϵ is the phase of the response [77]. The wave excitation force on the buoy can be modeled similarly to [100], as $F_{excitation} = aF\,cos(\omega t + \epsilon)$. Just as in [100] the phase is assumed to be zero and in this case, $F = B_b$, where B_b is referred to as the variable buoyancy. B_b has units of force per unit length and is given by multiplying the area of the bottom of the buoy by the density of water and the acceleration due to gravity. When B_b is multiplied by the length of the submerged portion of the buoy the weight of the displaced fluid is the same as the buoyant force acting on the buoy. The excitation force is shown in the equation of motion as $F_{WaveExcitation} = B_b y_w$, where y_w is the position of the wave surface described in further detail in section 2.4.1. The wave excitation on the PTO units and the heave plate is negligible because they are submerged several meters below the wave motion.

Three separate equations of motion are formed to describe the independent motion of all three lumped masses. The Oscilla system has a significantly more rigid connection between the buoy and the PTO units than the connection between the PTO units and the heave plate. This is reflected in the model by the use of the two different spring constants K_{r1}

and K_{r2}. Nevertheless, three equations of motion are modeled because it is the goal of this research to evaluate how variations in the structural properties affect the power production of the system. The resulting differential equations are:

$$\begin{aligned} m_{vb}\ddot{y}_b =& B_b y_w + m_b g - B_b y_b - \frac{C_{Db}}{2} A_b \rho (\dot{y}_b - \dot{y}_{rb})|\dot{y}_b - \dot{y}_{rb}| \\ & - \frac{C_f}{2} A_{bwet} \rho (\dot{y}_b - \dot{y}_{rb})|\dot{y}_b - \dot{y}_{rb}| - K_{r1}(y_b - y_p), \end{aligned} \tag{2.9}$$

$$\begin{aligned} m_{vp}\ddot{y}_p =& m_p g - B_p - \frac{C_{Dp}}{2} A_p \rho (\dot{y}_p - \dot{y}_{rp})|\dot{y}_p - \dot{y}_{rp}| \\ & - \frac{C_f}{2} A_{pwet} \rho (\dot{y}_p - \dot{y}_{rp})|\dot{y}_p - \dot{y}_{rp}| \\ & - K_{r1}(y_p - y_b) - K_{r2}(y_p - y_h), \end{aligned} \tag{2.10}$$

$$\begin{aligned} m_{vh}\ddot{y}_h =& m_h g - B_h - \frac{C_{Dh}}{2} A_h \rho (\dot{y}_h - \dot{y}_{rh})|\dot{y}_h - \dot{y}_{rh}| \\ & - \frac{C_f}{2} A_{hwet} \rho (\dot{y}_h - \dot{y}_{rh})|\dot{y}_h - \dot{y}_{rh}| - K_{r2}(y_h - y_p). \end{aligned} \tag{2.11}$$

The inertia term in the equation of motion for the buoy (2.9) is $m_{vb}\ddot{y}_b$, where m_{vb} is the virtual mass of the buoy described later, and $\ddot{y}_b$ is the acceleration of the buoy defined in Figs. 1 and 2. The weight of the buoy is given as $F_{Weight} = m_b g$, where m_b is the mass of the buoy given in Table 2.1 and $g = 9.81 \frac{m}{s^2}$ is the acceleration due to gravity at sea level. $F_{Buoyancy} = B_b y_b$ is the variable buoyant force of the buoy described above.

The total drag force is given by summing the friction drag and the profile drag. The drag force is included in the equation of motion as

$$F_{Drag} = \frac{C_{Db}}{2} A_b \rho (\dot{y}_b - \dot{y}_{rb})|\dot{y}_b - \dot{y}_{rb}| \tag{2.12}$$

$$+ \frac{C_f}{2} A_{bwet} \rho (\dot{y}_b - \dot{y}_{rb})|\dot{y}_b - \dot{y}_{rb}|, \tag{2.13}$$

where C_{Db} is the drag coefficient based on the geometry of the leading surface of the buoy as it moves in the positive direction. A_b is the projected area of the buoy's leading surface, for this model the magnitude of the drag force is computed identically for positive and negative

velocities. The variable, ρ, is the density of the surrounding fluid, and the difference $(\dot{y}_b - \dot{y}_{rb})$ is the relative velocity of the buoy. C_f is the shear stress coefficient from (2.4) and is assumed to be identical for all three lumped masses. A_{bwet} is the submerged surface area of the sides of the buoy. For the buoy the wetted area is given by a constant surface area, just as with the other two lumped masses, to preserve the linearity of the model.

Finally, the spring force in (2.9) is given by $F_{Spring} = K_{r1}(y_b - y_p)$, where $y_b - y_p$ is the net extension in the connection between the buoy and the PTO units and K_{r1} is the spring constant of the connection between the buoy and the PTO units as shown in Figs. 2.1 and 2.2. The sign conventions that appear in the equations of motion are established in Fig. 2.1, and subscripts defined in Figs. 2.1 and 2.2 are used to distinguish specific components. The other equations of motion are developed in a similar manner to (2.9).

It is important to note that the virtual mass is denoted with m_{vb}, m_{vp}, and m_{vh} where the subscript v identifies that the value is the virtual mass and the bodies are identified with subscripts b, p, and h. The virtual mass for each component is the sum, $m_v = m + m_a$, where m_a is the added mass correction factor and m is the mass. The added mass term is used to compensate for the fluid that is carried along with each mass as the components pass through the water. This entrained fluid may be a substantial modification to the inertia of each component, however it is important to note that this added mass does not contribute to the weight of the components.

When computing the added mass in the heave direction the geometry of the bodies is required. Typically a tool such as WAMIT is used to determine added mass coefficients for bodies with complex geometries. However, in this paper the geometries of the bodies are simplified and closed form equations for added mass are given in Ref. [15]. In particular the added mass for the PTO unit is roughly 4% of the actual mass and the added mass of the heave plate and buoy are roughly 40% of their respective masses. The hydrodynamic mass of the vertical motion of a circular disk, which represents the heave plate, is given by the expression $m_h = 8/3\rho r^2$, where ρ is the density and r is the radius of the disk. The added mass of the PTO units is computed in a similar manner to the added mass of the heave

plate. For the model validated below the added mass of the buoy is computed by taking into consideration the volume of water displaced as a result of the buoy motion. The sensitivity study shows the effect of changes in the added mass of each body.

2.2.2 Frequency Response Analysis

In order to develop the spectral method of simulating the response of the system the nonlinear drag term is linearized. Damping coefficients are often a very uncertain component of a model, in this case the dominant wave period of roughly 2.5 seconds is used and a peak to peak amplitude of 1 meter is used. By choosing a somewhat larger than standard wave amplitude the linear approximation is guaranteed not to under estimate the damping throughout the full range of the velocity. An over estimation of the simplified damping term at this point in the model is acceptable considering that there are additional forms of damping, such as radiation damping, that would cause additional losses in a real system.

The following development of a linearized drag constant is shown for a general mass which is signified by parameters with no subscript (b, p, or h). C_D, A, A_{wet}, and C_f are the same parameters as described in section 2.2.1, however this drag coefficient linearization is performed for all 3 bodies. The nonlinear drag coefficient is composed of the profile drag and the skin friction

$$C = \frac{1}{2} C_D A \rho + \frac{1}{2} C_f A_{wet} \rho, \tag{2.14}$$

where the first term is the profile drag and the second term is the skin friction. In the case of the buoy A_{wet} is assumed to be half the surface area of the buoy to obtain a linear damping coefficient. The wetted areas of the other bodies are calculated based on geometry. By Ref. [21] the nonlinear damping can be approximated by

$$F_{damping} = C\dot{x}|\dot{x}| = C\hat{a}\omega_o\dot{x}, \tag{2.15}$$

where $\hat{a}$ and ω_o are the peak to peak amplitude and the wave frequency respectively, and $\dot{x}$ is the body velocity. The linear drag coefficient,

$$D = \frac{1}{2}\hat{a}\omega_o \left[C_D A_{body} + C_f A_{wet}\right], \tag{2.16}$$

is formed by using the velocity linearization in (2.15) and summing both types of drag on the system. The drag force is modeled by $F_{Drag} = D\dot{x}$. The wave displacement, $y_w = a\, sin(\omega t)$, and wave velocity, $\dot{y}_w = a\,\omega\, cos(\omega t)$, are input forcing functions to this model described in further detail in section 2.4.1. The variables a and ω are the amplitude and frequency inputs determined by the Pierson-Moskowitz spectrum described in section 2.3. The terms are separated and organized for state space formulation as follows:

$$\begin{aligned} m_{vb}\ddot{y}_b =& - D_b\dot{y}_b - B_b y_b - K_{r1}y_b + K_{r1}y_p + m_b g + B_b y_w \\ &+ D_b\dot{y}_{rb}, \end{aligned} \tag{2.17}$$

$$\begin{aligned} m_{vb}\ddot{y}_p =& - D_p\dot{y}_p - K_{r1}y_p - K_{r2}y_p + K_{r1}y_b + K_{r2}y_h \\ &+ m_p g - B_p + D_p\dot{y}_{rp}, \end{aligned} \tag{2.18}$$

$$m_{vh}\ddot{y}_h = - D_h\dot{y}_h - K_{r2}y_h + K_{r2}y_p + m_h g - B_h + D_h\dot{y}_{rh}. \tag{2.19}$$

The 3 degree of freedom system in state space format with the wave input is given by:

$$\underline{M}\ddot{y} = \underline{K}y + \underline{C}\dot{y} + e_o + e_1 y_w + e_2\dot{y}_w, \tag{2.20}$$

$$\underline{M} = \begin{bmatrix} m_b + m_{ab} & 0 & 0 \\ 0 & m_p + m_{ap} & 0 \\ 0 & 0 & m_h + m_{ah}, \end{bmatrix}, \tag{2.21}$$

$$\underline{K} = \begin{bmatrix} -(B_b + K_{r1}) & K_{r1} & 0 \\ K_{r1} & -(K_{r1} + K_{r2}) & K_{r2} \\ 0 & K_{r2} & -K_{r2} \end{bmatrix}, \tag{2.22}$$

$$\underline{C} = \begin{bmatrix} -D_b & 0 & 0 \\ 0 & -D_p & 0 \\ 0 & 0 & -D_h \end{bmatrix}, \tag{2.23}$$

$$e_o = \begin{bmatrix} m_b g \\ m_p g - B_p \\ m_h g - B_h \end{bmatrix}, e_1 = \begin{bmatrix} B_b \\ 0 \\ 0 \end{bmatrix}, e_2 = \begin{bmatrix} D_b e^{-\frac{1}{2}k} \\ D_p e^{-7k} \\ D_h e^{-14k} \end{bmatrix}. \tag{2.24}$$

The virtual mass matrix, $\underline{M}$, is composed of diagonal elements where the mass and the added mass are summed. Let $q_1 = y$ and $q_2 = \dot{y}$ to perform a reduction of order. The new first order system is

$$\dot{q}_1 = q_2, \tag{2.25}$$

$$\dot{q}_2 = \underline{M}^{-1} \left[\underline{K} q_1 + \underline{C} q_2 + e_o + e_1 y_w + e_2 \dot{y}_w \right]. \tag{2.26}$$

Using $q = \begin{bmatrix} q_1 \\ q_2 \end{bmatrix}$ the equations of motion become

$$\dot{q} = \hat{A} q + \hat{B}_o + \hat{B}_1 y_w + \hat{B}_2 \dot{y}_w, \tag{2.27}$$

where

$$\hat{A} = \begin{bmatrix} 0 & I \\ \underline{M}^{-1}\underline{K} & \underline{M}^{-1}\underline{C} \end{bmatrix}, \hat{B}_o = \begin{bmatrix} zeros(3,1) \\ \underline{M}^{-1}e_o \end{bmatrix}, \tag{2.28}$$

$$\hat{B}_1 = \begin{bmatrix} zeros(3,1) \\ \underline{M}^{-1}e_1 \end{bmatrix}, \hat{B}_2 = \begin{bmatrix} zeros(3,1) \\ \underline{M}^{-1}e_2 \end{bmatrix}, q = \begin{bmatrix} y_b \\ y_p \\ y_h \\ \dot{y}_b \\ \dot{y}_p \\ \dot{y}_h \end{bmatrix}. \tag{2.29}$$

The frequency response analysis considers the motion of the system relative to the equilibrium position, hence the constant force terms are neglected. The Laplace Transform of (2.27) produces

$$(sI - \hat{A})Q = (\hat{B}_1 + \hat{B}_2 s)Y_w, \tag{2.30}$$

$$\frac{Q}{Y_w} = (sI - \hat{A})^{-1}(\hat{B}_1 + \hat{B}_2 s). \tag{2.31}$$

Q and Y_w are the Laplace transforms of the output and input respectively. The transfer function $\frac{Q}{Y_w}$ is formed by algebraic manipulation of (2.31), and is useful to determine the input-output relationship of the motion of the WEC components.

The symbolic computation is done using the MATLAB symbolic toolbox. This transfer function is defined in the frequency domain by multiplying the displacement transfer function by the derivative operator squared. The transfer function

$$\frac{\Lambda}{Y_w} = s^2 \frac{Q}{Y_w}, \tag{2.32}$$

gives the relationship from the displacement input to the acceleration output. Λ is the acceleration of the system and Y_w is the Laplace transform of the wave input.

2.3 Deployment

The Oscilla WEC first generation prototype was deployed in Lake Washington, by the University of Washington Applied Physics Laboratory. During this 3 month deployment, data was collected for the 3 axis accelerations of the buoy enabling the fundamental means of validating the numerical model of the WEC. Additionally, a load cell in series with the PTO units measured the tension between the PTOs and the buoy. The first three panels in Fig. 2.3 show a short time span of the raw data collected during the Lake Washington deployment. The deployment data was taken during a winter storm to demonstrate well defined wave characteristics.

Lake Washington was a safe testing environment with its relatively calm waters for the vast majority of the time, however during occasional storms the 5 kilometer fetch and increased wind speed allow for more fully developed wave conditions. The deployment occurred at a depth of 52 meters. Incident wave data was taken using a Waverider MK III directional buoy for the duration of the Oscilla Power deployment. Internal to the Waverider buoy, data was processed and stored as a Power Spectral Density (PSD). It is therefore necessary to convert the Waverider PSD data to an amplitude spectrum by multiplying by the bandwidth, then dividing the square root by half to provide valid one-sided amplitude inputs to the simulation used to validate the response of the linear model.

The Pierson-Moskowitz (PM) spectrum is used to model the wave data as a continuous function of frequency. The PM spectrum is a 1 parameter spectrum based on the wind speed in meters per second at 19.5 meters above the steady water line [99]. The PM spectrum is characterized by the assumption that the waves are generated by a steady wind with a very long fetch. The expected spectral amplitude at a given frequency is calculated using

$$E(f) = \frac{0.0081g^2}{(2\pi)^4 f^5} e^{(-0.74(\frac{2\pi f U_w}{g})^{-4})}, \tag{2.33}$$

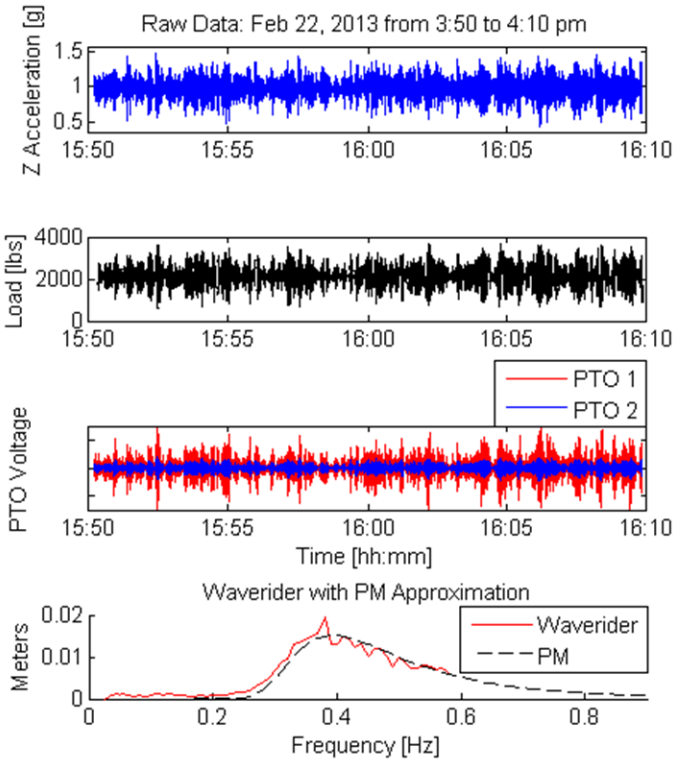

Figure 2.3: Sample raw data from the Oscilla Power wave energy converter generation 1 deployment with measured and approximated incident wave data. Units and y-axis omitted on panel 3 for proprietary reasons.

where g is the acceleration due to gravity, 0.0081 is the Phillips constant, f is frequency given in Hz, and U_w is the wind velocity in meters per second at an elevation of 19.5 meters.

In order to determine the wind speed, an optimization function is used to find the wind speed that minimized the error between the PM and the Waverider Spectra. The fourth panel in Fig. 2.3 shows two examples of the best fit PM spectra. While the high peaks in the Waverider data are not captured by the continuous function, the realistic higher frequencies are included. It is important to note that using a JONSWAP spectrum would add an extra parameter providing a more accurate model for fetch limited conditions [99]. However, the experimental conditions are well represented with the more simple PM spectrum.

2.4 Numerical Simulation

The time domain simulation program is implemented in MATLAB to simulate the heave motion of the WEC when subjected to a spectral wave input. The time domain simulation requires time series data for both the displacement and the velocity of the input wave. Since this system involves stiff differential equations, a small time step and a stiff ODE solver is used to simulate the motion of the 3 bodies of the WEC. The acceleration is computed from the simulated displacements and velocities, and the acceleration amplitude spectrum is computed using a Discrete Fourier Transform algorithm.

By using a transfer function, it is possible to compute the acceleration amplitude spectrum given a wave input defined by the PM spectrum by (2.33). This can be compared to the amplitude spectrum of acceleration provided by applying a Discrete Fourier Transform to the vertical acceleration data in Fig. 2.3. The spectral methods provided excellent validation of the numerical integration of the time series solution.

The dynamics of the WEC are compared using the power spectrum of the acceleration measured in the buoy of the Oscilla WEC. Figure 2.4 shows the dynamics of the linear model compared to the acceleration response of the deployed system. Once the response of the model was compared against the experimental results a time domain simulation is used to estimate the output of the model as described below. To compute the power spectral density the Fourier coefficients are multiplied by their complex conjugates and then divided by the bandwidth multiplied by two. In this case the bandwidth is $8.56 \cdot 10^{-3}$ Hz and Fig. 2.4 shows the PSDs as computed using the pwelch function in MATLAB.

2.4.1 Time Domain Simulation

The time domain simulation of the WEC in response to a wave input is computed by using the stiff numerical integrator ode23s in MATLAB. The PM spectrum of wave amplitudes is used to generate the wave input to the time domain model. Modeling the input wave

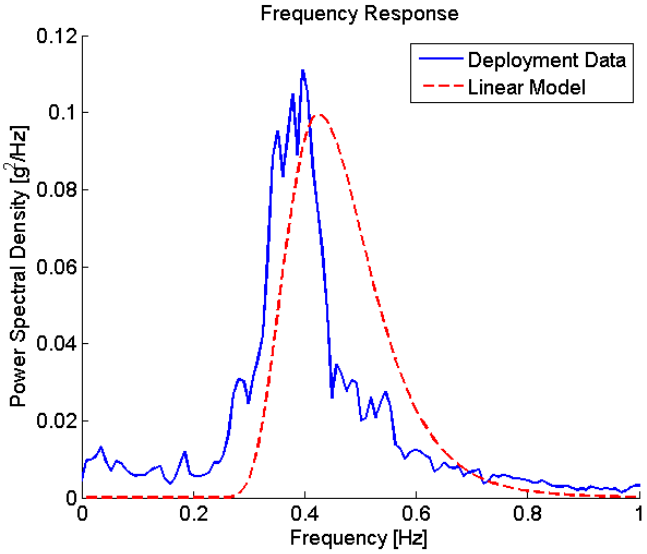

Figure 2.4: Power spectral density of the experimental data and the linear model. The measured acceleration, $\ddot{y}_b$, is the acceleration experienced by the buoy.

displacement and velocity by

$$y_w(t) = \sum_{i=1}^{300} a_i \, sin(\omega_i t + \phi_i), \tag{2.34}$$

$$\dot{y}_w(t) = \sum_{i=1}^{300} a_i \omega_i \, cos(\omega_i t + \phi_i), \tag{2.35}$$

gives a time domain representation of the wave. Equations (2.34) and (2.35) are the sum of 300 sine or cosine waves where the frequencies ω_i are equally spaced, starting at $\omega_1 = 0.15$ Hz and ending with $\omega_{300} = 1$ Hz, and the magnitudes, a_i, correspond to the amplitude of the PM spectrum at the corresponding frequencies, ω_i. The sum is truncated at 300 input frequencies because the variance of the spectrum converges to a constant value. The variable ϕ_i is the phase of each component of the wave spectrum, and is determined by choosing a random phase between 0 and 2π radians. Although real waves do not have a truly random phase, a reasonable time domain input is creating by randomizing the phase for each fre-

quency and amplitude pair.

Figure 2.5 shows the relative position from the natural length of the connections, il-

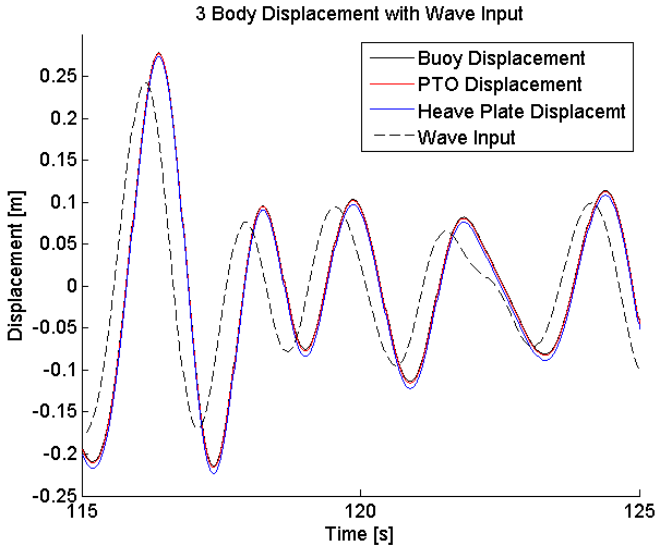

Figure 2.5: Time domain simulation of the relative deflections of the 3 bodies with reference to the wave input, displacement direction is opposite of the convention established in Figs. 2.1 & 2.2 for ease of visualization.

lustrating the relative displacement of all three bodies of the WEC compared to the wave input. This enables clear visualization of how the converter is moving when being forced by the incident wave input. As expected, relative positions of the components show that there is never a situation where the connection, holding the components together, is slack which would cause shock loading on the PTO units.

2.4.2 Predicted Power Production

By using the validated model of the motion of the buoy and comparing the predicted PTO output based on the rate of change of tension it is possible to identify the linear proportionality constant α relating the tension derivative to the power production $\mathbb{P} = \alpha \dot{T}$. Here, $\mathbb{P}$ is the power production of the PTO units and $\dot{T}$ is the time rate of change of the tension in

Table 2.1: Error in the modeled power, Feb. 22, 2013 to Feb. 23, 2013.

Time	T_D [s]	H_s [m]	% Error
22:30-23:00	2.56	0.14	-3.7
23:00-23:30	2.53	0.14	8.2
23:30-24:00	2.58	0.21	7.2
00:00-00:30	2.67	0.21	-8.2
00:30-01:00	2.67	0.28	-10.6
01:00-01:30	2.63	0.28	3.5
01:30-02:00	2.54	0.25	13.3

the PTO units. Oscilla Power has developed models describing the power production of the magnetostriction based power take off units which are able to production energy from the entire spectrum of the wave input [75].

After identifying the proportionality constant the model is compared against other data sets during the same storm. For reasons of propriety Table 2.1 only shows the error associated with the predicted power.

Table 2.1 shows the error between the power production from the WEC and the predicted power production from the time domain model. T_D is the dominant period and H_s is the significant wave height of the input. From this table it is shown that the time domain model has reasonable certainty given the simplified nature of the wave model. The assumption of a purely random phase also adds a small amount of uncertainty when determining the coefficient to predict the power generation of the system.

2.5 Sensitivity Analysis

By using a reference data set it is possible to perform a sensitivity analysis by changing parameters and computing the new power production. The analysis is performed in two stages, first varying each adjustable parameter by positive 5% and then positive 20%.

Table 2.2: Proportional power change: $\%\Delta\mathbb{P}_1$ is the change in power production when the parameter is changed by +5%, $\%\Delta\mathbb{P}_2$ is the change in power production when the parameter is changed by +20%.

Parameter	Initial Value	$\%\Delta\mathbb{P}_1$	$\%\Delta\mathbb{P}_2$
Buoy mass	570kg	0.3%	0.7%
PTO mass	260kg	1.0%	4.6%
Heave Plate mass	705kg	-0.6%	10.4%
Buoy added mass	220kg	0.5%	0.7%
PTO added mass	10kg	0.5%	0.7%
HP added mass	260kg	1.3%	3.5%
Spring: K_{r1}	5,400,000 $\frac{N}{m}$	0.9%	1.2%
Spring: K_{r2}	1,080,000 $\frac{N}{m}$	0.2%	0.3%
Buoy buoyancy	22,260$\frac{N}{m}$	3.5%	11.6%
PTO buoyancy	175 N	0.5%	0.3%
HP buoyancy	1000 N	0.5%	0.1%
Buoy drag, D_b	$D_b = 5,000\frac{Ns}{m}$	-1.3%	-6.5%
PTO drag, D_p	$D_p = 110\frac{Ns}{m}$	0.8%	-0.0%
HP drag, D_h	$D_h = 1,450\frac{Ns}{m}$	-0.1%	-0.6%

Table 2.2 shows the parameters that are varied in the sensitivity analysis along with the corresponding values used in the simulation. It can be seen that the greatest effect on the power production is the mass of the heave plate and the buoyancy of the buoy. This implies that the system is dominated by the inertia of the components and entrained fluid rather than the drag, as may be expected. Despite the great effect the buoyancy of the buoy has on the power production it may be that a disproportionately large buoy is not plausible. The heave plate parameters also have significant impact on the performance of the WEC. Table 2.2 shows that by increasing the mass of the heave plate or by increasing the mass of the fluid entrained by the heave plate the total power production will be increased.

As shown in Table 2.2, a significant change in the estimation of the added mass of the buoy does not produce a significant change in the estimated power production. Likewise, a

dramatic increase in both spring constants produces less than a 1.5% change in the power production. A change in the stiffness of the connections between masses can be a result of a change in the spring constant or a change from the modeled 4 meter natural length of the connections. The buoy drag also has a non trivial negative effect on the power generation of the WEC.

In the sensitivity analysis it is important to recognize that the power production is not based on the tension that the PTO units are subjected to, but rather the time rate of change of the tension. Careful consideration should be taken when considering the effect that parameters will have on a point absorber WEC with a different power take out.

2.6 Conclusion

This paper presents an approach to the modeling and validation of a multiple body point absorber wave energy converter. By forming the equations of motions from first principles, rather than using a commercial hydrodynamics package, a model is established for the development of control aimed at reducing the cost of producing energy with arrays of wave energy converters. The equations of motion are developed and then linearized with the goal of validating the amplitude spectrum with experimental data.

Simulations are performed using both spectral and time domain methods using MATLAB to validate the amplitude spectrum of the acceleration of the wave energy converter. After determining a model for the wave input based on incident wave data taken during the deployment, a time domain simulation is used to estimate the power production of the system. A linear proportionality constant is used to relate the time rate of change of tension, applied to the power take off units, to the power generated. The model is then used to compare the predictions with the experimental power production for several different time intervals.

Finally, a sensitivity analysis was used to show that this system is dominated by inertia more than drag. As a result, the design of the system should pay careful attention to the mass of each component and the added mass of the entrained fluid. The heave plate is also shown to be an important component for the performance of the system. The fluid drag

and the weight of the heave plate must ensure that the PTO units are never in slack conditions, while not producing an adverse effect on the power production as demonstrated in the sensitivity analysis.

Chapter 3

MODELING AND ANALYSIS OF THE TIME DOMAIN FORCES OF A WAVE ENERGY CONVERTER MODEL

The text of the following chapter was accepted for publication in the 3rd Marine Energy Technology Symposium (METS) in 2015. For the preparation of this document a numerical mistake was rectified which results in changes to figures 3.3 and 3.4. The revised figures show larger magnitudes of the force resulting from the radiated when compared to the original article as accepted. However, all results presented in this document are consistent with the original article as accepted. With the exception of reformatting the text no changes were made to the content of the article as accepted. The citation for the paper, Ref. [29], is as follows:

Andrew F. Davis and Brian C. Fabien. Modeling and analysis of the time domain forces of a wave energy converter model. In *Proceedings of the 3rd Marine Energy Technology Symposium*, 2015.

3.1 Introduction

Wave Energy Converters (WECs) have been the subject of a great deal of research and development in recent years. Reviews of WEC concepts and modeling methods are found in [8]. Point Absorbing (PA) wave energy converters were chosen for this study for their deployment versatility and simplified heave dynamics. Since some control strategies are developed for WECs to produce maximum displacements, understanding the nonlinear dynamics of WECs has become increasingly important. The primary motivation of this work is determine the contribution of each force on the WEC, to enable the future development of control strate-

gies. By using time domain simulations the predicted nonlinear forces are quantified in a way that shows the contribution of each force. The relative contribution of each force as well as the quantification of the discrepancies between some analytical and numerical methods are performed in order to inform future experiment design decisions. This well developed modeling method is analyzed as it may be suitable for implementation on microcontrollers usable for lab scale controls testing.

While the formulation of the numerical simulation of a heaving WEC is understood, the relative force contributions in the time domain is an area of current research [103] and is studied in this work. While WEC analysis can be performed using spectral methods as shown in[45], the future application of this model in control system development lends itself to the time domain methods used in this work. Here, the differences between an analytical formulation of radiation force and boundary element method calculations are quantified by comparing the forces calculated by each method. The last topic addressed in this work is the effect of the wave climate and characteristic dimension on the relative contribution of each force.

Section 3.2 provides the nonlinear model based on the work done in [32]. The modifications of the previous model include a quadratic Morison drag term, a state-space realization of the convolution integral for radiation force, and the inclusion of the wave excitation force. Section 3.3 gives a description of the analysis of a lab scale heave PA device which will give rise to the decomposition of forces not only as a function of wave climate but also geometry. Section 3.4 discusses the time domain contributions of the forces acting on the heaving WEC for various characteristic lengths and wave climates. Section 3.5 provides concluding analysis and directions of future work for this research.

3.2 Nonlinear WEC Model

To simplify the analysis, only the float portion of the WEC is considered when formulating the Equation of Motion (EOM). By constructing the nonliner EOM for the float at the surface, all subsequent components can be modeled in a similar manner. The model of the

Oscilla buoy was the basis for this work and was set up as a three body WEC with spring forces coupling the motion of the components [32]. The general EOM of a WEC body float is

$$M_v\ddot{y} = -F_W + F_b - F_D + F_{PTO} - F_R + F_{F-K} + F_d, \tag{3.1}$$

where the inertial force of the object is the product of the virtual mass, M_v and the heave acceleration $\ddot{y}$. The virtual mass is the sum of the infinite frequency added mass and the dry mass of the object [26]. The non-inertial forces are defined as: the weight of the object is F_W, the buoyant force is F_b, the viscous drag force is F_D and the power take off forces are F_{PTO}. The radiation force is F_R, the Froude-Krylov force is F_{F-K}, and the wave diffraction force is F_d. The forces are shown for a simple geometry in Fig. 3.1. The displacement of the body is y, the displacement of the wave is y_w and the dot notation represents derivatives with respect to time. Equation (3.1) can be simplified as follows:

$$M_v\ddot{y} = F_B - F_D - F_R + F_{ex}, \tag{3.2}$$

where F_B is the weight of the object combined with the buoyant force to create the hydrostatic restoring force. The Froude-Krylov force and the wave diffraction force are summed together and represented as the wave excitation force, F_{ex}. Since the purpose of this work is to evaluate the uncontrolled forces acting on the WEC the power take off forces will be removed. The drag, radiation, and excitation forces have been reformulated from the work in [32] as shown below.

3.2.1 Morison Drag Term

The viscous drag can be simulated using a quadratic Morison drag form [20, 103]. The drag in the heave direction is given by $F_D = \frac{1}{2}\rho A_p C_D V|V|$, where V is the relative velocity of the object and the water particles surrounding it. Water particle velocities are computed

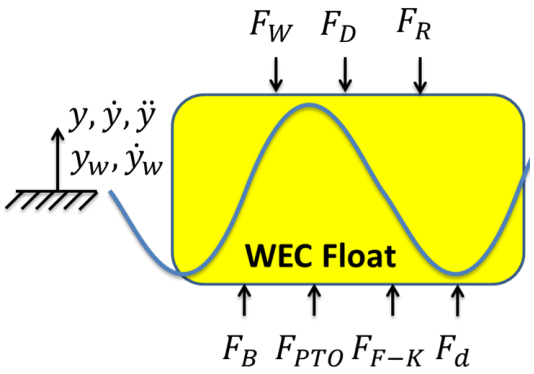

Figure 3.1: The coordinates and forces acting on a heaving object in waves.

using linear Airy wave theory. The density of the fluid is given by ρ, and A_p is the projected area of the object in the heave direction. The drag coefficient, C_D, can be determined using lookup tables or experimentally as in [103]. A signed velocity square term is computed by taking the product of velocity, V, and the absolute value of the velocity, $|V|$.

3.2.2 Excitation Force

The wave excitation force is modeled as the sum of the diffraction force and the Froude-Krylov force. The diffraction force is the force on the heaving body due to the body disturbing the incident waves. The Froude-Krylov force is caused by the unsteady pressure field generated by undisturbed waves [20]. The sum of these two forces is commonly given as the frequency domain wave excitation force by Boundary Element Method (BEM) codes such as NEMOH [7]. Given a particular object geometry the excitation force, $F_X(\omega)$, is computed by NEMOH as a function of frequency. In order to simulate the regular wave excitation force in the time domain a single frequency is chosen and the amplitude of the excitation force becomes the coefficient of a sinusoidal function. For regular waves the excitation force is given by $F_{ex} = \mathbb{R}\left[\frac{H}{2}F_X(\omega_r)e^{i(\omega_r t)}\right]$, where $\mathbb{R}$ represents the function to extract the real part of the argument, H is the peak to peak wave height, and $F_X(\omega_r)$ is the magnitude of the frequency

domain excitation force for a given frequency, ω_r. The imaginary unit is donated by i, and t is the time in seconds. This excitation force can be generalized to irregular waves by $F_{ex} = \mathbb{R}\left[\int_0^\infty \sqrt{2\Delta\omega_r S(\omega_r)} F_X(\omega_r) e^{i(\omega_r t+\phi)}\right]$, where $S(\omega_r)$ is the power of the wave spectrum as a function of frequency. The variable $\Delta\omega_r$ is the discrete distance separating each frequency and ϕ is a random phase angle in radians [52].

3.2.3 Radiation Force

The radiation force of the heaving WEC is the energy lost due to radiated waves. The standard method of computing radiation force is formulated in the frequency domain by a BEM program. The frequency domain forces are simulated in the time domain through the use of the convolution integral as illustrated in [26]. A state-space (SS) realization of the convolution integral is created as an efficient method of computing the radiation force. The standard formulation of the radiation force at a given time t is given by $F_R = \int_{-\infty}^{t} K_r(t-\tau)\dot{y}(\tau)d\tau$, where K_r is the kernel of the convolution integral. This is the impulse response function of the radiation force [94]. The variable τ is the dummy variable of integration, and $\dot{y}(\tau)$ is the heave velocity of the oscillating object as a function of time. The SS representation can be formed as

$$\dot{X}_r(t) = A_r X_r(t) + B_r \dot{y}(t), \tag{3.3}$$

$$F_R = \int_{-\infty}^{t} K_r(t-\tau)\dot{y}(\tau)d\tau = C_r X_r(t) + D_r \dot{y}(t), \tag{3.4}$$

where X_r is the state variable of the realization. The state matrices A_r, B_r, C_r, and D_r are a non-unique linear realization of the convolution integral and are generated from the impulse response function [57].

To generate the impulse response function, the methods shown in [94] are used. The radiation damping is given by $\beta(\omega) = \beta_\infty + \int_0^\infty K_r(t)\cos(\omega t)dt$. The radiation damping at an infinite frequency is denoted by β_∞. The frequency is ω in radians per second and the time is given by t. Applying the inverse the Fourier transform to the radiation damping gives

Table 3.1: Statistical summary of radiation force on a heaving hemisphere and vertical cylinder. Mean, Maximum (Max.), and Standard Deviation (Std. Dev.) are shown.

Hemisphere	Hulme [N]	NEMOH [N]	% Difference
Mean Force	105.6	101.5	-3.9
Max. Force	310.4	291.9	-5.9
Std. Dev.	74.3	71.9	-3.3
Cylinder	Falnes [N]	NEMOH [N]	% Difference
Mean Force	28.8	27.1	-5.8
Max. Force	97.0	88.1	-9.1
Std. Dev.	21.5	19.7	-8.3

the impulse response function $K_r(t) = \frac{2}{\pi}\int_0^\infty [\beta(\omega) - \beta(\infty)]\cos(\omega t)d\omega$. Since the radiation damping tends toward zero at high frequencies, $\beta_\infty = \beta(\infty) = 0$, $K_r(t)$ becomes easy to evaluate.

As proposed in [57] the SS model is chosen using the Hankel singular value decomposition. This is done using the MATLAB function 'IMP2SS.' By specifying a sampling time and the impulse response function a high order linear system realization of K_r is determined. Since high order matrices can be computationally difficult for simulation, another function, 'BALMR', is used in MATLAB to reduce the dimension of the realization matrices. This function uses a balanced model reduction to reduce the order of the SS matrices from hundreds to less than 10 with no appreciable difference in the force influence on the object.

Comparison of Radiation Forces

The accuracy of numerical simulations is an important factor when evaluating the radiation force of a system. A comparison is performed between the radiation force determined from analytical methods and BEMs. To do this comparison the analytical radiation damping and added mass from two geometries will be compared to the BEM calculations from NEMOH for the same geometries [7]. The first geometry is a hemisphere with a radius of one meter [53]. The second geometry is a vertical cylinder with a radius of one meter and a draft equal

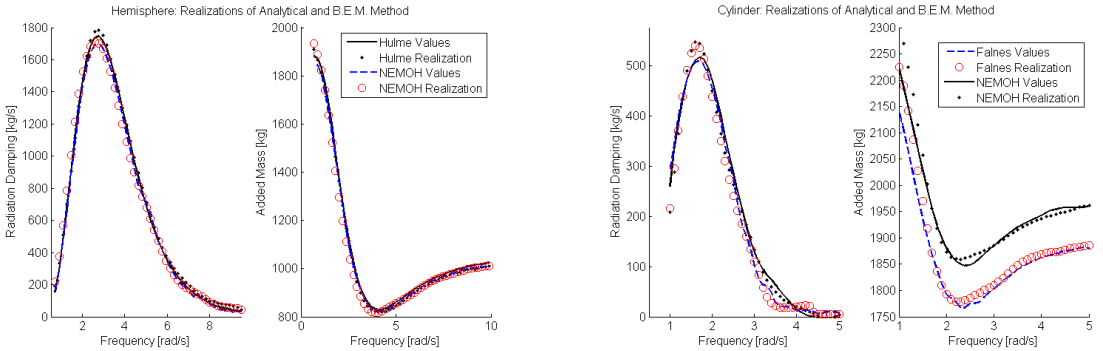

(a) The comparison of method by Hulme [53] and NEMOH [7].

(b) The comparison of solution from Falnes [42] and NEMOH [7].

Figure 3.2: The analytical and numerical comparison of the radiation damping and added mass coefficients. Realizations with system order 10 are overlayed for comparison.

to 1.88 meters [42]. Comparing the radiation from BEM to analytical solutions of simple geometries is necessary since analytical solutions are unavailable or difficult to obtain for complex geometries, whereas the radiation for complicated geometries is easily determined with a BEM package.

Figure 3.2 shows that there is a reasonable comparison for the shapes of the frequency dependent radiation damping and added mass between analytical and numerical results. It can however be seen that while the analytical and numerical coefficients for the hemisphere match well, the two methods calculate an infinite frequency added mass that differs by approximately 75 kg for the cylinder. Table 3.1 shows a comparison of radiation forces incurred in time domain simulations using the SS realizations for both analytical and BEM calculations. A peak period of two seconds and a significant wave height of 0.5 meters are used as the parameters for the Bretschneider spectrum to determine the wave climate. The sum of linear waves, with randomized phase and amplitudes determined by the spectrum, are used to determine an irregular wave input velocity. The simulations show that the relative differences in the calculated force between the above methods is insignificant for these geometries.

3.3 Model Evaluation

The work done in [103] was an attempt to experimentally validate the time domain forces on a heaving PA wave energy converter. The tests were performed on a lab scale WEC. To model the lab scale prototype several distinctions must be made between the model described above and the model used in [103]. The lab scale device relies on a PTO unit that generates power from an arm moving with the waves while the rest of the WEC is grounded to the ocean floor using piles. The floats of the WEC trace out a constant radius path so the equation of motion is formulated by summing torques about the joint attaching the float arm to the body of the WEC. Many of the standard force formulations described above are used for determining the forces on the float in the heave direction, then the moment arm is used to calculate the torque that is applied to the PTO unit.

The hydrostatic restoring force is experimentally determined and defined as a function of the angular displacement of the arm with respect to the equilibrium position. The drag term must also include a horizontal component with respect to the wave since the float has some displacement in both the vertical and horizontal directions. It should be noted that the Morison drag in this work as shown in section 3.2.1 is formed using the density of the fluid whereas the density term is omitted in [103].

The frequency domain terms such as wave excitation force and radiation force are formulated using a rotational torque in WAMIT. From this formulation of the hydrodynamic forces a heave motion input will produce a torque output.

Incorporating the experimental measurements and frequency domain coefficient of [103] produced Fig. 3.3 which shows the normalized torques acting on the lab scale device for various wave conditions. The wave conditions are given in Table 3.2. In each case the wave climate is generated using the Bretschneider spectrum. The control torque is removed from the model to allow for the fluid forces acting on the float have a more significant contribution. The torques are normalized by dividing by the hydrostatic torque because it has the most significant contribution. For the simulations used to produce Fig. 3.3 the length of the float

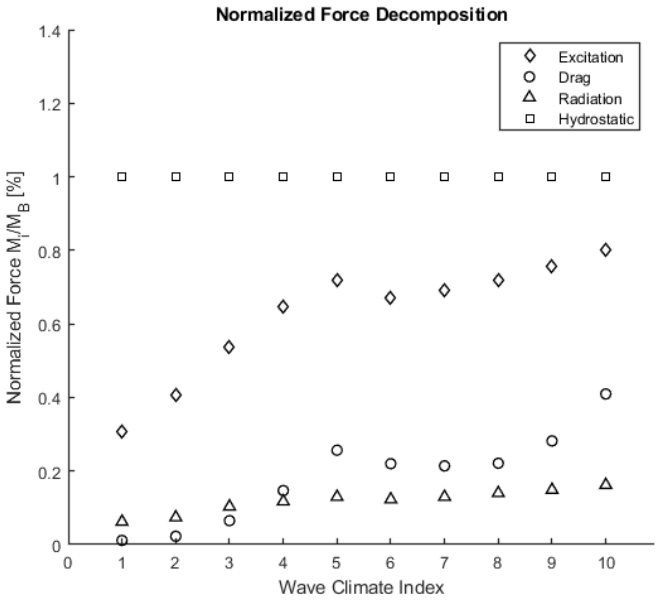

Figure 3.3: The normalized mean torques acting on the WEC for various wave conditions described in Table 3.2.

arm is $0.68m$, the diameter of the float is $0.254m$, the mass moment of inertia is $0.778kgm^2$, the linear hydrostatic stiffness is $87\frac{Nm}{rad}$, the nonlinear hydrostatic stiffness is given in [103], and the draft of the buoy is $0.104\ m$. With the draft less than half the diameter, the profile of the float will be that of a hemisphere. The drag coefficients are assumed to be 0.2 in the vertical direction and 0.4 in the horizontal direction and the infinite frequency added inertia is $0.3656kgm^2$. Two sets of spline interpolations were performed to recreate the excitation force and radiation force. For the excitation force the frequency values, in $\frac{rad}{s}$, were $[0, 2, 4, 6, 8, 10, 12]$ and the magnitude values, in $\frac{Nm}{m}$, were $[200, 192, 160, 121, 85, 61, 41]$. For the radiation damping the frequency values, in $\frac{rad}{s}$, were $[0, 5, 10, 15, 20, 25]$ and the magnitude values, in $\frac{Nm}{m}$, were $[0, 1.25, 2.575, 1.95, 1.225, 0.8250]$ [103].

Figure 3.3 illustrates that as the wave climate becomes more energetic the excitation force and viscous drag force will play a more significant role in the dynamics of the float than the radiation force.

Table 3.2: Wave Conditions used in Fig. 3.3

Number	1	2	3	4	5
T_P [s]	0.80	1.25	1.30	2.50	3.00
H_s [m]	0.027	0.044	0.062	0.080	0.120
Number	6	7	8	9	10
T_P [s]	0.85	1.30	1.35	2.50	3.00
H_s [m]	0.055	0.090	0.115	0.155	0.232

3.4 Forces on Body: Extension to Various Waves and Geometries

Using the simple cylindrical geometry from section 3.2, Fig. 3.4 was generated to visualize the relative contribution of each force acting on the heaving body. The wave climates were formed by evenly increasing the steady wind speed of a Pierson-Moskowitz spectrum from $5m/s$ to $25m/s$ [52]. The other variable considered in this section is the characteristic length of the WEC body. The radius of the vertical cylinder is varied from $1m$ to $10m$. The frequency domain excitation and radiation terms were computed using NEMOH for the geometry mentioned in section 3.2. The drag coefficient was assigned a value of 1.7 as in [32].

Figure 3.4 shows that the forces are greatest in the high energy wave states, and the forces acting on the body increase as the radius of the body increases. According to this method of simulating the dynamics, the radiation force will contribute significantly less than the viscous drag. The excitation force contributes significantly to motion of the buoy, however, for the simulated conditions, it is always smaller in magnitude than the hydrostatic force.

3.5 Conclusions

This paper presents an approach to the modeling of a single heaving component of a wave energy converter. The equations of motion are formed using a Cummins equation method with an added Morison drag term in an attempt to quantify the contribution of each force on the response a of wave energy converter. A brief comparison of the radiation force is

performed between analytical and numerical methods for a hemisphere and vertical cylinder which shows only small differences in the computed force. An evaluation of the forces on a lab scale wave energy converter is given in which excitation force and viscous drag coefficients were experimentally determined. The evaluation of the lab scale device shows that as the wave climate becomes more energetic the viscous drag becomes much larger than the radiation force and that the excitation force approaches the magnitude of the hydrostatic force. Finally the forces on a vertical cylinder are simulated for a range of wave climates and characteristic lengths. The results of the simulations show that larger mean forces result from larger geometries and wave inputs, the large disparity between the radiation force and viscous drag forces show that this model predicts the vicious drag to be much more significant for the dynamics of the wave energy converter.

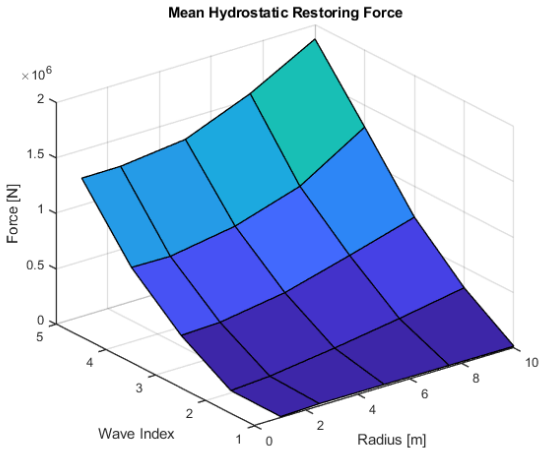

(a) The hydrostatic restoring force

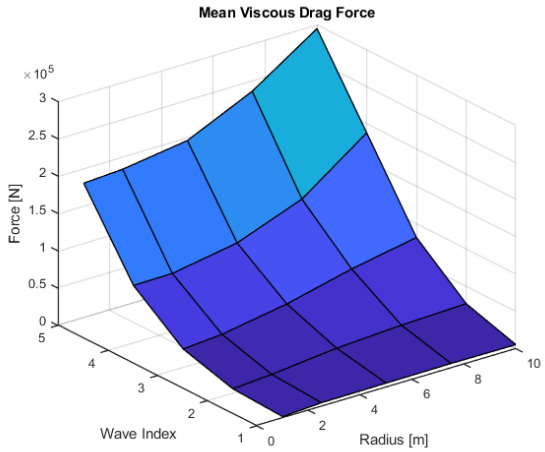

(b) The viscous drag

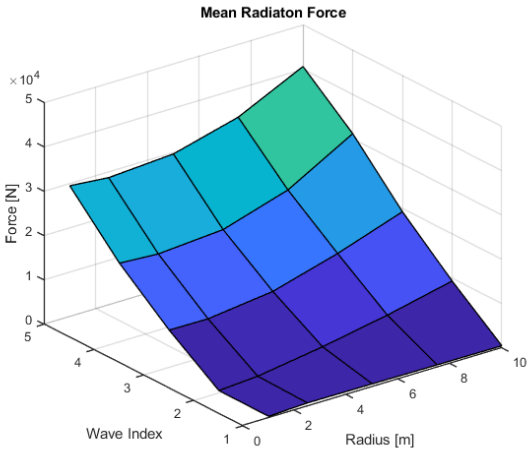

(c) The radiation force

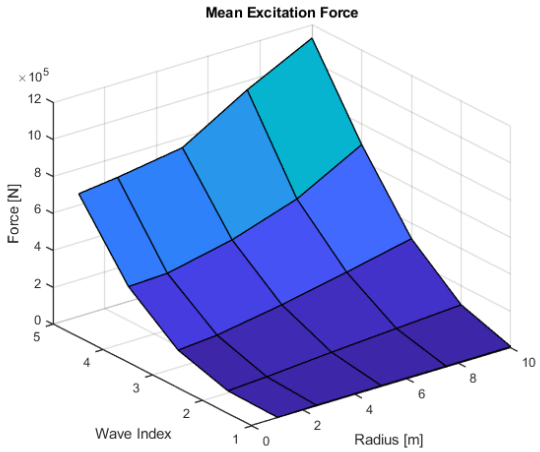

(d) The wave excitation force

Figure 3.4: The forces acting on a vertical cylinder in heave for varied geometry and wave climate.

Chapter 4

SYSTEMATIC IDENTIFICATION OF DRAG COEFFICIENTS FOR A HEAVING WAVE FOLLOWER

The text of the following chapter was accepted for publication in the Journal of Ocean Engineering in 2020. With the exception of reformatting the text and the correction of typographical errors no changes were made to the content of the article as accepted. The citation for the paper, Ref. [31] is as follows:

Andrew F. Davis, and Brian C. Fabien. Systematic identification of drag coefficients for a heaving wave follower. *Journal of Ocean Engineering*, 168, 2018.

4.1 Introduction

Wave Energy Converters (WECs) have been the subject of a great deal of research and development in recent years. Reviews of WEC concepts and modeling methods can be found in [33, 43, 63, 44]. Since some control strategies are developed for WECs to produce maximum displacements, understanding the nonlinear dynamics of WECs has become increasingly important. The nonlinear drag term in particular has become important as the oscillations have become large. The primary motivation of this work is to implement a systematic way of determining the viscous drag coefficient and to enable the future development of control strategies. Point absorbing (PA) wave energy converters were chosen for this study for their deployment versatility and simplified heave dynamics.

The equation of motion for point absorbing WECs traditionally comes from the Cummins equation [26], originally developed for ship dynamics [44, 42]. Optimal control strategies in high energy sea states necessitate a nonlinear drag term for wave energy converters [103, 16]. A quadratic drag term known as the Morison drag has been included in the model [8], in order

to avoid non-physical simulation amplitudes. The quadratic drag term is typically the first nonlinear term that is added to the linear Cummins model. The Morison term comes from the Morison equation which is a semi-emperical description of the forces exerted on vertical slender cylinders, piles, in oscillatory flows [73]. While the drag term is meant to quantify the viscous losses of a heaving body, its implementation has become very unsystematic [8, 63] and has been shown to have a significant effect on the predicted power of wave energy converters [8]. As a result the standard way of determining the drag coefficient is to tune the numerical model of a WEC to experiential data [12].

A filter on board the WEC that can be used to identify the current drag coefficient would be useful when implementing a wide range of control methodologies. One of the most prominent WEC control methods, model based control, also requires knowledge of the states of the controlled system. An algorithm that combines identification and state observation would minimally increase the computational burden on the WEC.

The first goal of this work is to implement a systematic method for determining the drag coefficient of WECs in a way that will be useful when implementing a control system. The second purpose is to compare several lumped parameter WEC models. This work examines three low computational cost lumped parameter models of heaving point absorbing WECs. These models are used in an Extended Kalman Filter (EKF) to estimate the states and identify the drag acting on the heaving object. The effect of model choice on the observation and identification is discussed.

An EKF is used to identify the unknown drag coefficient. A filtering algorithm was chosen for this work because it affords potentially significant contributions to the WEC control systems such as real time state observation, parameter estimation, and wave excitation force estimation [64]. Each model was applied to the experimental work performed by [13], which is described in section 4.3. The experimental data provided by [13] enabled a performance evaluation of each model in regular wave situations.

The application of Kalman filters on WECs is not novel, the use of Kalman filters to estimate the wave excitation force is described in [64] and they have been mentioned in

control system research papers such as [14]. However, there is very little literature discussing the implementation of these filters, particularly the EKF. Furthermore, the identification of drag coefficients on WECs is a research area in need of more development as described by [12, 17]. To fill in some gaps in the literature, this work develops several aspects of implementing a Kalman filter that need to be addressed prior to widespread use on WECs.

Firstly, each state in a dynamic model undergoes a "random walk" process in a Kalman filter algorithm [24]. In this work the EKF algorithm is modified to allow for a state space realization of the radiation force to be including in the dynamics without the "random walk". This is necessary due to the fact that variations in the radiation force states can cause an otherwise stable dynamic system to have non-physical behavior. Another prominent issue with implementing a Kalman filter on any device is the uncertainty of process noise. To solve this problem a systematic initial value of the process noise covariance based on easily measurable information is given. Finally, multiple models are tested using numerically generated data to evaluate the effectiveness of these models for state observation and drag identification.

The models used in this work are discussed in section 4.2. The experimental tests that the models describe and that are used for initial validation are described in section 4.3. A broad description of the EKF used in this work is found in section 4.4, and a detailed description of the filtering algorithm used is found in Appendix A. The results of estimation and observation that was simulated are discussed in section 4.5. Concluding remarks about identification and model choice are presented in section 4.6.

4.2 WEC Models

The most typical form of the Equation of Motion (EOM) of a point absorbing WEC is the potential based time domain integro-differential equation found in [8]. However, semi-emperical models or simplified lumped parameter models are also possible for WECs, which will be discussed in addition to the traditional EOM. Each model described below will be applied to the experimental situation described by [13]. The devices and testing conditions

found in [13] are also briefly described in section 4.3.

4.2.1 Potential Time Domain Model

The equation of motion of a semi-submerged body about the center of gravity in heave is given by

$$M\ddot{y} = -F_W + F_b + F_D + F_{PTO} + F_R + F_{F-K} + F_m + F_u + F_d + F_I, \tag{4.1}$$

where the inertial force of the object is the product of the mass, M, and the heave acceleration, $\ddot{y}$. The terms used in (4.1) are defined as: F_W is the weight of the object, F_b is the buoyant force, F_D is the viscous drag force, F_{PTO} is the power take off force, F_R is the radiation damping, F_{F-K} is the Froude-Krylov force, F_m is the force applied by the mooring lines, F_u is the force applied by the umbilical cable, F_d is the wave diffraction force, F_I is the added mass force, and the displacement of the body is y. The added mass force is computed by $F_I = m_a\ddot{y}$, where m_a is the added mass. The dot notation shown above represents derivatives with respect to time.

To simplify the EOM from (4.1) the weight of the object is combined with the buoyant force to create the hydrostatic restoring force, F_B. The added mass force is absorbed into a "virtual mass," M_v, which is the added mass of the fluid and the mass of the body. This "virtual mass" is given by the sum of the infinite frequency added mass and the dry mass of the object, as is traditionally used in the Cummins formulation [26]. The Froude-Krylov force and the wave diffraction force are commonly summed together and represented as the wave excitation force, F_{ex}. A combined force applied to the float, F_M, takes into account the force from the mooring lines as well as the umbilical cable as shown by

$$M_v\ddot{y} = F_B + F_D + F_R + F_M + F_{ex}. \tag{4.2}$$

Since the purpose of this work is to evaluate the ability to observe and identify the uncontrolled states F_{PTO} is removed to get from (4.1) to (4.2).

The potential based force terms of (4.2) are developed in agreement with the Cummins equation [26] which is a model originally developed to describe the motion of ships and is now applied to floating bodies. Inertial, excitation, restoring, and radiation forces are assumed to be linear in the following development. The viscous drag term is the lone nonlinear term as shown in [8, 12]. The following subsections describe each force in the development of the potential based EOM [29].

Morison Drag Term

The viscous drag is simulated using a quadratic Morison drag form [20, 103]. The drag in the heave direction is given by

$$F_D = -\frac{1}{2}\rho A_p C_D V|V|, \tag{4.3}$$

where V is the relative velocity between the object and the water particles surrounding it. Water particle velocities are computed using linear Airy wave theory [20]. The density of the fluid is given by ρ, and A_p is the projected area of the object in the heave direction. A signed velocity square term is computed by taking the product of velocity, V, and the absolute value of the velocity, $|V|$. Finally, the drag coefficient is given by C_D.

Throughout the contemporary literature there is a wide variety of treatments of viscous drag coefficients for WECs. Heave plate drag coefficients are a current area of research [17]. The drag coefficient can sometimes be determined using lookup tables or experimentally as in [103]. However, often lookup tables prove to be insufficient and experimental tests are unavailable. Numerical research methods have also been recently applied with system identification methods to determine the drag coefficients of WEC bodies using computational fluid dynamics or numerical wave tank simulations [12, 27, 49].

The nonlinear, relative velocity Morison drag term is well represented among WEC mod-

eling software packages such as WEC-sim, Inwave, WaveDyn, and ProteusDS [23]. Research work using a relative drag term for a semi-submerged WEC body can also be seen in [103, 34]. Use of a nonlinear drag term where the drag coefficient was intentionally over estimated can be found in [95], and a case where the drag term is linearized can be found in [10]. As illustrated in [8, 23], drag terms are often used as viscous correction terms where the unmodeled nonlinear effects are absorbed into a single quadratic term. Viscous loads, particularly Morison drag terms, are not available for many situations to a satisfactory confidence level in literature. Therefore, if the viscous drag is needed prior to the deployment of the WEC individual free decay or forced oscillation tests are required to determine the value [9].

Excitation Force

The wave excitation force is modeled as the sum of the diffraction force and the Froude-Krylov force. The diffraction force is the force on the heaving body due to the body disturbing the incident waves. The Froude-Krylov force is caused by the unsteady pressure field generated by undisturbed waves [20]. The sum of these two forces is commonly given as the frequency domain wave excitation force by Boundary Element Method (BEM) codes such as NEMOH [7]. Given a particular object geometry, the excitation force, $F_X(\omega)$, is computed by NEMOH as a function of frequency. In order to simulate the wave excitation force in the time domain a single frequency is chosen and the magnitude of the excitation force becomes the coefficient of a sinusoidal function. For regular waves the excitation force is given by

$$F_{ex} = \mathbb{R}\left[\frac{H}{2}F_X(\omega_r)e^{i(\omega_r t)}\right], \tag{4.4}$$

where $\mathbb{R}$ represents the function to extract the real part of the argument, H is the peak to peak wave height, and $F_X(\omega_r)$ is the magnitude of the frequency domain excitation force for a given frequency, ω_r. The imaginary unit is donated by i, and t is the time in seconds. This

excitation force can be generalized to irregular waves by

$$F_{ex} = \mathbb{R}\left[\int_0^\infty \sqrt{2\Delta\omega_r S(\omega_r)} F_X(\omega_r) e^{i(\omega_r t+\phi)} d\omega_r\right], \tag{4.5}$$

where $S(\omega_r)$ is the power of the wave spectrum as a function of frequency. The variable $\Delta\omega_r$ is the discrete distance separating each frequency and ϕ is a random phase angle in radians [52].

Radiation Damping

The radiation damping of the heaving WEC is the energy lost due to radiated waves. The standard method of computing radiation damping is formulated in the frequency domain by a BEM. The frequency domain forces are simulated in the time domain through the use of the convolution integral as illustrated in [26]. A state space realization of the convolution integral is created as an efficient method of computing the radiation force. The standard formulation of the radiation damping force at a given time t is given by

$$F_R = -\int_{-\infty}^{t} K_r(t-\tau)\dot{y}(\tau)d\tau, \tag{4.6}$$

where K_r is the kernel of the convolution integral which is the impulse response function of the radiation damping. The variable τ is the dummy variable of integration, and $\dot{y}(\tau)$ is the heave velocity of the oscillating object as a function of time. The state space representation can be formed as

$$\dot{X}_r(t) = A_r X_r(t) + B_r \dot{y}(t), \tag{4.7}$$

$$F_R = -\int_{-\infty}^{t} K_r(t-\tau)\dot{y}(\tau)d\tau = -C_r X_r(t) - D_r \dot{y}(t), \tag{4.8}$$

where X_r is the state variable of the realization. The state matrices A_r, B_r, C_r, and D_r are a non-unique linear realization of the convolution integral and are generated from the impulse

response function [57].

To generate the impulse response function, the methods developed in [81] are used. The radiation damping is given by

$$\beta(\omega) = \beta_\infty + \int_0^\infty K_r(t) cos(\omega t) dt. \tag{4.9}$$

In (4.9) β_∞ is the radiation damping at an infinite frequency. The frequency is ω in radians per second, and the time is given by t. Applying the inverse Fourier transform to (4.9) gives the impulse response function

$$K_r(t) = \frac{2}{\pi} \int_0^\infty [\beta(\omega) - \beta(\infty)] cos(\omega t) d\omega. \tag{4.10}$$

Since the radiation damping tends toward zero at high frequencies, $\beta_\infty = \beta(\infty) = 0$, (4.10) becomes easy to evaluate.

As proposed in [57] the state space model is chosen using the Hankel singular value decomposition. This is done using the MATLAB function "IMP2SS." By specifying a sampling time and the impulse response function a high order linear system realization of K_r is determined. Since high order matrices can be computationally difficult for simulation, another function, "BALMR", is used in MATLAB to reduce the dimension of the realization matrices. This function uses a balanced model reduction to reduce the order of the state space matrices from hundreds to less than 10 with no appreciable difference in the force influence on the object.

For this work the residual sum of squares was used to determine if the state space realization was sufficiently accurate. The residual sum of squares, sometimes called the coefficient of determination, is given by the expression

$$R^2 = 1 - \frac{\Sigma(K_r - \tilde{K})^2}{\Sigma(K_r - K_m)^2}, \tag{4.11}$$

where K_r is the impulse response function shown in (4.10), $\tilde{K}$ is the impulse response function of the state space realization, and K_m is the mean of the impulse response function given by (4.10). A fourth order state space realization was found to be the smallest realization that exceeded the $R^2 = 0.99$ criteria that was used for this work. To further investigate the state space approximation, first through third order realizations were also implemented with coefficients of determination being $[0.699, 0.978, 0.984]$ respectively.

It is also possible to approximate the radiation force with a single linear term as described in [58]. For this linear approximation it is typical to use the radiation damping coefficient at the peak frequency, ω_p. The radiation damping force can be approximated with a constant coefficient by

$$F_{R-Lin} = \beta(\omega_p)\dot{y}, \tag{4.12}$$

where $\dot{y}$ is the body velocity and β is the frequency dependent radiation damping described by (4.9).

Linear Force Terms

The forces resulting from the mooring lines and umbilical cable are modeled together as the product of a constant parameter and the body displacement. The combined mooring-umbilical force is described by the spring equation

$$F_M = -K_{mu}y, \tag{4.13}$$

where K_{mu} is lumped linear spring constant describing the forces acting on the body by the mooring lines and umbilical cable and y is the displacement from the static equilibrium point. By modeling the response of the body from the equilibrium position, as with the hydrostatic restoring force, a linear relationship is needed to determine the vertical force contribution of the cables as a function of heave position. The spring constant can be

determined experimentally using load cells and displacement measurements.

The hydrostatic restoring force is determined by

$$F_B = -\rho A y, \tag{4.14}$$

where A is the projected area that is being submerged, ρ is the density, and y is the displacement from the static equilibrium. It is important to note that (4.14) assumes that a constant area is being submerged. Reference [59] provides insight into the calculation of a nonlinear buoyancy force, however a linear force is sufficient for this work.

4.2.2 Morison Equation

One standard method of modeling the forces acting on a moving body in waves is the Morison equation. The Morison equation was originally developed as a semi-empirical expression to determine the in-line force exerted on fixed slender cylinder in oscillatory flows such as waves [73]. The Morison equation was then adapted to non-stationary objects. Typical limitations of the Morison equation are discussed in [20]. While it is not typical for the Morison equation to be used to determine the heave forces acting on a floating object, there is precedent for this modeling application of the Morison equation found in the offshore marine systems dynamic analysis package OrcaFlex [67]. Orcina's OrcaFlex package uses the Morison equation to determine the hydrodynamic loads on mooring lines and buoys. These loads are then used in the EOM for each simulated degree of freedom. Using the Morison equation, the force acting on the submerged portion of an object is given by

$$F(t) = -\frac{1}{2}\rho A C_d(\dot{y} - U)|\dot{y} - U| - \rho \forall C_l(\ddot{y} - \dot{U}) + \rho \forall \dot{U} \tag{4.15}$$

where $\dot{y}$ and $\ddot{y}$ represent the WEC velocity, and U is the incident water particle velocity in the same direction as y. The displaced volume of the WEC is $\forall$, C_d and C_l are the drag and inertia coefficients respectively, ρ is the fluid density, and A_p is the projected area in

the direction of motion. The first term of (4.15) is the same Morison drag term discussed above, the second term is the inertia force of the fluid and body, and the third term is the Froude-Krylov force. Additional background and discussion of experimental work done to determine the Morison equation coefficients is given by [12].

When using the Morison equation as the basis for the EOM externally applied forces such as mooring, umbilical, PTO, and weight can be dealt with in the same way as in (4.2). The EOM is then given by

$$(m + \rho \forall C_l)\ddot{y} = (1 + C_l)\rho \forall \dot{V} - F_D - F_M + F_B \tag{4.16}$$

where F_D and F_M are the Morison drag term and combined mooring-umbilical forces described by Eqns. 4.3 and 4.13 respectively. The fluid acceleration terms are combined into a single term, $\dot{V}$, which is the time derivative of the relative velocity, V. Here F_B is the same hydrostatic force described previously by (4.14).

4.2.3 Models Used for Study

In this work three models are used when evaluating the observation and identification capabilities of the EKF. The first model used is the widely accepted potential time domain model shown in (4.2). The second model is the semi-emperical Morison equation, described by (4.16) that has been adapted for a semi-submerged object. The third model is a simplified version of (4.2) where the state space realization of radiation is replaced by the linear damping term described by (4.12). This damping term is determined using a frequency domain BEM program and is chosen to be the value at the peak input wave frequency as done in [58]. To investigate the sensitivity of the EKF to model error, three additional versions model number 1 in Table 4.1 are included in section 4.5. These three models only vary the order of the state space radiation realization.

Table 1 shows all three models along with suggested references that describe each model in more detail. The first model is sometimes referred to as a potential time domain model

Model No.	Model	Ref.
1	$M_v\ddot{y} = F_B + F_D + F_R + F_M + F_{ex}$	[12, 34, 103]
2	$(m + \rho V C_l)\ddot{y} = (1 + C_l)\rho V \dot{V} - F_D - F_M + F_B$	[67]
3	$M_v\ddot{y} = F_B + F_D + F_{R-Lin} + F_M + F_{ex}$	[58]

Table 4.1: Summary of the three models used in the extended Kalman filter with references that discuss each model.

with viscous correction. The third model is the same as the first model except the state space radiation realization has been replaced with a linear damping term.

4.3 Modeled Situation

Experimental data was made available by the Oregon State University Northwest National Marine Renewable Energy Center's Marine and Hydrokinetics Open Data Project [79]. The data set that is used for reference in this work was a physical model test of a 1:10 scale floating power system at the COAST lab at Plymouth University [13]. While experimental data is not used in the identification of the drag coefficient, it is used in the development of each numerical model. In order to test the viability of the EKF for WECs the true values must be known and the models must describe a realistic device. The mooring study described in [13] used a wave tank to compare several mooring configurations of two bodies in water. Of these two bodies, the scaled Floating Power System (FPS) is analyzed in this current work as it provides a very similar geometry to that of a point absorbing WEC. The FPS is shown in Fig. 4.1 in the wave tank prior to wave generation.

The Ocean Wave Basin at Plymouth University is 35 meters long, 15.5 meters wide, and 3 meters deep. For the tests studied in [13] the water depth is 2.5 meters and the body was subjected to deep water waves. There were four different mooring configurations tested by [13], one of which was a 3-point compliant mooring configuration and the other three which were 3-point taught mooring configurations using various off the shelf components.

A Qualisys motion capture system was used with six cameras to track 5 markers on each

body providing low noise data on all 6 degrees of freedom for the FPS. A pressure sensor was used to collect incident wave elevation at each of the bodies. Loadcells were used to measure the mooring loads on each body as well as the load applied by an umbilical cable. Incident wave elevation and load cell measurements were measured at 128Hz, and motion data was recorded at a sampling frequency of 200Hz. Free decay tests, monochromatic waves, and panchromatic waves, generated by the Bretshneider spectrum, were measured for various mooring configurations. A LabView measurement program was used to collect loadcell, incident wave elevation, and motion data for each of the four different mooring configurations. While the work described by [13] is meant as a mooring study, the data collected is sufficient for validating models that can be used for evaluating the identification algorithm.

4.3.1 Reproducing Numerical Work

The code used when implementing the EKF to produce the results found in section 4.5 will be made available on a GitHub repository found in Ref. [28]. Monochromatic wave tests using the "o-ring" mooring lines from [13] were used to validate the models used for this paper. The incident waves that were used in section 4.5 were generated using a sum of sine waves according to Airy wave theory [20]. The amplitude for each sine wave was determined using a Bretschneider spectrum with a peak period of 2.69 seconds and a significant wave height of 0.3 meters, and the phase was randomly varied between 0 and 2π radians.

Detailed descriptions of the experiments along with wave tank schematics and dimensioned drawings can be found in the Marine and Hydrokinentics Open Data Project [79]. Key paramters used in the WEC models not found in [13, 79] can be found in Table 4.2. Frequency dependent terms, such as added mass, radiation damping, and wave excitation force are calculated using the BEM code NEMOH [7]. The scripts used to execute NEMOH will be made available on GitHub [28].

The initial conditions for the dynamics used to simulate the WEC are zero for every state except for the drag coefficient state, which must be set to the true value of 0.35. How-

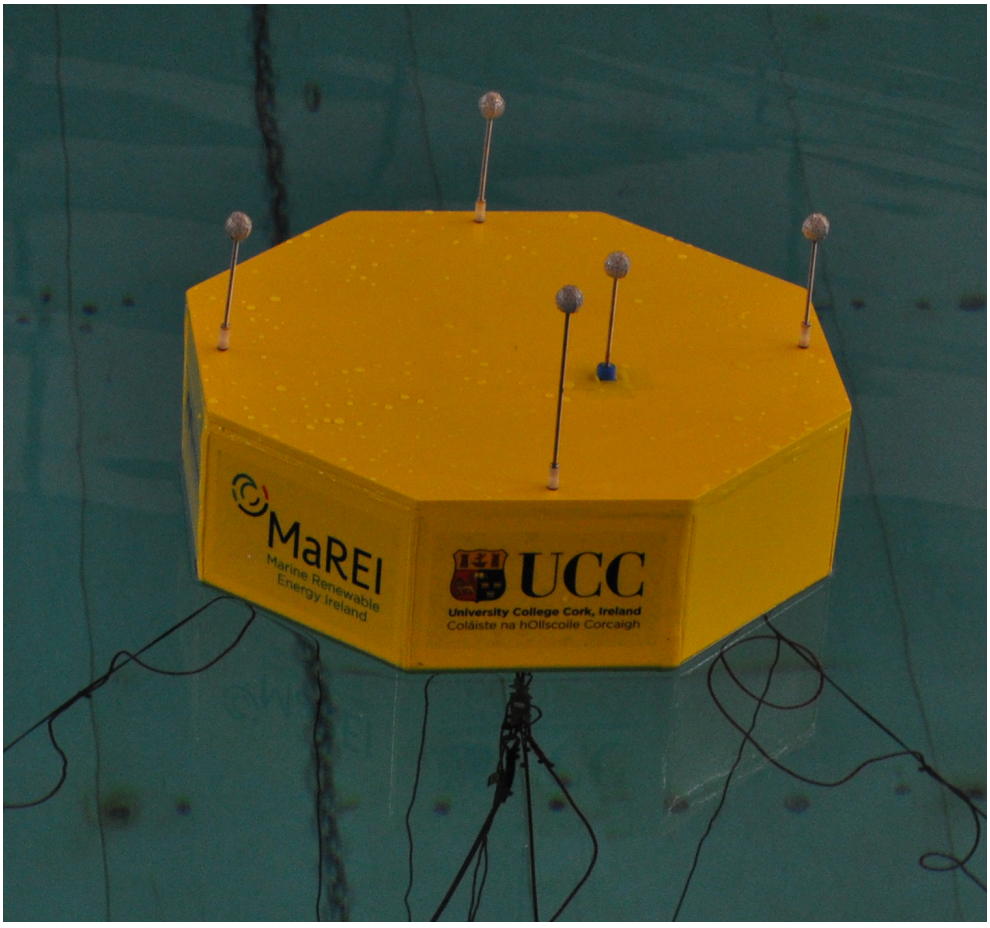

Figure 4.1: The 1:10 scale Floating Power System configured with compliant moorings and umbilical cable described in [13] and made available by the Northwest National Marine Renewable Energy Center's Marine and Hydrokinetics Open Data Project [79].

ever, the identification algorithm is given the erroneous initial conditions of 0.1 m, 0.1 $\frac{m}{s}$, and 1 for the position, velocity, and drag respectively. The initial conditions for the radiation states are always zero. The measurement noise error is Gaussian white noise with a standard deviation of 6.075x10^{-4} m. The measurement noise is randomly generated and added to the state dynamics in the Kalman filter described in section 4.4. The measurement noise was determined by using the position measurement residuals from [79]. The final initial value needed by the EKF is the covariance matrix which is traditionally initialized as the iden-

Parameter	Variables	Value
Fluid Density	ρ	1000 $\frac{kg}{m^3}$
Gravitational Acceleration	g	9.81 $\frac{m}{s^2}$
WEC Mass	M	9.58 kg
Submerged Depth	*	0.075 m
Added Mass (Cummins Based Models)	m_a	21.15 kg
Added Mass (Morison Based Models)	$\rho \forall \dot{U}$	40.0 kg
Mooring And Umbilical Stiffness	K_{mu}	500 $\frac{N}{m}$
Displaced Fluid Volume	$\forall$	1.13x10^{-2} m^3

Table 4.2: Summary of physical parameters used in this work. Parameters are determined to reproduce run number 125 of the 1:10 scale tests available from [79].
* The parameter for submerged depth is not explicitly used in the equations appearing in this paper, but is used when computing the incident water particle velocities.

tity matrix. In this model, due to the small value of each state, the covariance matrix is initialized as the identity matrix and then scaled by the factor 0.1.

4.4 System Identification Method

An Extended Kalman Filter (EKF) is used to observe the state dynamics of the system at the same time as estimating the drag coefficient. A Kalman filter, sometimes referred to as a linear quadratic estimator, uses a series of measurements and a statistical description of the measurement and process noise to generate an estimate of the state dynamics. It is possible to include an extra state in the dynamic model that represents the drag coefficient that will be estimated along with the position and velocity of the system. The two application specific adaptations to the EKF developed in this work are described below and a detailed overview of the entire the EKF is given in Appendix A.

4.4.1 Modifying the Covariance Update

A Kalman filter employs a random walk process with each state in order to determine the best choice of algorithm gains. Whether or not the random variation improves the

accuracy of the state estimates will determine how the next step will be varied. For the state space realization of the radiation damping there is an n^{th} order realization that has been identified to reproduce the same impulse response function as the original convolution integral given by (4.6). This state space realization is highly sensitive to perturbations in the state dynamics, which causes significant instabilities when the state space realization is included in an implementation of a Kalman filter, despite being a linear system on its own. To allow for the state space realization the covariance update equation, (A.5), must be modified to only implement the random walk variations in the states relating to state dynamics. Each row of P_k^+ corresponding to the radiation states in (A.5) is set to a zero vector, preventing the influence of the Kalman gain, K, from modifying the dynamics of the state space realization.

4.4.2 Determining the Process Noise

The process noise, described in section A.2, quantifies the uncertainty in the state dynamics of the model used in the EKF. The true process noise of a model in a given set of experimental conditions is never truly known [24]. This difficulty is made worse in a smooth wave following situation like the conditions described in section 4.3. For the modeled situation in regular waves the primary discrepancies between the model and the experiment are periodic. Kalman filters model process noise as Gaussian white noise which is fundamentally different than the periodic noises for a wave follower model in regular waves. To model a situation where there will be random variation in the dynamics, irregular waves are used in each simulation using the EKF.

The product of the standard deviation of the input wave and the amplitude response of the model will be used as the process noise for the position in the EKF. The model used for this is the first entry in Table 4.1 with a fourth order state space realization and is evaluated at the peak frequency of the irregular wave spectrum. Likewise, the process noise for the velocity in the EKF can be described by the standard deviation of the input position multiplied by the steady state amplitude response of the velocity output to a periodic input.

Further discussion of the process noise estimation is given in section A.4.

4.5 Model Comparison

4.5.1 Idealistic Identification Comparison

When comparing the models described in section 4.2.3 the first comparison of the EKF identification with various models used the high sampling rate described in the experimental tests and an observed position and velocity of the heaving Floating Power System (FPS). By first comparing the EKF identifications in a best case type scenario, it is plausible to eliminate any models that are universally unfit to identify the drag coefficient. Figure 4.2

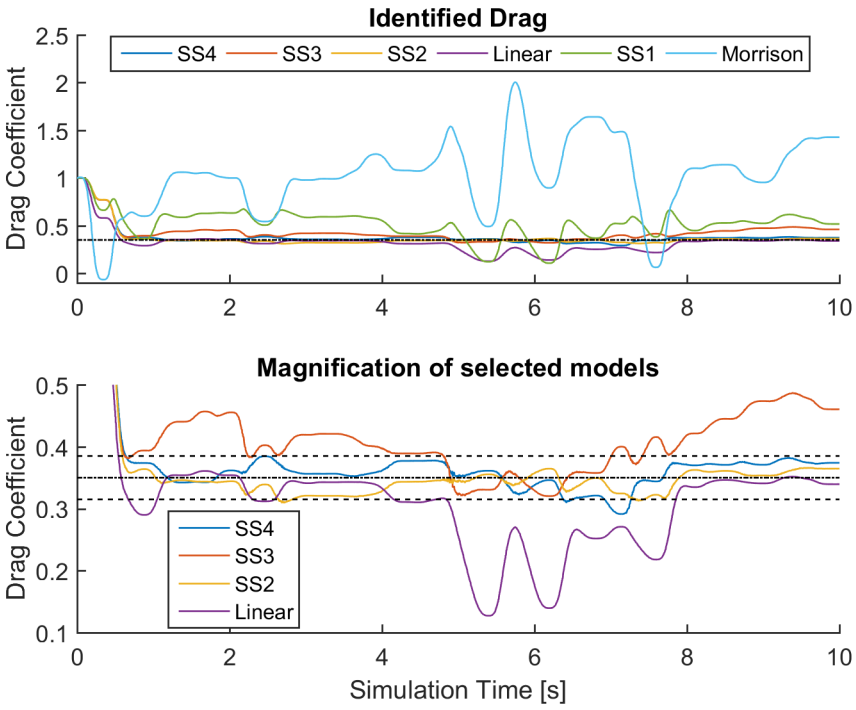

Figure 4.2: Time domain plot of the various models being used to identify the drag coefficient of the FPS. The center dotted line indicates the true value of 0.35 and the outer dotted lines represent a 10% error. SS followed by a number represents the order of the state space realization used in the potential time domain model.

shows six different identification runs trying to identify the true value of $C_D = 0.35$, a realistic but small drag coefficient used when modeling a surface piercing float [103]. Three of these runs are the models described in this paper: the linear lumped parameter model, the Morison model, and the potential time domain model. Additionally, three extra potential time domain models are included with first through third order realizations to evaluate the influence of various orders on identification. The numerical data that was used for identification was generated using a Bretshneider spectrum with a peak period of 2.69 seconds and a significant wave height of 0.3 meters. The model used to generate the numerical data used a tenth order state space realization which had a coefficient of determination of $R^2 = 0.9989$. This high order realization was chosen to reduce the error in the radiation force calculations and to ensure that none of the models used to identify the drag coefficient were the same as the model that was used to generate numerical data.

For this idealistic identification scenario it is clear that the Morison equation implementation is identifying a vastly different drag coefficient and there is a large amount of variability in the identified parameter. As this model starts with a fundamentally different form and relies significantly on the wave dynamics to produce forces acting on the object it follows that the drag be approximated using a different value. While the EKF is able to use the Morison equation to track the dynamics of the FPS it is unable to converge on a steady drag coefficient which is necessary for further use in this work. As a result the Morison equation does not appear to be a viable model for drag identification. The linear and state space approximations for radiation force appear to be much more capable of determining a static drag coefficient. Figure 4.2 shows that very low order realizations have the problematic tendency to produce a high variability in the identified drag coefficient. The minimum coefficient of determination of 0.99, associated with the fourth order state space model, appears to be satisfactory and is used in the rest of this work.

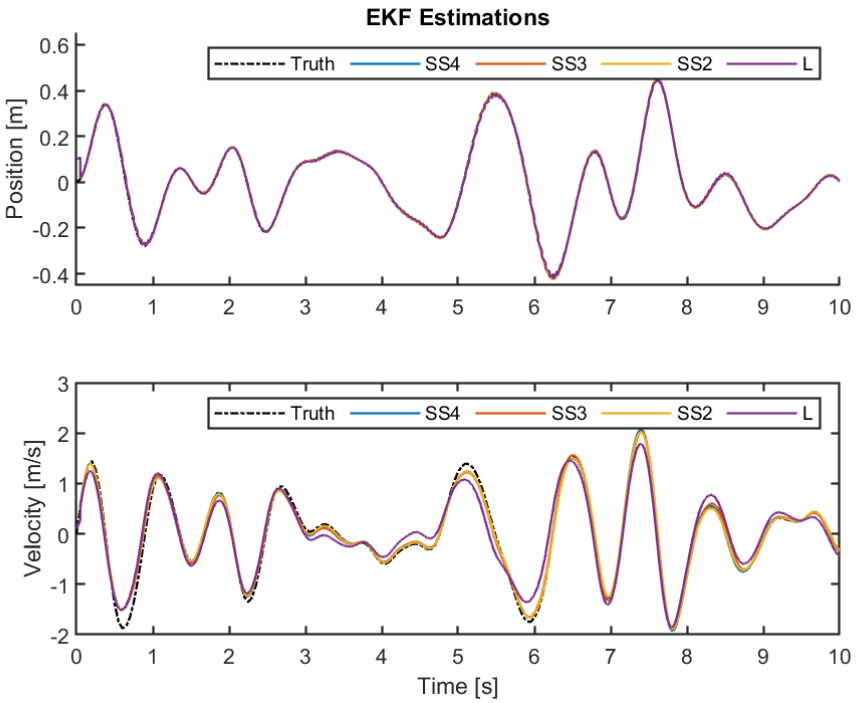

Figure 4.3: Time domain plots of each implemented model overlayed with the true state data. Since the position is the measured data the EKF is able to adhere very well to the first state, however the second state does not have sampled data influencing the algorithm so there is less accuracy in this state.

4.5.2 Identification with Limited Sampling

Using the extended Kalman filter to identify states in lab conditions with multiple observed states and a high sampling rate provides very favorable identification results. Another test case where only the position state is measured and the sampling rate is only 20 Hz is simulated which provides a more realistic example of the EKF identifying the drag coefficient. Figure 4.3 shows that even with a slower sampling rate the estimated position state and the true data match very well. However since the velocity state is not directly measured and incorporated into the EKF there is an apparent error between the estimated value and the true data. This estimation adheres to the form of the true data but it misses some of the abrupt changes and

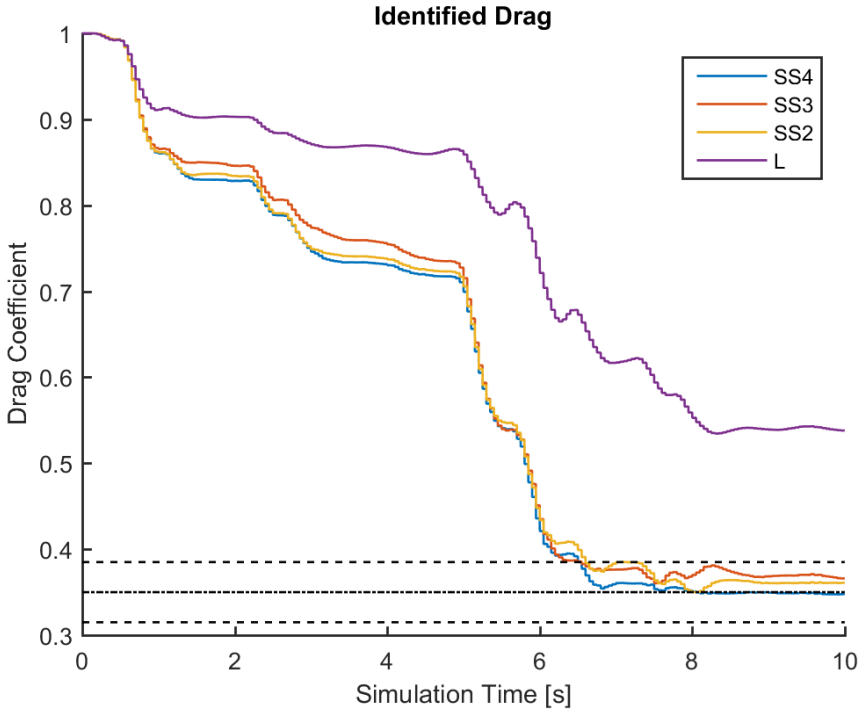

Figure 4.4: Time domain plot of the various models begin used to identify the drag coefficient of the FPS. The center dotted line indicates the true value of 0.35 and the outer dotted lines represent a 10% error.

peaks in amplitude. Without state estimation of the velocity kinematic relationships would be used to determine the velocity.

Figure 4.4 shows that while there is less sampled data the EKF is still able to identify a drag coefficient. With one state measurement removed the identification will respond slower as shown by the linear radiation force model not reaching the 10% error bounds on the true state in the allowed ten seconds of simulation time. However, the state space models that performed adequately with a large amount of sampled data show that they are capable of operating with very low sample rates while still providing usable state and drag coefficient information.

Since the process, or state, noise is never truly known for any model there is a wide

range of noise that will allow the EKF to work in a sub-optimal but effective manner. It is a necessary aspect of any Kalman filter to tune the noise to best identify or observe a given system [24]. For the work described in this paper a small study was done to test the resilience of the EKF to a range of added noises and tuning of the noise parameters. It was found that when simulating a WEC response in irregular waves the EKF is resilient to limited changes in the noise values. The process noise values were taken to be half of the original estimate and up to one and a half times their initial value with reasonable success for the fourth order state space radiation force model. For the linear radiation force model when the noise terms were halved the algorithm was unable to converge. As expected, varying the noise terms in the filter places a different amount of "trust" on each state which directly impacts how quickly the EKF is able to change the values of that state. For instance placing a very high noise covariance on the identified drag state will allow the EKF to vary that state quickly, potentially allowing the algorithm to identify a time varying drag.

4.5.3 Time Varying Drag

It is unlikely that any WEC will be a perfectly time invariant system, as such there will be variations in the drag coefficient as a result of wear, biofouling, water temperature, turbulence, and perhaps more. The EKF, since it is continually estimating the optimal state for a given set of numerical data, will treat the drag coefficient state as a time varying parameter. Figure 4.5 shows the EKF estimating the drag for three different time varying drag functions. Each estimation is performed with a sampling rate of 200 Hz and both position and velocity are measured states. The drag coefficient for the true data is determined by the function $C_D = 0.2sin(\frac{2*\pi}{T_{drag}}t) + 0.5$, where T_{drag} is the period of drag function and t is the time in seconds. This time varying function is meant to show that the EKF can adapt to a time varying drag that changes more rapidly than would be needed in a real situation. Figure 4.5 shows the response of the modified Cummins equation model with a fourth order state space radiation realization. In order to adapt to the quickly changing drag coefficient, the process noise covariance was increased drastically. As a result, all but the fourth order state

space potential time domain model experienced too much random variation to identify the drag coefficient. Even with a detailed model, estimation with a high covariance results in noticeable short term variation in the identified drag coefficient.

Figure 4.5 shows that if the drag is oscillating with roughly the same period as the wave then an effective identification is not possible. However, as the period of the time varying drag is increased to three or five times the period of the wave a reasonable estimation of the drag becomes possible. While there is an appreciable time delay with the identification of the time varying drag, the time delay begins to become insignificant as the period of the drag variation becomes large. The peak wave period of wave oscillation essentially corresponds to a lower limit of the timescale over which a variable drag can be identified. As the EKF would be continuously running on board a WEC the variation in drag coefficient is expected to account for the time varying effects described in this section.

4.6 Conclusion

This paper presents an implementation of a extended Kalman filter that observes a continuous model with discrete data for the purpose of state observation and drag coefficient identification of a heaving wave follower. Several lumped parameter models used in wave energy converter applications were used in the extended Kalman filter to provide insight into the tradeoff between simplicity and numerical accuracy. The most promising lumped parameter model is the potential based time domain model with a Morison drag term and a state space realization describing the radiation force as is traditional in the WEC modeling community. Two additionally simplified models are shown to be acceptable for state observation. However with excessively simplified models it becomes impossible to identify the Morison drag coefficient.

Since Kalman filters apply a "random walk" process to each state in the model the state space realization became unstable, causing the filter not to converge. To address this issue the covariance update equation in the extended Kalman filter was modified to ensure that the radiation states in the dynamics were not modified. This is reasonable because their process

noise is already described in the position and velocity states. The process noise covariance matrix is developed using the input-output relationship of the incident wave elevation and the body displacement and velocity.

Numerical data was generated using a model developed from a wave tank test of a floating power system meant for WEC deployments. The floating power system was used because it most closely represents the float component of a point absorbing WEC, working as a good test case for the identification and observation of future WECs. Numerical tests to determine if the extended Kalman filter can identify states with limited sampling are discussed, and a time varying drag coefficient is identified with the extended Kalman filter to show the robust nature of the algorithm. While computationally the slowest model tested, the fourth order state space system used in the potential time domain model proved to be the most reliable for the applications foreseen in this work.

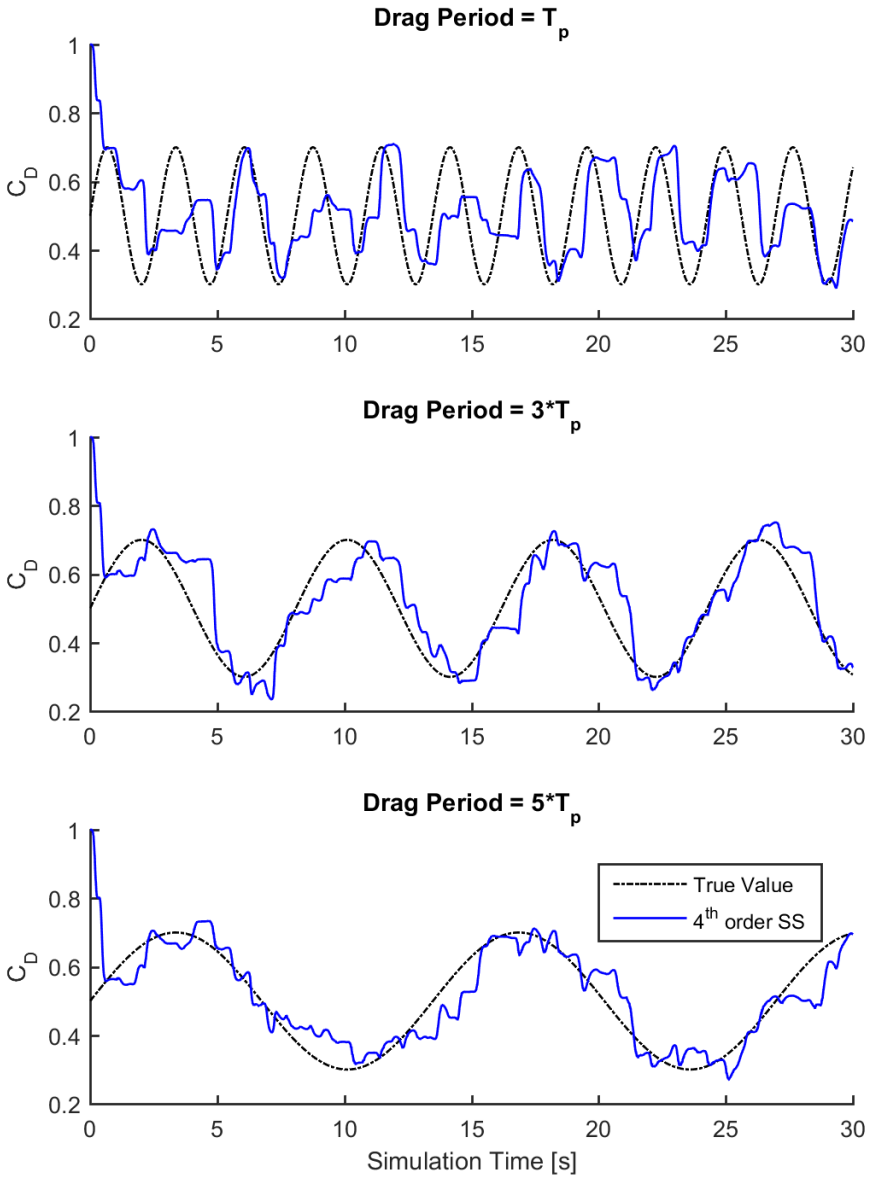

Figure 4.5: Time domain estimation of a time varying drag coefficient.Each subplot shows the estimation of a different drag function. $T_p = 2.69$ seconds

Chapter 5

WAVE EXCITATION FORCE ESTIMATION OF WAVE ENERGY FLOATS USING EXTENDED KALMAN FILTERS

The text of the following chapter was accepted for publication in the Journal of Ocean Engineering in 2020. With the exception of reformatting the text and the correction of typographical errors no changes were made to the content of the article as accepted. The citation for the paper, Ref. [31] is as follows:

Andrew F. Davis, and Brian C. Fabien. Wave excitation force estimation of wave energy floats using extended Kalman filters. *Journal of Ocean Engineering*, 198, 2020.

5.1 Introduction

Wave Energy Converters (WECs) are devices that generate electricity from ocean waves. Some non-exaustive reviews of the widely varying devices and modeling methods for WECs can be found in [33, 43, 63, 44]. This work will focus specifically on point absorbing wave energy converters. Point absorbing type WECs rely on a small body, when compared to the incident wavelength, to be actuated primarily in a single degree of freedom to achieve power generation.

Modern control strategies rely on state information to calculate an optimal control input. As addressed in [14] and [64], this is possible through the use of Kalman filters as optimal state observers. Kalman filters can also be used to estimate the wave excitation force which is necessary for many controllers [64, 78]. Even though Kalman filters are commonly used to estimate the states for control systems, the implementation of a Kalman filter on a WEC is not trivial. This work addresses some of the current barriers to state observation and excitation force estimation of wave energy converters using an Extended Kalman Filter (EKF),

which is the nonlinear adaptation of the Kalman filter.

The use of an EKF to determine wave excitation force using external pressure sensors is shown in [2]. However, the implementation of additional external pressure sensors may be impractical for many commercial WEC applications. Alternatively, [64] shows a way to use a Kalman filter to estimate the exitation force by modeling the excitation force as a disturbance in the WEC equations of motion. The disturbance used in [64] describes the excitation force as a sum of sinusoids as is typical in WEC modeling [44]. This method of estimating the wave excitation force will be referred to as the *disturbance estimation method*. Using a different approach, a linear Kalman filter is implemented in [78] where the excitation force is identified by including the force as a state with no dynamics and thereby allowing the "random walk" of the Kalman filter to identify the best estimate of the state directly. This methodology of implementing the Kalman filter to identify the wave excitation force will be referred to as the *direct estimation method*. The work of [78] also develops a receding horizon estimator which requires the solution of a dynamic programming problem at each time step. Estimation using the receding horizon method results in increased computational complexity but provides very little phase lag between the estimated and true excitation forces [78]. A similar disturbance model estimation method to [64] is [3], where a linear Kalman filter is used on simulation data to perform an investigation into excitation force estimation and prediction. The direct estimation method shown in [78] applies the same principle that is used for drag estimation in [30] and unknown parameter identification in [24]. The work of [40] provides an overview of control algorithms, many of which rely on the use of a linear Kalman filter. Excitation force prediction is of primary interest in the overview [40].

This work describes the implementation of an extended Kalman filter that uses a nonlinear continuous time model and discrete time measurements. The use of a nonlinear Kalman filter enables the inclusion of the nonlinear Morison drag term, that has become commonly included in many lumped parameter models and WEC modeling software packages [12, 23]. The implementation and sensitivity analysis of wave excitation force estimation with an extended Kalman filter on experimental data from [13] is described using both the direct

estimation and disturbance estimation methods. The considerations that need to be taken into account when implementing these two methods with a nonlinear model are given, and the sensitivity of the estimation methods to various conditions are investigated.

The work described in this paper is differentiated from previous literature in this field by providing the following contributions:

- The excitation force estimation is performed on experimental wave tank data.
- The implementation of a nonlinear extended Kalman filter made use of two different methods of adapting the Kalman filter to estimate the excitation force.
- The inclusion of an estimated velocity for the water surrounding the float allows for the nonlinear Morison drag term to be used in the model.
- The sensitivity of the estimation algorithm to measurement noise, wave climate, sampling rate, radiation realization, and the number of frequencies that are used to model the excitation force are studied.
- An equal energy approach is taken to choose the wave frequencies that comprise the disturbance model of the wave excitation force.

This work provides insight into the implementation of a nonlinear Kalman filter with experimental data for wave energy conversion. Reproducible methods are described to facilitate implementation of the EKF for excitation force estimation and an investigation of the limitations of the EKF is performed to help ensure the suitability of the application. The purpose of this work is to enhance the performance of state observers when estimating the wave excitation force acting on WECs with the goal of enabling more effective feedback control.

Advanced control strategies such as latching control or Model Predictive Control (MPC) offer increased power production when compared to traditional WEC control strategies [51,

14]. Optimal power absorption is achieved when the phase of the WEC velocity is properly aligned with the wave excitation force, to this end latching control uses an actuator to lock a WEC in a specific configuration long enough for the WEC to achieve the optimal phase with the excitation force [43]. Model predictive control is a method that solve a series of successive, small time horizon, optimal control problems [97]. The optimal control problem is solved for a future timespan and takes into account the current wave climate when determining the optimal control input. However, a short prediction of incident wave elevation or wave excitation force is necessary to implement this type of controller [47]. As the wave excitation force estimation is enhanced forecasting methods can be better implemented to provide the necessary time horizons for predictive and latching control methods.

Sections 5.2 and 5.3 describe the mathematical model and the experimental tests used in the development and implementation of the algorithms in this work, respectively. A description of the identification algorithms developed, and the excitation force estimation results along with sensitivity analyses, are given in sections 5.4 and 5.5. Finally, section 5.6 contains concluding remarks on the work presented.

5.2 Wave Energy Converter Model

The potential based time domain integro-differential equation analyzed in [8] has become the most prolific lumped parameter model for a WEC Equation of Motion (EOM). However, semi-emperical models or simplified lumped parameter models are also possible for WECs as shown in the detailed modeling description given in [30]. The equation of motion of a semi-submerged body in heave is given by

$$M_v \ddot{y} = F_B + F_D + F_R + F_M + F_{ex}. \tag{5.1}$$

where the inertial force of the object is the product of the "virtual mass", M_v, and the heave acceleration, $\ddot{y}$. This "virtual mass" is the sum of the mass of the body and the infinite frequency added mass of the entrained fluid, as is traditionally used in the Cummins formu-

lation [26]. The terms used in (5.1) are defined as: F_B is the hyrdostatic force on the object, F_D is the viscous drag force, F_R is the radiation damping, F_M is the restoring force from mooring lines, F_{ex} is the wave excitation force, and the displacement of the body is y. The dot notation represents derivatives with respect to time, for example, $\dot{y} = \frac{dy}{dt}$ and $\ddot{y} = \frac{d^2y}{dt^2}$. Discussion of the simplification of a general equation of motion to the form shown in (5.1) can be found in [30].

The potential flow based force terms of (5.1) are developed in agreement with the Cummins equation [26] which was originally developed to describe the motion of ships and is now applied to semi-submerged floating bodies. The work of [29] shows that the nonlinear viscous drag force is significant for wave followers and the work of [23] shows the necessity of the nonlinear visoucs drag for modeling software. As a result the viscous drag term will be included as a nonlinear term in (5.1). The viscous drag term is the lone nonlinear term in (5.1) as described in [8, 12] and the inertial, excitation, restoring, and radiation forces are assumed to be linear for the following development.

5.2.1 Mooring and Hydrostatic Forces F_M and F_B

The forces resulting from mooring and umbilical cables are modeled together as the product of a constant parameter and the body displacement as given by the linear relationship

$$F_M = -K_{mu}y, \tag{5.2}$$

where K_{mu} is lumped linear spring constant describing the forces acting on the body by the mooring lines and umbilical cable and y is the displacement from the static equilibrium point. By modeling the response of the body from the equilibrium position, as with the hydrostatic restoring force, only a linear relationship is needed to determine the vertical force contribution of the cables as a function of heave position. The constant can be determined experimentally using load cells and displacement measurements, described in section 5.3.

The hydrostatic restoring force is determined by

$$F_B = -\rho g A y, \tag{5.3}$$

where A is the projected area of the submerged volume at the calm water surface, ρ is the density, g is the gravitational acceleration constant, and y is the displacement from the static equilibrium. It is important to note that (5.3) assumes that a constant area is being submerged.

5.2.2 Drag Force F_D

The viscous drag is modeled using a quadratic Morison drag form [20, 103]. The drag in the heave direction is given by

$$F_D = -\frac{1}{2}\rho A_p C_D V|V| - b\dot{y}, \tag{5.4}$$

where V is the relative velocity between the object and the water particles surrounding it. The density of the fluid is given by ρ, and A_p is the projected area of the object in the heave direction. A signed velocity square term is computed by taking the product of velocity, V, and the absolute value of the velocity, $|V|$. Finally, the drag coefficient is given by C_D. The relative velocity, V, ensures that the drag force is not over predicted. If the velocity of the ocean wave was neglected then a large viscous drag force would be calculated any time the body is oscillating in phase with the incident wave, a case where the drag should be small since there would be very little motion between the body and the impinging water particles. An approach to estimating the vertical water velocity can be found in section 5.4.3. A discussion on the treatment of the viscous drag force as well as an identification method can be found in [30]. A small linear damping force $b\dot{y}$ is included to compensate for the fluid shear forces acting on the body and linear damping in the mooring lines. The coefficient b is based on the experimental response of the body at low velocities.

5.2.3 Radiation Force F_R

The force acting on the WEC that results from radiated waves is calculated in the time domain through the use of the convolution integral as illustrated in [26]. A state space realization of the convolution integral is created as an efficient method of computing the radiation force. The state space representation of the radiation force can be formed as

$$\dot{X}_r(t) = A_r X_r(t) + B_r \dot{y}(t), \tag{5.5}$$

$$F_R = - C_r X_r(t), \tag{5.6}$$

where X_r is the state variable of the realization. The state matrices A_r, B_r, and C_r, are a non-unique linear realization of the convolution integral and are generated from the impulse response function [57] of the system. A more detailed description of the Fourier transform inversion and computational considerations of describing the radiation force as a state space system is given in [30].

5.2.4 Excitation Force F_{ex}

The wave excitation force can be calculated using the excitation force Impulse Response Function (IRF), $F_{IRF}(t)$, and the wave surface elevation, y_w, using the convolution integral,

$$F_{ex}(t) = \int_{-\infty}^{\infty} F_{IRF}(\tau) y_w(t-\tau) d\tau. \tag{5.7}$$

This convolution is used to compute the true value of the excitation force for this work as shown in [64, 42]. The time range of the numerical integration is truncated to be longer than the active response of the excitation IRF which is determined by applying the inverse Fourier transform on the frequency dependant excitaiton force calculated from a BEM [42].

5.3 Available Data

Experimental data was made available by the Oregon State University Northwest National Marine Renewable Energy Center's Marine and Hydrokinetics Open Data Project [79]. The data set that is used in this work was a physical model test of a 1:10 scale floating power system at the COAST lab at Plymouth University [13]. The deep water tests described in [13] is used to determine the parameters in the equations of motion.

The mooring study described in [13] used a wave tank to compare several mooring configurations of two bodies in water. Of these two bodies, the scaled Floating Power System (FPS) is analyzed in this current work as it provides a very similar geometry to the float of a point absorbing WEC. The FPS is shown in Fig. 5.1 in the wave tank prior to wave generation. For this work a subset of experimental runs were chosen. Seventeen different panchromatic runs using an elastic "o-rings" as moorings are used to test the Kalman filter estimation algorithm in section 5.5. These moorings act as springs and allow for displacement in all six degrees of freedom. The work of [13] shows experimentally that a resonance period for the FPS exists between 2.5 and 2.8 seconds. Table 5.1 shows the significant wave height, H_s the peak period, T_p the zero crossing period, T_z and the bandwidth, B of the incident wave spectra. Each data set had roughly six-hundred seconds of data collected.

Incident wave elevation and mooring line forces were measured at 128Hz and motion data was recorded at a sampling frequency of 200Hz. Irregular waves were generated using the Bretshneider spectrum.

5.3.1 Reproducing Numerical Work

Detailed descriptions of the experiments along with wave tank schematics and dimensioned drawings can be found in the Marine and Hydrokinentics Open Data Project [79]. Key paramters used in the WEC models not found in [13] or [79] can be found in [30]. Frequency dependent terms, such as added mass, radiation damping, and wave excitation are calculated using the BEM code NEMOH [7]. Figure 5.2 shows the radiation damping and added mass as

Run No.	H_s mm	T_p [s]	T_z [s]	B [Hz]
1	175	1.42	0.338	0.13
2	50	1.90	0.391	0.17
3	175	1.90	0.391	0.17
4	300	1.90	0.391	0.17
5	50	2.37	0.436	0.21
6	175	2.37	0.436	0.21
7	300	2.37	0.436	0.21
8	50	2.69	0.465	0.24
9	175	2.69	0.465	0.24
10	300	2.69	0.465	0.24
11	50	3.16	0.504	0.29
12	175	3.16	0.504	0.29
13	175	3.95	0.563	0.36
14	175	4.74	0.617	0.43
15	175	5.53	0.666	0.50
16	375	2.06	0.407	0.19
17	375	2.37	0.436	0.21

Table 5.1: List of experimental runs from [13] that are considered in this work with corresponding significant wave height, H_s, peak period, T_p. Additionally the zero crossing period, T_z, and bandwidth, B are given for each generated wave spectrum.

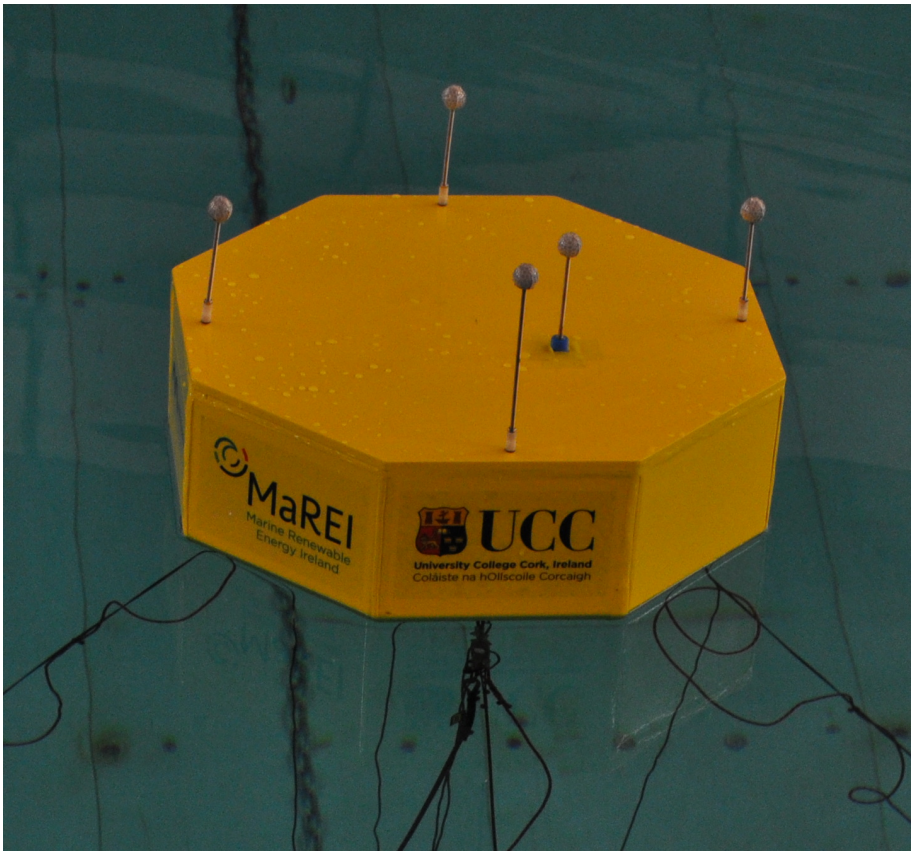

Figure 5.1: The 1:10 scale Floating Power System configured with elastic moorings and umbilical cable described in [13] and made available by the Northwest National Marine Renewable Energy Center's Marine and Hydrokinetics Open Data Project [79]. The FPS is 500mm wide (the characteristic length), 225mm tall, and has a mass of 9.58kg.

a function of angular frequency for the FPS. The magnitude and phase of the wave excitation force on the FPS is shown as a function of angular frequency in Fig. 5.3. The scripts used for this paper to execute NEMOH and all other figures will be made available on GitHub [28].

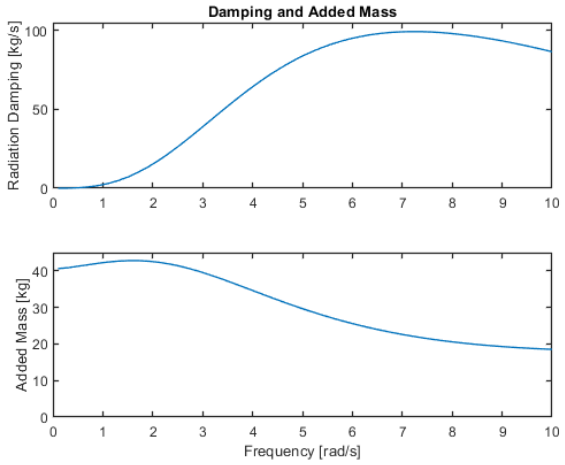

Figure 5.2: Radiation damping and added mass values are generated using NEMOH [7] for the range of frequencies that the FPS is excited by in [13].

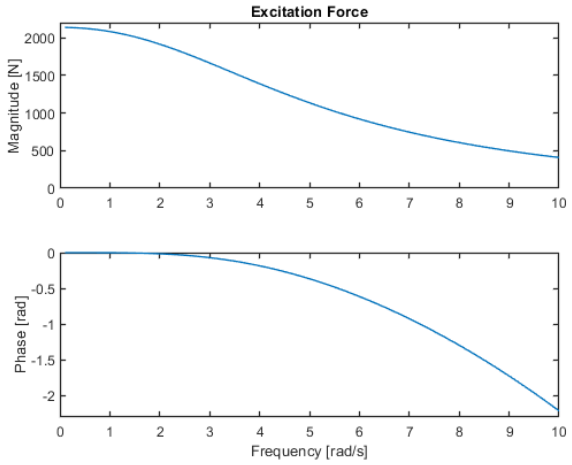

Figure 5.3: The magnitude and phase of the wave excitation force is calculated using NEMOH [7] for the range of frequencies that the FPS is excited by in [13].

5.4 Continuous-Discrete Extended Kalman Filter

The Kalman filter incorporates measured outputs, a model, and Gaussian error description to determine a statistically significant estimate of the state dynamics. A nonlinear continuous

time model with discrete time experimental data points can be observed using a continuous-discrete extended kalman filter. The EKF is a nonlinear adaptation of the Kalman filter which observes a dynamic system in which zero-mean Gaussian white noise is assumed in both the dynamics and measurement. The model that is observed by the extended Kalman filter is described by

$$\dot{x}(t) = f(x(t), u(t), t) + G(t)w(t) \tag{5.8}$$

$$\tilde{y}(t) = h(x(t), t) + v(t) \tag{5.9}$$

where f is the nonlinear state dynamics, h is the nonlinear output function, $G(t)$ is a vector that describes the noise of each state, $w(t)$ is zero-mean Gaussian white noise with a variance $Q(t)$, and $v(t)$ is zero-mean Gaussian white noise with a variance of $R(t)$. The tilde symbol, $\tilde{\bullet}$, modifying the output, y, represents that this is an experimentally measured quantity. The accuracy of the Kalman filter relies on knowledge of the process and measurement noise terms. Correct quantification of the process noise is essential for the EKF to function effectively. For discussions concerning the determination of the process noise covariance see [24, 72] and section 5.4.3. Since the EKF deals with nonlinear systems that must be integrated to determine state dynamics, reasonable initial conditions must be used to ensure filter stability [24].

The Kalman filter will iterate through the gain, update, and propagate steps for each discrete time in order to estimate the states of the system. The gain step calculates a matrix of gains that is used to correct a previous step's estimates based on the covariance of each state. The update step uses the calculated gain to adjust the covariance of each state and estimated value based on the difference between estimated and measured states. Finally the propagation step calculates the covariance and state estimates of the next time step.

Details on the theory of the continuous-discrete EKF can be found in [24] and the implementation of the algorithm on a WEC application can be found in [30]. For this implementation of the EKF the Joseph stabilized form of the covariance update equation is used, and

the symmetry of the covariance matrix is enforced by taking the element-wise average of the covariance and its transpose at each step. In order to use the Kalman filter for estimation the model must be modified to provide the estimated parameter as a function of the observed states as described below.

5.4.1 Direct Identification Estimation

To directly identify a force or parameter using the EKF the variable in question is appended as an extra state with no dynamics. Each state in the dynamics of a Kalman filter undergoes a "random walk" to determine the best estimate of the state variable at each time step [24]. The nonlinear dynamics in (5.8), described in section 5.2, when reduced to a first order system is,

$$\begin{bmatrix} \dot{x}_1 \\ \dot{x}_2 \\ \dot{x}_r \end{bmatrix} = \begin{bmatrix} x_2 \\ \frac{1}{M_v} F(x_1, x_2, F_{ex}, \dot{y}_w, C_r x_r) \\ A_r x_r + B_r x_2 \end{bmatrix} \tag{5.10}$$

where x_r is a vector of radiation states, x_1 and x_2 are the first order variables for position and velocity respectively, and both F_{ex} and $\dot{y}_w$ are inputs to the system representing wave excitation force and water velocity, respectively. The estimated wave excitation force can be used to provide a functional estimate of the water velocity surrounding the WEC as described in section 5.4.3.

The inclusion of F_{ex} as an estimated force necessitates the inclusion of another state in the dynamics as,

$$\begin{bmatrix} \dot{x}_1 \\ \dot{x}_2 \\ \dot{x}_3 \\ \dot{x}_r \end{bmatrix} = \begin{bmatrix} x_2 \\ \frac{1}{M_v} F(x_1, x_2, x_3, \dot{y}_w, C_r x_r) \\ 0 \\ A_r x_r + B_r x_2 \end{bmatrix} \tag{5.11}$$

where F_{ex} is now the third state of the system, x_3, estimated by the EKF. The inclusion of a state with zero dynamics means that the "random walk" that takes place during the gain and propegation steps of the Kalman filter is responsible for the changes in the estimated value. Equation (5.11) assumes that the time derivative of the excitation force has the form $\dot{F}_{ex} = gw(t)$, where g is a single term of $G(t)$ in (5.8) and $w(t)$ is a Gaussian zero-mean white noise signal. The EKF is then modeling the excitation force simply as noise where the current value of F_{ex} does not depend on previous estimates. The choice of the process noise $w(t)$ for the estimated force is crucial to success of the estimation algorithm, the selection of noise is discussed in [24] and the choice used in this work is described in section 5.4.3.

The direct identification method only adds a single state to the dynamics of the system and as such is the most computationally simple identification method used in this work. An additional initial condition is necessary with the addition of any state is required, however precise determination of this initial condition is not necessary as it is expected that there be an initial error in the dynamics. This method of identifying the excitation force does not require information on the wave climate, however a sensitivity analysis of the process noise corresponding to the identified state should be performed. An example where a large process noise for an identified state is able to identify a time-varying viscous drag coefficient is shown in [30].

5.4.2 Disturbance Model Estimation

An alternative method of estimating the wave excitation force is to model the incident wave force as a disturbance to the WEC dynamics [65]. Ocean waves and excitation forces are typically modeled as a harmonic oscillator, or the sum of a large number of sinusoids, with parameters determined by a wave energy spectrum and randomized phase [44]. The disturbance, as described by [64], will be modeled using a similar approach. The regular

wave representation of the excitation force is given as

$$F_{ex} = \mathbb{R}\left[\frac{H}{2}F_X(\omega)e^{i(\omega t)}\right], \tag{5.12}$$

where $\mathbb{R}$ represents the function to extract the real part of the argument, H is the peak to peak wave height, and $F_X(\omega)$ is the magnitude of the frequency domain excitation force for a given frequency, ω. The imaginary unit is donated by i, and t is the time in seconds. This excitation force can be extended to irregular waves by

$$F_{ex} = \mathbb{R}\left[\int_0^\infty \sqrt{2\Delta\omega S(\omega)}F_X(\omega)e^{i(\omega t+\phi(\omega))}d\omega\right], \tag{5.13}$$

where $S(\omega)$ is the power of the wave spectrum as a function of frequency. The variable $\Delta\omega$ is the discrete frequency separating each frequency, ω, and ϕ is a vector of randomly generated phase angles in radians [52].

Equation (5.13) shows an infinite integral over a range of frequencies which is typically modeled as a discrete sum [44]. By looking at a single frequency component of the wave excitation force a description of the excitation force dynamics can be shown as,

$$\begin{aligned} f_{ex} &= sin(\omega t) \\ \ddot{f}_{ex} &= -\omega^2 sin(\omega t). \end{aligned} \tag{5.14}$$

The differential equation describing the excitation force can be implemented in the first order system of equations by

$$\begin{bmatrix} \dot{x}_1 \\ \dot{x}_2 \\ \dot{f}_{ex} \\ \ddot{f}_{ex} \\ \dot{x}_r \end{bmatrix} = \begin{bmatrix} x_2 \\ \frac{1}{M_v}F(x_1, x_2, f_{ex}, \dot{y}_w, C_r x_r) \\ \dot{f}_{ex} \\ -\omega^2 f_{ex} \\ A_r x_r + B_r x_2 \end{bmatrix}, \tag{5.15}$$

where f_{ex} and $\dot{f}_{ex}$ are now states of the dynamic system. The above expression describes a system where a single excitation force signal is estimated, similar to the direct identification method. However, (5.15) enforces that the estimated excitation force be a solution to the differential equation given in (5.14).

This excitation force estimation method can be generalized to use multiple wave frequencies by using

$$\begin{bmatrix} \dot{x}_1 \\ \dot{x}_2 \\ \dot{f}_{ex} \\ \ddot{f}_{ex} \\ \dot{x}_r \end{bmatrix} = \begin{bmatrix} x_2 \\ \frac{1}{M_v} F(x_1, x_2, \Sigma \bar{f}_{ex}, \dot{y}_w, C_r x_r) \\ I \dot{\bar{f}}_{ex} \\ -\Omega^2 \bar{f}_{ex} \\ A_r x_r + B_r x_2 \end{bmatrix} \tag{5.16}$$

for the dynamics. The bar over the excitation force denotes a vector of disturbance forces. The excitation force becomes $F_{ex} = \Sigma \bar{f}_{ex}$ to denote the sum of N excitation force terms that each oscillate at a different frequency and I is the $N \times N$ identity matrix. The term Ω denotes the diagonal matrix containing each of the N frequencies corresponding to the entries of $\bar{f}_{ex}$. The sum of each excitation force frequency allows for the excitation force to be modeled in a way that realistically describes the time derivative behavior of the wave excitation force. This method however requires knowledge of the wave climate for an appropriate choice of the disturbance wave frequencies. The choice of these frequencies is discussed in section 5.4.2. The initial conditions of the excitation terms should satisfy the differential equations given by (5.14). These initial conditions act as the terms that dictate the phase of the excitation force terms.

Just as with the direct identification method, each of the new states that are included in the dynamics are subject to a "random walk" that is influenced by the process noise covariance in the gain and propagation steps of the Kalman filter. The disturbance estimation method becomes nonlinear if any of the frequencies in Ω are varied, where any frequencies

would then be appended to the dynamics as an extra state [64]. For this work the frequencies remain constant.

The disturbance model introduces two states for every disturbance frequency that is used in the dynamics which is a significant increase in computational complexity over the direct identification method. However, the use of the equal energy approach when selecting wave frequencies provides an effective way to model the incident wave with only a few frequencies. This enables the use of the disturbance model to more realistically describes the wave excitation force.

Equal Energy Approach

The implementation of the disturbance method requires the choice of N frequencies to comprise the wave excitation force. The typical approach to representing irregular waves uses many frequencies, on the order of 10,000 sinusoids [78], however this number would be computationally impractical for implementation in a Kalman filter. Unlike the typical time domain construction of waves the disturbance method makes use of variable magnitudes of the frequency components which are states in the model. This means that fewer frequencies are required to adequately describe the time domain wave excitation force. The wave frequencies used to construct an irregular wave can be found in several ways as described in [67]. Some examples include an arithmetic progression, which selects wave components that are equally spaced in frequency, and a geometric progression, which selects wave components that have a constant ratio of wave frequency. Both of these methods typically require large numbers of waves to realistically represent an irregular wave. In contrast, the equal energy method can be used to realistically represent an irregular wave with relatively few frequency components, and is mentioned in [44]. The basic premise of this method is to select wave components such that each frequency represents an equal amount of spectral energy. Since this energy is calculated by considering the area under the energy spectrum, this method is sometimes referred to as the equal area approach.

Figure 5.4 shows the wave energy spectra of the 17th run of the experimental data de-

scribed in section 5.3. The significant wave height of the generated wave was 375 mm and the peak period was 2.37 seconds. The vertical blue lines show the divisions between each equal energy area of the spectra and the red circles indicate the power and frequency of the components that were selected to form the disturbance equations.

The divisions are created by determining the area under the energy spectra and dividing this by the number of desired frequency components, which was in this case 5 components, to determine the area of each division. A threshold for minimum power is required otherwise the very high and very low frequency components would artificially bias the selection towards frequencies with very little energy. Once the equal energy areas are determined a single frequency with the average power is selected from each equal energy area to provide the average power for that division. This method of determining the disturbance frequencies is effective for selecting wave frequencies and initial estimations of each components magnitude while only requiring the peak period and significant wave height of the incident wave spectra.

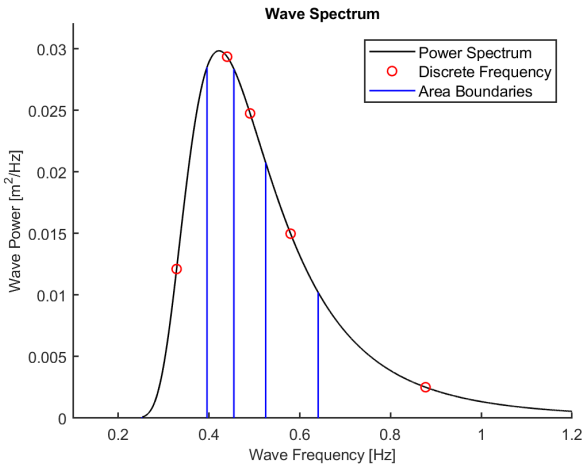

Figure 5.4: The wave spectrum of run 17 generated by the Bretschneider Spectrum. Red circles indicate the frequencies selected for use in the disturbance method and blue lines are the divisions between the equal energy areas of the spectra.

5.4.3 Implementing the EKF

In order to implement the extended Kalman filter a few key considerations were required prior to successful estimation of the excitation force. First, and often the most difficult part of any Kalman filter, is determining the process noise covariance given below. The other barrier to the implementation of the nonlinear equation of motion is that in typical WEC models both the excitation force and incident water velocity are unknown, therefore an approximation of the wave velocity is required. The method used in this work for estimating the water velocity is described below.

Process Noise

The process noise covariance is the product of $G(t)w(t)$ that describes the error in the dynamics of the system. The diagonal entries of the symmetrical matrix $G(t)w(t)$ are variances of the noise in each state and non diagonal entries quantify the correlation between the states. A typical assumption for the development of a Kalman filter is to assume that no cross-correlation exists between states [24]. For the equation of motion the radiation states are excepted from having a process noise variance as the error in the radiation force is included in the error for the position and velocity states [30].

The process noise for each state was found by simulating the response of the model to the inputs determined from experimental measurements. As with the work of [64, 12, 52], the convolution formulation of the excitation force in (5.7) is used to determine the wave excitation force that the float experienced during each experimental run, and the water particle velocity is known from measurements of the incident wave described in section 5.3. The dynamics of the float are simulated using the experimental measurements and the states are compared to the measured states from [13]. The process noise describes the error between the simulated states and the experimental states, so the variance of this simulation error is calculated for each run and used as the process noise covariance in the EKF. This method of estimating the process noise relies on the assumption that any full scale deployed WEC

will be preceded by model tests.

Recall that we are considering various experiemental runs from [13], and attempting to determine the wave excitation force for each run. Since the process noise is a variable, with dimensions, that will vary based on the incident wave it becomes necessary for each run to have its own process noise. A typical Kalman filter implementation requires a significant amount of tuning to provide effective estimation [24] and in some cases optimization algorithms are used to identify a "best" choice of the process noise terms [65]. For this work, a reasonable value of process noise for the excitation force was chosen for each separate sensitivity analysis as changes in sampling rate, model complexity, and measurement noise all change the robustness of the EKF to changes in the estimated state process noise.

Estimating Water Velocity

The estimation of the water velocity of the incident wave enables the calculation of the Morison drag force as the relative velocity is needed between the body and the surrounding water particles. With this estimation of the velocity it becomes possible to observe the model described in section 5.2 using an EKF. It is important to note that this nonlinear time domain model is well represented as a generic model for point absorbing WECs [12].

The estimation of the water particle velocity relies on a regular wave representation of the wave excitation force using (5.12). When simulating the excitation forces in irregular waves using (5.7) it is necessary to incorporate the time delay and the frequency dependent magnitude of the excitation force, however in order to approximate the incident wave elevation the wave excitation force is assumed to have a small phase lag and a magnitude equal to the magnitude of $F_X(\omega_p)$, where ω_p is the peak frequency of the exciting wave. Figure 5.3 shows a small wave excitation force phase lag for the frequencies corresponding to the irregular waves used in this work given in Table 5.1.

By using the linear relationship of (5.12) between the wave elevation and excitation force,

the wave elevation can be approximated by

$$y(t) = \frac{F_{ex}(t)}{||F_X(\omega_p)||_2} \tag{5.17}$$

where $F_{ex}(t)$ is the estimated excitation force and $||F_X(\omega_p)||_2$ is the L2-norm, Euclidean norm, of the excitation force at the peak frequency of the incident wave. This norm is required as each entry of $F_X(\omega)$ is an imaginary number that is used to represent the magnitude and phase of the wave excitation force. Note that (5.17) should only be used to calculate the wave height based on the heave forces acting on a body with a small characteristic dimension relative to the wave length. The wave velocity can then be computed using a finite difference method based on the previous estimations of the water elevation. This simple method allows for the full implementation of the Morison drag equation with the time domain model discussed in section 5.2. The estimation results of the water particle velocity are given in section 5.5.

5.5 Estimation Results

The two estimation methods presented in this work were tested using the experimental data described in section 5.3. The discrete measurements used in the EKF are the heave position and velocity, and the estimated excitation force is compared to the excitation force calculated using the non-causal convolution integral formulation in (5.7). This convolution integral relies on knowledge of the time history of the incident wave as well as the impulse response of the buoy in the heave direction, both of which are known before estimation as a result of the work in [13]. The experimental values of water velocity is determined by taking the time derivative of the measured water surface elevation. This data was recorded at the side wall of the wave tank, which is the undisturbed water surface elevation that is incident to the FPS.

Each estimation run is evaluated using a Goodness Of Fit (GOF), computed by using

the Normalized Mean Square Error (NMSE), given by the expression

$$GOF = 1 - NMSE = 1 - \frac{||s(t) - \tilde{s}(t)||_2}{||s(t) - \bar{s}(t)||_2}, \tag{5.18}$$

where $s(t)$ is the time domain reference signal, the bar notation denotes the mean value, $\tilde{s}(t)$ is the estimated signal, and the notation $||\bullet||_2$ represents the L2-norm of a vector. In this work the value will be represented as a scalar, less than or equal to one, where $GOF = 1$ would denote perfect estimation of the reference signal [69]. Alternatively the goodness of fit can be represented as a percentage as shown in [78]. In the case of this work both the incident wave velocity and excitation force are evaluated using (5.18).

Figure 5.5 shows the time domain estimation of the wave excitation force using both the direct identification method and the third order disturbance estimation method, where *third order* signifies that the disturbance models is a sum of three excitation force frequencies, for the incident wave. The reference signal that was calculated from experimental measurements is shown in black, and the results from the direct identification and the disturbance estimation methods are shown in blue and red, respectively. The third order disturbance estimation is shown as it provides a representative example of the performance of the disturbance estimation method while also being directly comparable to the work of [64]. This figure shows that some of the very sharp changes in the excitation force are not captured by the estimation algorithm, however it is apparent that the estimation algorithm results in a excitation force signal that represents the reference signal. For this estimation run the significant wave height of the incident wave was $H_s = 300$ mm and the peak period was $T_p = 2.37$ s. The GOF of direct and disturbance estimations are 0.914 and 0.927, respectively. In order to test the estimation algorithms in a variety of wave climates the excitation force estimation was performed for the seventeen different wave climates described in section 5.3, the results of which are shown in Fig. 5.7.

The estimation of the incident wave water velocity is shown in Fig 5.6 for the run 8 in table 5.1. The water velocity results from the direct estimation implementation and the

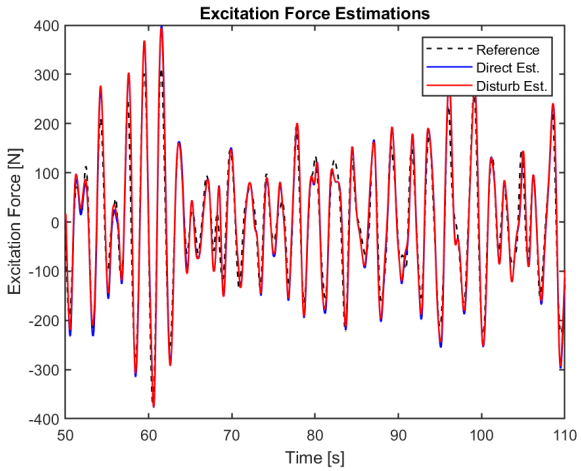

Figure 5.5: Time domain plot of estimated excitation force for a sixty second window using run number 7. The reference signal is generated using (5.7).

disturbance estimation implementation are once again shown in blue and red, respectively. The method by which the incident water velocity is estimated is described in section 5.4.3. It is not difficult to tell by visual inspection that estimation of the water velocity is not as accurate as the estimation of the excitation force. This is reflected in the goodness of fit values, which for the direct and disturbance estimation methods results, shown in Fig. 5.6, are 0.825 and 0.831, respectively. The approximation used to describe the velocity as a function of excitation force is very simplistic and a more detailed formulation of water velocity as a function of excitation force using the relationship given by (5.13) could be implemented. Additionally, a higher order finite difference scheme could be implemented. However, as the influence of the water velocity on dissipation forces does not drive the dynamics of the WEC, this simple approximation method is sufficient for this work.

The GOF of several estimation algorithms applied to each run in table 5.1 are shown in Fig. 5.7. Recall that both of the estimation methods being presented are run seventeen times, once for each of the different wave climates being considered. The results are shown in Fig. 5.7 as box and whisker plots to give an understanding of the overall performance

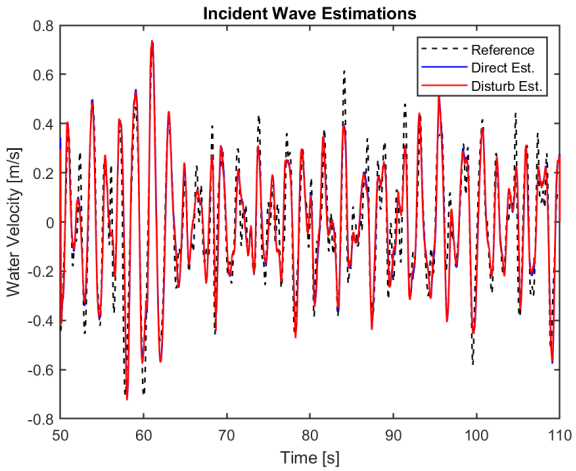

Figure 5.6: Time domain plot of estimated water velocity for a sixty second window using run number 7. The reference signal is generated by taking the time derivative of the incident wave.

of each method. For this comparison the direct estimation method is shown compared to the disturbance estimation method of varying orders (one excitation term to five excitation terms). It can be seen from the figure that the performance of the disturbance estimation algorithm provides the best estimation result using three excitation force components. As a result the third order disturbance estimation method will be used when analyzing the sensitivity of the estimation algorithms. The estimation of the incident wave velocity is shown in Fig. 5.8. As shown in Fig. 5.8 the mean GOF value tends to be roughly 10% lower than the excitation force estimation shown in Fig. 5.7.

Both figures 5.7 and 5.8 show a single outlier marked with a red +. This outlier corresponds to the first run in table 5.1. This high frequency wave is shown to be consistently difficult for the EKF to estimate. While it is possible to tune the parameters of the Kalman filter to better estimate the high frequency wave that is currently being shown as an outlier, the purpose of this work is to show general trends in the estimation capabilities of the EKF methods. Therefore, rather than producing the highest possible goodness of fit for a single

wave climate this work focuses on tuning the parameters of the Kalman filter to produce acceptable estimation for a wide range of wave climates. It is of interest to note that this first run consisted of a wave that generated relatively small excitation forces when compared to the waves from the other runs being considered. For example, the excitation force of the seventeenth run has a magnitude about four times larger than the first run. This means that the wave from the first run will have a much smaller effect on the dynamics of the buoy than any of the other runs considered in this work. Therefore, while this first run consistently has the lowest GOF of any of the runs being considered, the waves that are consistently estimated well by the EKF have a much larger effect on the buoy dynamics.

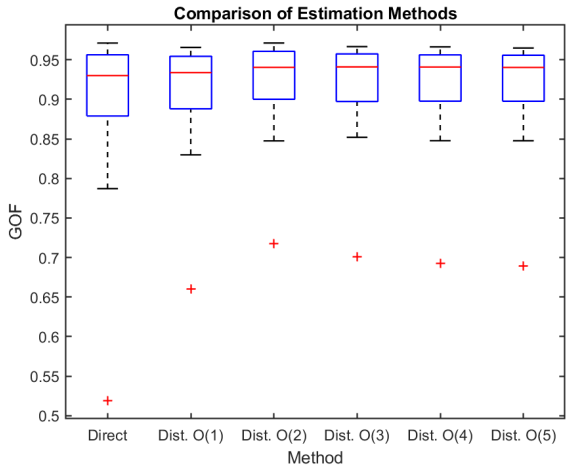

Figure 5.7: The comparison the direct estimation method and five variations of the disturbance method for wave excitation force. O(*) refers to the number of sinusoids used in the disturbance method. Outliers are denoted with a red +.

As each run represents a different incident wave the GOF can be plotted as a function of significant wave height, shown in Fig. 5.9, and size ratio, shown in Fig. 5.10. The size ratio is defined as the ratio of characteristic width of the FPS and the wavelength of a deep water wave with the peak frequency of the irregular wave.

In Fig. 5.9 the GOF is shown to not be directly influenced by the significant wave height,

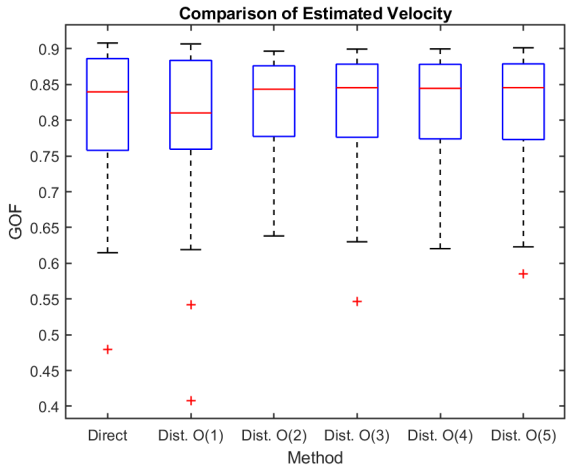

Figure 5.8: The comparison the direct estimation method and five variations of the disturbance method for wave velocity. O(*) refers to the number of sinusoids used in the disturbance method. Outliers are denoted with a red +.

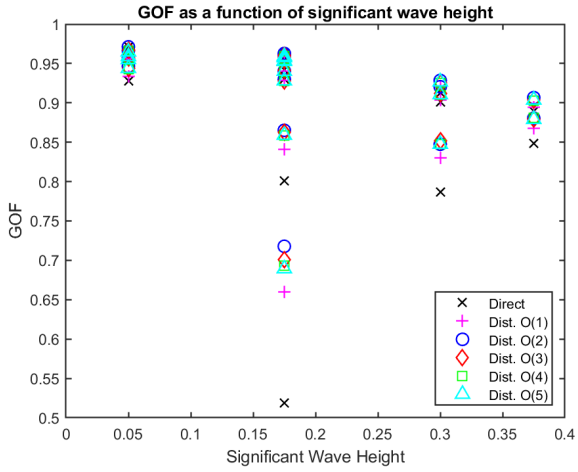

Figure 5.9: The excitation force estimation goodness of fit of each run as a function of the peak period of the significant wave height, H_s. O(*) refers to the number of sinusoids used in the disturbance method.

unlike the wave frequency and size ratio. The performance of the estimation algorithms tend to be worse in the cases where the wave is oscillating at a high frequency. Figure 5.10 shows

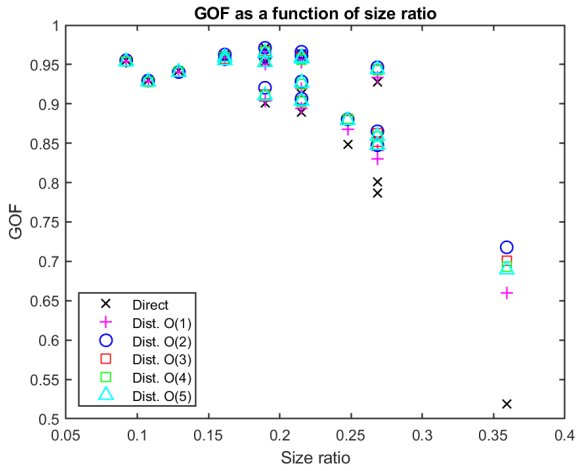

Figure 5.10: The excitation force estimation goodness of fit of each run as a function of the dimensionless ratio between the characteristic dimension of the float and wavelength. O(*) refers to the number of sinusoids used in the disturbance method.

that the lowest performing estimation runs occur at low frequencies, since the frequency of deep water waves can be directly related to wavelength. The size ratio is commonly used to determine the dominant forces for modeling purposes [77]. As the relative size of the float when compared to the wavelength becomes large the assumptions used in the development of the EOM for this work may be called into question as the size ratio is shown to negatively impact the GOF of each run in Fig. 5.10.

5.5.1 Sensitivity to Sampling Rate

The motion data is originally recorded at a sampling frequency of 200Hz. A subset of the motion data is used to test the sensitivity of the estimation algorithms to sampling rate. Figures 5.11 and 5.12 show the response of the direct estimation and third order disturbance estimation when the sampling rate is lowered. To select a subset of the measurements an evenly spaced number of the measurements were selected and treated as the measured data points. The resulting sampling frequencies are used as the control variable to determine the

influence on the GOF of the estimations.

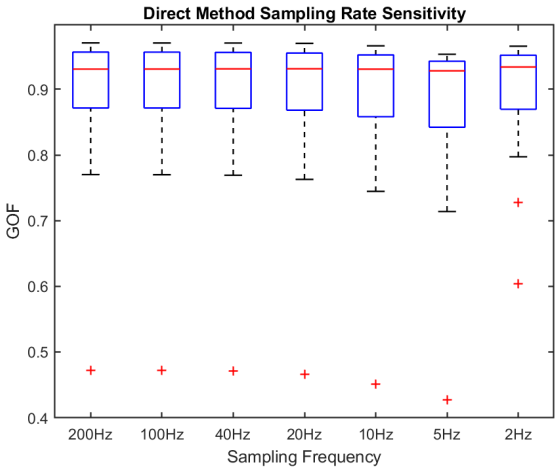

Figure 5.11: The excitation force estimation GOF using the direct estimation method of each run shown for various sampling frequencies. Outliers are denoted with a red +.

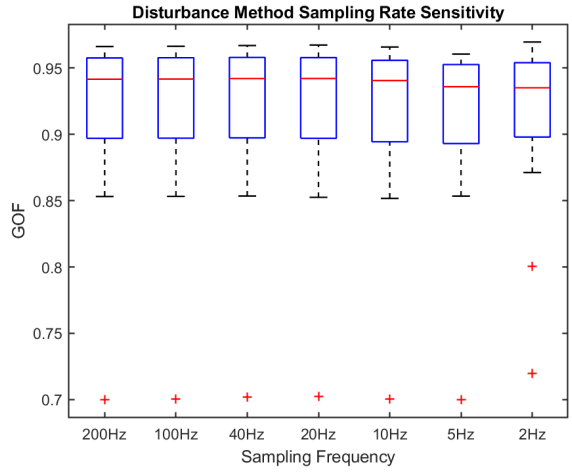

Figure 5.12: The excitation force estimation GOF using the third order disturbance estimation method of each run shown for various sampling frequencies. Outliers are denoted with a red +.

Figures 5.11 and 5.12 show that even at much lower sampling rates the effectiveness

of the EKF to identify the excitation force still results in a GOF greater than 0.9. The outlier corresponding to the first, high frequency, run shows a more significant performance degradation than the mean performance of the rest of the runs. It intuitively follows that a low sampling rate would adversely affect the estimation of a high frequency wave. It is important to note that while the average for the runs appears to increase at a sample rate of 2Hz the fact that an extra outlier is shown means that the overall performance for all of the runs is lower. This extra outlier in both Figs. 5.11 and 5.12 corresponds to run 4 which has a low period for its amplitude. The robustness of the estimation algorithms to a change in sampling rate shows promise for the potential of real time estimation for WEC deployments.

5.5.2 Sensitivity to Radiation Force Order

The radiation force is modeled using a state space realization given by (5.6) that can vary in size. Reference [65] shows a study in which the order of the radiation realization is varied and the effect on the estimator performance is evaluated using simulated wave measurements. When generating the state space realization of the radiation force it is typical to use a coefficient of determination as shown in [30]. The fourth order state space realization, used in this work, was the smallest realization that satisfied the minimum coefficient of determination threshold established in [30]. A simple investigation into the effects that the order of the radiation force has on the excitation force estimation is described below. The coefficient of determiniation of each of the state space realizations is given in Table 5.2.

It is shown in both Figs. 5.13 and 5.14 that using a first order realization for the radiation results in a significant decrease in performance. Note that for the second through fifth order realizations the performance of the estimator remains fairly constant. However, as mentioned above, it was shown in [30] that the fourth order radiation force is the smallest realization that is viable for identifying a missing drag force for this heaving float. As a result, the fourth order radiation force is used throughout the rest of the simulations in this work.

Realization Order	GOF
1	0.622
2	0.973
3	0.968
4	0.987
5	0.987

Table 5.2: List of state space model orders with coefficient of determination. Equation (5.18) is used to compute the coefficient of determination comparing the impulse response function from the boundary element method and the state space realizations.

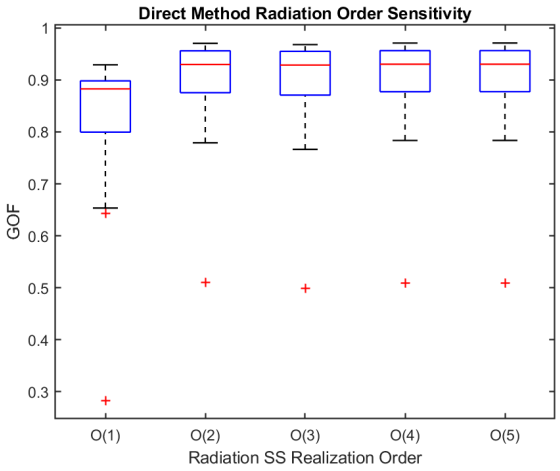

Figure 5.13: The excitation force estimation GOF using the direct estimation method of each run shown for various orders of the state space radiation realization. O(*) refers to the order of the state space realization of the radiation force. Outliers are denoted with a red +.

5.5.3 Sensitivity to Measurement Noise

The experiments described in [13] obtained high quality position measurements by using a Qualysis data acquisition system. The measurement noise used in the EKFs is very small, calculated from the residuals of the position measurements. The standard deviation of the measurement noise for position and velocity was $v = 6.075 \times 10^{-4}$. To investigate the sensitivity of the estimation algorithms to measurement noise an artificial, zero mean, Gaussian

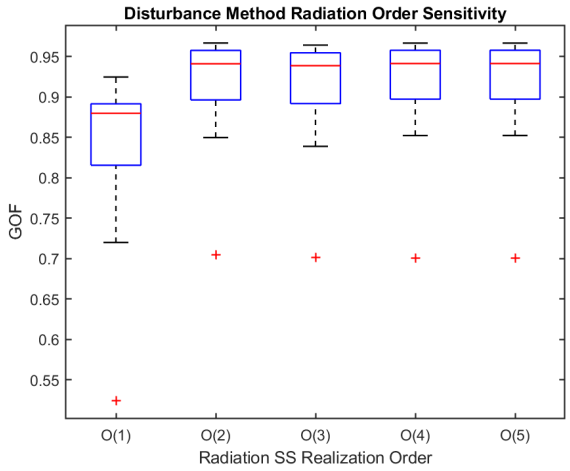

Figure 5.14: The excitation force estimation GOF using the disturbance estimation method of each run shown for various orders of the state space radiation realization. O(*) refers to the order of the state space realization of the radiation force. Outliers are denoted with a red +.

noise term was added to the measurements. Figures 5.15 and 5.16 show the GOF for the direct estimation and disturbance estimation methods, respectively, as artificial measurement noise is added to the experimental measurements. The actual measurement noise is very small, the artificial measurement noise, v_a is described by a noise factor that is an integer multiple of the experimental measurement noise. Both Figs. 5.15 and 5.16 show the resilience of the EKF, as no appreciable performance degradation is shown until the artificial noise is several orders of magnitude larger than the measurement noise.

5.6 Conclusion

This paper presents the implementation of an Extended Kalman Filter (EKF) to estimate the wave excitation force of a Wave Energy Converter (WEC). Many advanced control strategies require the wave excitation force that is acting on the WEC to determine the control input. However, real time measurement of the wave excitation force is typically not viable for ocean deployments. To provide information about the wave excitation force, Kalman filters are

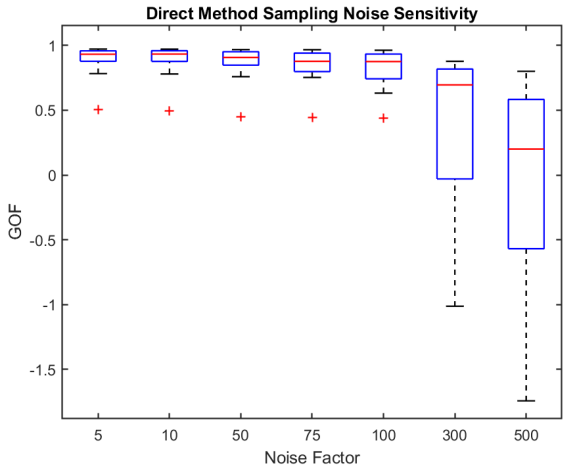

Figure 5.15: The excitation force estimation GOF using the direct estimation method of each run shown for various added measurement noises. Outliers are denoted with a red +.

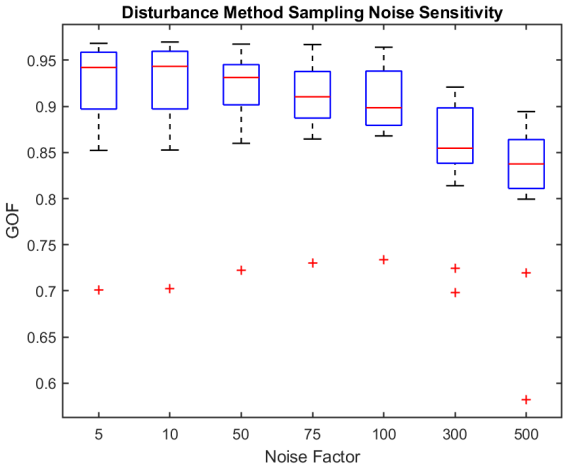

Figure 5.16: The excitation force estimation GOF using the disturbance estimation method of each run shown for various added measurement noises. Outliers are denoted with a red +.

implemented as optimal state observers which are configured to estimate the wave excitation force along with the dynamics of the WEC. Prior to this work, typical implementations of

the Kalman filter have been restricted to linear Kalman filters and have been tested with simulations rather than experimental data.

Two different estimation methods, making use of the nonlinear Kalman filter, are described in this work, both of which are tested with experimental data from a 1:10 scale wave tank test of a floating power system which closely resembles a point absorbing float. The *direct estimation method* relies on modeling the excitation force as a single state with no dynamics, allowing for the "random walk" of the Kalman filter to determine a statistically significant estimate of the excitation force. The *disturbance estimation method* models the wave excitation force as a sum of sine waves with the appropriate derivatives modeled as states. An equal energy method is used to determine the amplitudes and frequencies of the harmonic components. The quantity of the harmonic excitation terms is varied and discussed in this work.

The potential based time domain integro-differential equation of motion, used in this work, is a widely applied lumped parameter model for WEC bodies. This model includes a Morison drag term which is nonlinear and requires knowledge of the incident wave velocity to describe the drag acting on the object. The nonlinearity of this model requires the use of the EKF rather than the simpler linear Kalman filter. Much like the wave excitation force, the incident wave velocity is typically unknown in WEC deployments. A simple approximation of the incident wave velocity is developed and tested in this work, which enables the full implementation of the nonlinear equation of motion. The error between the estimated excitation force and true excitation force is evaluated using the normalized mean square error for seventeen different wave climates. The sensitivity of the excitation force estimation error is evaluated for variation in the model of radiation force, measurement noise, sampling rate as well as wave climate.

Both of the estimation methods discussed in this work were shown to provide good estimates of the excitation force using experimental data that would be available during a WEC deployment. The harmonic oscillator model of the wave excitation force utilized in the disturbance estimation method is a more realistic model of the force, which results in some

improvements in estimation accuracy. The excitation force estimation of both methods is shown to be quite resilient to a wide range of situations. This work shows that a common, nonlinear, lumped parameter model, previously unused for wave excitation force estimation, can be used to accurately estimate experimental excitation forces through the use of an extended Kalman filter.

Chapter 6

WAVE EXCITATION FORCE PREDICTION OF A HEAVING WAVE ENERGY CONVERTER

The following chapter has been recommended for publication in the IEEE Journal of Oceanic Engineering. In accordance with conventions familiar to IEEE reviewers the variable z is used for heave displacement. This variable change allows the variable y to be used as the output of the autoregressive models which is consistent with literature on the subject. With the exception of reformatting the text and the correction of typographical errors no changes were made to the content of the article as submitted.

6.1 Introduction

Wave Energy Converters (WECs) are being developed to provide a renewable source of energy to coastal communities in response to rising global energy demands [43]. Reviews of the widely varying devices and modeling methods for WECs can be found in [43, 33, 63, 44] and an example of an operating wave farm can be found in [54]. To lower the cost of energy produced by WECs optimal control methods are being investigated to provide more energy than traditional control strategies [51, 14, 68]. Optimal power absorption is achieved when the phase of the WEC is properly aligned with the wave excitation force [43].

Optimal control methodologies for WECs are continuously under development as they offer a way to harvest the most energy for a given WEC [40]. For example, Model Predictive Control (MPC) and Nonlinear Model Predictive Control (NMPC), which have gained significant traction in the WEC industry, are methods that solve a series of successive, small time horizon, optimal control problems [97]. Many optimal control algorithms require knowledge of the incident wave before it encounters the WEC [40, 47]. As the wave propagates a point

A will be called *up-wave* relative to point B, if point A interacts with the wave before point B. Conversely point B will be called *down-wave* relative to point A, if point A interacts with the wave before point B. To enable these control algorithms the future wave excitation force must either be measured or predicted in real-time with enough of a forecast horizon to improve energy production. The prediction requirements for the optimal control of WECs are studied in [47, 62] however, it is important to note that without up-wave prediction many optimal control algorithms, such as MPC, are impossible to implement [47].

This work studies wave excitation force prediction for WECs that can be implemented during real time deployments without significant measurement infrastructure. Wave tank tests are used in this work to provide experimental values for the incident wave elevation and WEC dynamics. An Extended Kalman Filter (EKF) is used to estimate the wave excitation force of WEC bodies in the wave tank using only the WEC body dynamics [31]. Excitation force prediction is achieved using AutoRegressive (AR) and AutoRegressive with eXogeneous input (ARX) models. Previous literature concludes that predictions using up-wave information with an ARX model do not significantly improve prediction for certain situations [83]. However, this work shows that the use of the up-wave information with an ARX model provides a significant improvement on prediction performance for the tested application. This work shows that ARX models may be able to utilize communication between wave energy devices in arrays to inform and improve the power production performance of WECs that are down-wave. A discussion of the difference between this work and the work of [83] are included below. The novel contributions of this work are:

- Excitation force predictions are made using only experimental data with irregular waves. None of the data used in this work was generated by numerical simulation.

- The real-time prediction is shown to work using easily available measurements, no external infrastructure for data collection is required.

- Up-wave information from other WECs is shown to appreciably improve the wave

excitation force prediction.

The contributions of this work are better understood after discussing the common methodologies that are used to obtain wave excitation force information. The methodology used in this work uses the WECs physical response to an incident wave to estimate the wave excitation force.

Figure 6.1 shows four commonly taken steps to obtain the future excitation force $F_{ex}(t)$. The first step shows information about the incident wave elevation. In literature, this incident wave elevation can either be simulated from a representative wave climate [32], or it can come from experimental time domain data [64]. The state dynamics of the WEC are the physical response of the body and can be obtained through simulation [64, 47], which inherently reduces the realistic nature of the data, through wave tank data, as with this work, or through ocean deployments. The third step shows the determination of the excitation force. This can either be done offline (not in real time) using measured wave elevation and the frequency response of the buoy as in [64] or it can be estimated in real time using the physical response of the WEC as implemented in this current work. Step four is either an offline or online (real-time) approach for wave excitation force prediction. Offline prediction can be used to show impressive results, as with [46], however these methods are not viable for a WEC deployment. Small arrows are shown in Fig. 6.1 moving around the methodical left-to-right progression of the figure, to show that some steps can be bypassed if desired. For instance, the use of external infrastructure or measurement systems would bypass the need for steps two or three, instead a prediction is made based on wave elevation as in [46, 83]. Each of these steps is typically treated separately in literature, citing the effectiveness of the separation principle [22]. This work focuses on the prediction of the wave excitation force using methods that can be implemented in real-time from physical data to provide the most realistic analysis possible.

An excellent overview of the wide range of prediction methodologies can be found in [40]. This includes methodologies that range from adaptive methods, such as autoregressive mod-

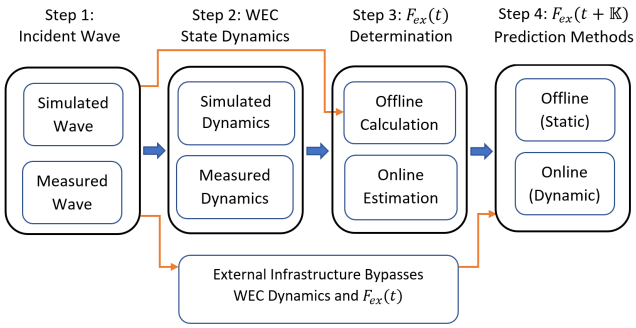

Figure 6.1: Depiction of the main steps by which excitation force is predicted. Arrows indicate paths that are possible with assumptions or processes outlined in section 6.1.

els, to nonlinear models that require offline training, such as Convolution Neural Networks. Deterministic methods, which have shown the promise of long timespan predictions when using external measurement infrastructure, are a current area of research as shown in [11].

Simulated WEC dynamics can be a useful proof of concept [30], however the conclusions about the effectiveness of predictions based on simulations, as shown in [64, 84], are subject to uncertainty. Without significant amounts of noise added to the simulation the dynamics will be much too ideal to give an accurate picture of the prediction effectiveness. The most common method of increasing realism is to add Gaussian noise directly to the simulated dynamics of the WEC, which does not accurately capture the systematic modeling errors of a heave only model operating in a wave tank with six degrees-of-freedom. A valuable sensitivity analysis using simulated data is given in [48].

References [74, 46, 83] show the development of prediction work using post-processed results. In the work of [46] a low pass filter is implemented in the forward and backward direction to eliminate phase lag which produces a time domain signal that is well suited to estimation using an autoregressive model. This work was extended by incorperating a Gaussian representation of the wave spectrum for prediction to further enhance the prediction of the stochastic wave process [74].

Offline filtering and external measurement infrastructure are combined with promising

results in [74]. Up-wave information is incorperated into the prediction in the form of an ARX model. However, unlike this current work, the up-wave information is provided by a measurement buoy rather than another WEC device that is already required to be in the deployment zone. In other estimation works the undisturbed water surface elevation is assumed to be measurable allowing for the investigating filtering methods such as [90] but the measurement methodology is not discussed.

The conclusion of [83] is that ARX models do not provide a significant enough increase in prediction to justify the added complexity. Key differences exist between this current work and the work done in [83]. First, [83] analyzes a WEC that is embedded in the coastline of an island, thus the waves will be shallow water waves, interacting with the shore, whereas this work analyzes a deep water wave situation. Second, the work of [83] provides predictions of the water surface elevation which will be a significantly more difficult to predict than the excitation force as shown in [64], since the excitation force convolution integral given in section 6.3 acts as a low pass filter of wave elevation. The conclusion of [83] also provides a commentary of the limitations of their evaluation of the ARX model.

The wave tank data that was used for this work is described in section 6.2. The dynamic models used for each body in the wave tank are given in section 6.3 and the wave excitation force estimation method is described in section 6.4. The autoregressive models used for prediction are found in section 6.5 and the prediction results are presented in section 6.6. Finally, a discussion of the results and outcomes of this research is given in section 6.7.

6.2 Available Data

Wave tank data was made available by the Oregon State University Northwest National Marine Renewable Energy Center's Marine and Hydrokinetics Open Data Project. For this work sixteen of the irregular wave runs, from the mooring study at the COAST lab at Plymouth University, were used [13]. The mooring study was used to analyze 1:10 scale bodies in waves in preparation for full scale deployment at an ocean test facility. Figure 6.2 shows the two bodies in the wave tank where tests were performed. Each of the bodies was

capable of motion in all six degrees of freedom. The up-wave body on the left is a model floating power system (FPS), a power station for the WEC deployments, and is attached to the other WEC with an umbilical cable. The down-wave body on the right is a model Oscillating Water Column (OWC) wave energy converter.

Sixteen irregular wave runs that tested an elastic "o-ring" as a taught mooring line were used for this study. Table 6.1 shows the peak period, T_p, significant wave height, H_s, "dead time" d_t, and the Goodness Of Fit (GOF) of the excitation force predictions for each body for each of the sixteen runs. The dead time is considered to be the time it would take a regular wave with a period equal to peak period from Table 6.1 to reach the down-wave body from the up-wave body. Each of the sixteen runs were sampled at 200Hz and were measured for roughly 600 seconds. The irregular waves were generated using a Bretschneider spectrum using the peak periods and wave heights listed in Table 6.1.

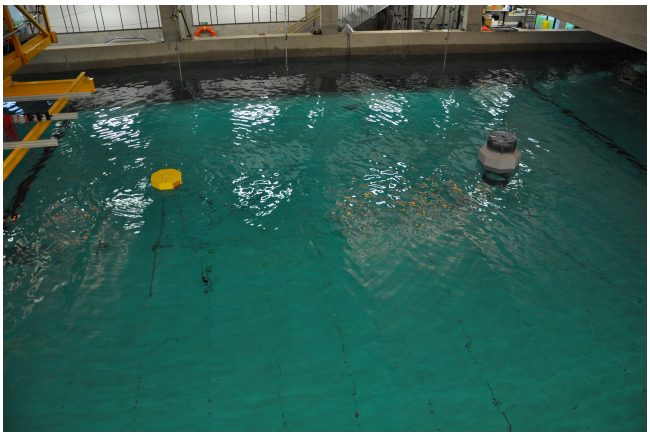

Figure 6.2: Photograph of the two 1:10 scale bodies at rest in the COAST lab. Waves approach from left, interacting first with the yellow floating power system, then the grey oscillating water column. The spacing between the bodies is fixed at 7.5 meters for all tests.

The original experiments for this work can be found in [13] and data and supplemental information can be found in [79]. Additional documentation of the methods and parameters that were used in the foundations of this numerical work can be found in [30]. The code

Run No.	H_s mm	T_p [s]	d_t [s]	GOF_1	GOF_2
1	50	1.90	2.53	90.4	75.0
2	175	1.90	2.53	81.5	72.5
3	300	1.90	2.53	72.8	76.9
4	50	2.37	2.03	94.8	83.1
5	175	2.37	2.03	92.3	82.2
6	300	2.37	2.03	86.7	79.1
7	50	2.69	1.79	94.7	87.1
8	175	2.69	1.79	93.3	87.7
9	300	2.69	1.79	87.1	82.1
10	50	3.16	1.52	92.1	88.5
11	175	3.16	1.52	93.8	89.6
12	175	3.95	1.22	95.6	86.6
13	175	4.74	1.01	95.9	81.1
14	175	5.53	0.89	95.2	79.3
15	375	2.06	2.33	76.1	76.4
16	375	2.37	2.03	84.0	78.5

Table 6.1: List of experimental runs from [13] that are considered in this work with corresponding significant wave height, H_s, peak period, T_p, and the "dead" time, d_t, it takes the wave to get from the up-wave body to the down-wave body. The GOF values are reported in percent as calculated by (6.19) and represent the GOF for the wave excitation force estimations of each run for the FPS (GOF_1) and the OWC (GOF_2) described in section 6.4.

used in this work will be made available on [28].

The wave tank tests used for this work were Froude scaled with a reduction ratio of 1:10. The 7.5 meters between the bodies in the wave tank is equivalent to a 75-m spacing between the full sized objects. Froude scaling ensures that gravity forces, such as the wave forces, are correctly scaled between the scale and full sized objects. Times, such as d_t, are scaled by the square root of the scaling factor. Since the dead time is determined using the peak period, the ratio between dead time to peak period is constant when Froude Scaling. Preliminary WEC array optimization shows that WECs are likely to be spaced well within 75 meters of each other [92]. In order to produce electricity at the lowest possible cost it is necessary to consider a wide range of factors such as overall array energy generation, permitting costs,

mooring, and environmental monitoring. The work of [92] shows that when optimizing a small number of WECs they will be spaced out to maximize the power production of each WEC. However, larger commercial scale WEC arrays require a tighter spacing of WECs to lower the overall cost of produced electricity [92].

6.3 WEC Models

Two different bodies were subjected to waves in the wave tank tests in [13]. To estimate the wave excitation force a model of each body is necessary. An arbitrary model for a partially submerged rigid body is developed, and then parameters relevant to each body are used in the estimation algorithm [31]. The potential based time domain integro-differential equation analyzed in [8, 44] has become the most prolific lumped parameter model for a WEC equation of motion. However, semi-emperical models or simplified lumped parameter models are also possible for WECs as shown in the modeling description given in [30] which provides more detail on the modeling description given in this section. The equation of motion of a semi-submerged body in heave is given by

$$M_v\ddot{z} = F_B + F_D + F_R + F_M + F_{ex}. \tag{6.1}$$

where the inertial force of the object is the product of the "virtual mass," M_v, and the heave acceleration, $\ddot{z}$. This "virtual mass" is the sum of the mass of the body and the infinite frequency added mass of the entrained fluid, as is traditionally used in the Cummins formulation [26]. The terms used in (6.1) are defined as: F_B is the hyrdostatic force on the object, F_D is the viscous drag force, F_R is the radiation damping, F_M is the restoring force from mooring lines, and F_{ex} is the wave excitation force. For this work the displacement of the body is z, and the dot notation represents derivatives with respect to time. The restoring force, F_M, is given by the product of a linear spring constant and the body displacement and the hydrostatic restoring force, F_B is equal to the weight of the displaced fluid, where a

constant body cross section is assumed. Discussion of the simplification of a general equation of motion to the form shown in (6.1) can be found in [30].

The potential based force terms of (6.1) are developed in agreement with the Cummins equation [26] which was originally developed to describe the motion of ships and is now applied to semi-submerged bodies. The viscous drag term is the lone nonlinear term in (6.1) as described in [8, 12]. The inertial, excitation, restoring, and radiation forces are assumed to be linear for the following development. Viscous drag was chosen as the only nonlinear term for this work as it is shown in literature to be a necessary addition to the linear Cummins equation [29, 12, 23]. Additionally the linear terms in (6.1) are modeled consistently with the excitation and drag identification work found in [30, 31]. The viscous drag is modeled using a quadratic Morison drag form [20, 103]. The drag in the heave direction is given by

$$F_D = -\frac{1}{2}\rho A_p C_D V|V| - bV, \tag{6.2}$$

where V is the relative velocity between the object and the water particles surrounding it. The density of the fluid is given by ρ, and A_p is the projected area of the object in the heave direction. A signed velocity square term is computed by taking the product of velocity, V, and the absolute value of the velocity, $|V|$. Finally, the drag coefficient is given by C_D. A discussion on the treatment of the viscous drag force as well as an identification method can be found in [30]. A small linear damping force bV is included to compensate for the fluid shear forces acting on the body and linear damping in the mooring lines. The coefficient b is based on the experimental response of each body at low velocities.

The forces acting on the WECs that result from radiated waves can be calculated in the time domain through the use of a convolution integral as illustrated in [26, 64]. In this work a state space realization of the convolution integral is created as an efficient method of computing the radiation force. The state space representation of the radiation force can be formed as

$$\dot{X}_r(t) = A_r X_r(t) + B_r \dot{z}(t), \tag{6.3}$$

$$F_R = - C_r X_r(t), \tag{6.4}$$

where X_r is the state vector of the realization. The state matrices A_r, B_r, and C_r are a non-unique linear realization of the convolution integral and are generated from the impulse response function of the system [57]. A fourth order realization is used for this work and a more detailed description of the Fourier transform inversion and computational considerations of describing the radiation force as a state space system is given in [30].

The wave excitation force can be calculated using the excitation force Impulse Response Function (IRF), $F_{IRF}(t)$, and the wave surface elevation, z_w, using the convolution integral,

$$F_{ex}(t) = \int_{-\infty}^{\infty} F_{IRF}(\tau) z_w(t - \tau) d\tau. \tag{6.5}$$

A truncated version of this convolution is used to compute the true value of the excitation force for this work. The time range of the numerical integration is truncated to be longer than the active response of the excitation IRF which is determined by applying the inverse Fourier transform on the frequency dependent excitation force calculated from a boundary element method [42].

The mooring lines are identical for the OWC and the FPS in the wave tank tests, however the other parameters and frequency response functions are determined independently for each body. Parameters for each of the bodies are provided in the estimation scripts available on GitHub [28].

6.4 Excitation Estimation

This work relies on an Extended Kalman Filter (EKF) to estimate the wave excitation forces on the FPS and the OWC. A detailed description of the implementation can be found in [31]. The Kalman filter incorporates measured outputs, a model, and error description to determine a statistically significant estimate of the state dynamics. A Kalman filter was chosen for the versatility of the estimator and ability for eventual implementations in real-time on board a WEC. With the extension to the nonlinear EKF the common model described in section 6.3 can be used for the purpose of state estimation.

Wave excitation force estimation is performed in this work by adapting a continuous-discrete extended Kalman filter with a disturbance model of the wave excitation force. This algorithm is used to observe a nonlinear continuous time model with discrete time experimental data points. The EKF is a nonlinear adaptation of the Kalman filter which observes a dynamic system in which zero-mean, Gaussian, white noise is assumed in both the dynamics and measurement. The model that is observed by the extended Kalman filter is described by

$$\dot{z}(t) = f(z(t), F_{ex}(t), t) + G(t)w(t) \tag{6.6}$$

$$\tilde{z}(t) = h(z(t), t) + v(t) \tag{6.7}$$

where f is the nonlinear state dynamics, h is the output function, $G(t)$ is a vector that describes the noise of each state, $w(t)$ is zero-mean Gaussian white noise with a variance $Q(t)$, and $v(t)$ is zero-mean, Gaussian, white noise with a variance of $R(t)$. The states are given by, $z(t)$, and output is given by, $\tilde{z}(t)$. The tilde symbol, $\tilde{\bullet}$, modifying the output, z, represents that this is an experimentally measured quantity. The output given by (6.7) is a column vector comprised of the measured heave position and measured heave velocity. The accuracy of the Kalman filter relies on knowledge of the process and measurement noise terms. Correct quantification of the process noise is essential for the EKF to function

effectively. For discussions concerning the determination of the process noise covariance see [24, 72].

The Kalman filter will iterate through the gain, update, and propagation steps for each discrete time in order to estimate the states of the system. The gain step calculates a matrix of gains that is used to correct a previous step's estimates based on the covariance of each state. The update step uses the calculated gain to adjust the covariance of each state and estimated value based on the difference between estimated and measured states. Finally, the propagation step calculates the covariance and state estimates of the next time step utilizing a Jacobian to linearize about the operating conditions. Details on the theory of the continuous-discrete EKF can be found in [24] and the implementation of the algorithm on a WEC application can be found in [30]. For this implementation of the EKF the Joseph stabilized form of the covariance update equation is used. In order to use the Kalman filter for estimation the model must be modified to provide the estimated parameter as a function of the observed states as described below.

6.4.1 Disturbance Model Estimation

Ocean waves and excitation forces are typically modeled as harmonic oscillators, or the sum of a large number of sinusoids, with coefficients determined by a wave energy spectrum and randomized phases [44]. The wave excitation force, $F_{ex}(t)$, is modeled as a disturbance to the system, as described by [64]. The regular wave representation of the excitation force is given as

$$F_{ex} = \mathbb{R}\left[\frac{H}{2}F_X(\omega_r)e^{i(\omega_r t)}\right], \tag{6.8}$$

where $\mathbb{R}$ represents the function to extract the real part of the argument, H is the peak to peak wave height, and $F_X(\omega_r)$ is the magnitude of the frequency domain excitation force for a given frequency, ω_r. The imaginary unit is denoted by i, and t is the time in seconds. This

excitation force can be generalized to irregular waves by

$$F_{ex} = \mathbb{R}\left[\int_0^\infty \sqrt{2\Delta\omega S(\omega)} F_X(\omega) e^{i(\omega t + \phi(\omega))} d\omega\right], \tag{6.9}$$

where $S(\omega)$ is the power of the wave spectrum as a function of frequency. The variable $\Delta\omega$ is the discrete distance separating each frequency and ϕ is vector of randomly generated phase angles in radians [52].

Equation (6.9) shows an infinite integral over a range of frequencies which is typically modeled as a discrete sum [44]. By looking at a single frequency component of the wave excitation force a description of the excitation force dynamics can be shown as,

$$\begin{aligned} f_{ex} &= sin(\omega t) \\ \ddot{f}_{ex} &= -\omega^2 sin(\omega t). \end{aligned} \tag{6.10}$$

The differential equation describing the excitation force can be implemented in the first order system of equations by

$$\begin{bmatrix} \dot{z}_1 \\ \dot{z}_2 \\ \dot{f}_{ex} \\ \ddot{f}_{ex} \\ \dot{x}_r \end{bmatrix} = \begin{bmatrix} z_2 \\ \frac{1}{M_v} F(z_1, z_2, f_{ex}, V, C_r x_r) \\ \dot{f}_{ex} \\ -\omega^2 f_{ex} \\ A_r x_r + B_r z_2 \end{bmatrix}, \tag{6.11}$$

where f_{ex} and $\dot{f}_{ex}$ are now states of the dynamic system. The states z_1 and z_2 represent the heave position and heave velocity respectively. The above expression describes a system where a single excitation force signal is estimated, similar to the direct identification method. However, (6.11) enforces that the estimated excitation force be a solution to the differential equation given in (6.10).

This excitation force estimation method can be generalized to use multiple wave frequen-

cies by using

$$\begin{bmatrix} \dot{z}_1 \\ \dot{z}_2 \\ \dot{f}_{ex} \\ \ddot{f}_{ex} \\ \dot{x}_r \end{bmatrix} = \begin{bmatrix} z_2 \\ \frac{1}{M_v} F(z_1, z_2, \Sigma \bar{f}_{ex}, V, C_r x_r) \\ I \dot{\bar{f}}_{ex} \\ -\Omega^2 \bar{f}_{ex} \\ A_r x_r + B_r z_2 \end{bmatrix} \tag{6.12}$$

for the dynamics. The bar over the excitation force denotes a vector of disturbance forces. The excitation force becomes $F_{ex} = \Sigma \bar{f}_{ex}$ to denote the sum of N excitation force terms that each oscillate at a different frequency. The term Ω denotes the diagonal matrix containing each of the N frequencies corresponding to the entries of $\bar{f}_{ex}$. The sum of each excitation force frequency allows for the excitation force to be modeled in a way that realistically describes the time derivative behavior of the wave excitation force. This method however requires knowledge of the wave climate for an appropriate choice of the disturbance wave frequencies. The initial conditions of the excitation terms should satisfy the differential equations given by (6.10). These initial conditions act as the terms that dictate the phase of the excitation force terms.

6.4.2 Implementing the EKF

The disturbance model introduces two states for every disturbance frequency that is used in the dynamics which is a significant increase in computational complexity over state estimation. However, the use of the equal energy approach when selecting wave frequencies of the disturbance model provides a more efficient way to estimate the incident wave with only few frequencies. This enables the use of the disturbance model to more realistically describe the wave excitation force. This approach not only provides wave frequencies that have a significant influence on the dynamics of the body, but it also defines the constraints on the initial conditions for the wave excitation force given by (6.10).

The nonlinear adaptation of the Cummins equation given by (6.1) requires the velocity of the body and the incident water particle velocity to obtain the relative velocity. This is achieved through the use of a finite difference estimation, developed in [31], that makes use of a linear relationship between the incident wave and wave excitation force. A numerical derivative can then be taken to provide an estimate of the water velocity, thereby enabling the nonlinear Cummins model to be implemented in the observer [31].

One of the greatest difficulties when implementing a Kalman filter is the determination of the process noise. The linear Kalman filter can be proven to be the optimal state estimator if both the process and measurement noises are Gaussian, zero mean, white noise. This linear Kalman filter can be extended to be the highly effective, nonlinear, extended Kalman filter, which relies on the same assumptions of process and measurement noise. While measurement noises are typically easy to obtain, accurate quantification of the process noise is impossible to know for sure and difficult to estimate [24]. The solution employed for this work relies on the assumption that any full scale deployed WEC will at some point have model tests. With these model tests a known experimental input can be used in a numerical simulation to determine an output. The simulated output is then compared to experimental output for the same input to obtain an error between the physical object and the model. The variance of this error is used as the estimate for the Gaussian process noise used in an EKF [31].

Results of the wave excitation force estimation for both the FPS and the OWC is used as the time domain data for section 6.6. The estimation performance of each run for the different wave climates is given in Table 6.1. Each of the estimations were performed over a using three disturbance frequencies and a fourth order radiation model.

6.5 Prediction Methods

While many system identification methods have been considered for wave excitation force prediction, autoregressive models were chosen for this study for their dynamic identification capability shown in the literature [46]. Autoregressive models are linear, parametric system identification models that model the current output of a stochastic process as being a linear

function of previous inputs and outputs. A thorough reference on the theory of autoregressive models and recursive autoregressive methods can be found in [66].

The autoregressive models are used to predict the wave excitation force of the down-wave body as the output, $y(k)$, and wave excitation force of the up-wave body as the input, $u(k)$. Figure 6.3 shows the input-output description in terms of the variables used for the autoregressive functions. The FPS interacts with the wave first and then the wave must travel 7.5 meters to the OWC. Only the time history of the output is used for the AR model and both input and output data are used for the ARX model.

Since irregular waves are non-stationary processes the wave spectra, and thus the time domain wave elevation, is expected to change between the up-wave and down-wave bodies. Results presented in section 6.6 show that this wave is stationary enough for the up-wave information to beneficially help down-wave prediction. Excitation forces are used as the inputs and outputs of this system as this is the time domain information that is most easily estimated. An added benefit of excitation force prediction is that the semi-submerged body acts as a physical low-pass filter of the incident wave elevation.

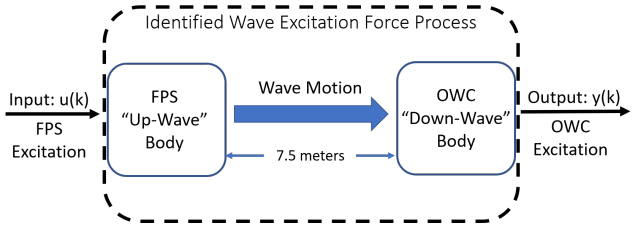

Figure 6.3: Depiction of the wave excitation force prediction. The estimated excitation force of the FPS is the input to the stochastic process and the output is the estimated excitation force of the OWC. Up-wave information is used to inform the prediction of down wave data.

6.5.1 AR Model

The autoregressive model in which the current output is only described as a linear combination of previous outputs will be referred to as the AR model and can be written as,

$$y(k) + a_1 y(k-1) + ... + a_n y(k-n) = \nu(k) \tag{6.13}$$

where $y(k)$ is the sampled output, the order, n, is the number of past outputs used in the AR model and $\nu(k)$ is the noise that describes the error of the model. For this work a model order of $n = 20$ is used and a discussion of model orders is given in section 6.6. One-step ahead predictions can be made by using the current value, $y(k)$, to solve for the next output,

$$\hat{y}(k+1) = -a_1 y(k) - ... - a_n y(k-n+1) \tag{6.14}$$

where the $\hat{\bullet}$ notation represents estimated data for times $k+1$ and beyond. An arbitrary timestep in the future, $\mathbb{K}$, can be predicted by making $\mathbb{K}$ successive 1-step ahead predictions, treating each predicted value as true. Propagation forward in time is given by

$$\hat{y}(k+\mathbb{K}) = -a_1 \hat{y}(k+\mathbb{K}-1) - ... - a_n \hat{y}(k+\mathbb{K}-n) \tag{6.15}$$

where the $\hat{\bullet}$ notation shows that each of the output values, y, has the potential to be estimated. Only output values for times greater than the current time, k, are estimated. Solving for the coefficients of $A = a_1, a_2, ..., a_n$ can be done by solving for the prediction error as a function of outputs, then the parameter estimation becomes a least squares problem [76].

The solution to the least squares problem can be calculated recursively, allowing for the parameters to change based on wave climate, WEC performance, and environmental uncertainties in real time. A forgetting factor is implemented in this work to weight the regression more heavily towards recent measurements. When the least squares regression is performed a weighting factor λ^{k_w} is introduced for each measurement, where λ is a scalar value between

zero and one and k_w represents the number of discrete time steps behind the current time [66]. Typical values of λ range from 0.98 to 0.995 [66], for this work a value of $\lambda = 0.99$ is chosen.

6.5.2 ARX Model

Unlike the AR model the ARX model uses past and current inputs in a linear combination to estimate the current output. The ARX model can be written as

$$\begin{aligned} &y(k) + a_1 y(k-1) + ... + a_n y(k-n) = \\ &b_1 u(k-1) + ... + b_m u(k-m) + \nu(k) \end{aligned} \tag{6.16}$$

where $u(k)$ is the output and the order, m, is the number of inputs that are used in the model. For this work a model order of $m = 50$ is used and a discussion of model orders is given in section 6.6. The ARX model (6.16) uses inputs that are one time step behind the current output. Recall that the experimental setup in section 6.2 has a spacing of 7.5 meters between the two bodies resulting in a "dead time". This "dead time" can be incorporated into the ARX model by using

$$\begin{aligned} &y(k) + a_1 y(k-1) + ... + a_n y(k-n) = \\ &b_1 u(k-1-m_k) + ... + b_m u(k-m-m_k) + \nu(k), \end{aligned} \tag{6.17}$$

where the delay m_k is the number of "dead" samples between when the input to the system can effect the output of the system.

The $\mathbb{K}$-step ahead predictions can be made in a similar manner to the AR model by

predicting successive 1-step ahead predictions, finally getting to the form

$$\begin{aligned} \hat{y}(k+\mathbb{K}) = b_1 u(k-1+\mathbb{K}-m_k) + ... \\ +b_m u(k-m+\mathbb{K}-m_k) - a_1 \hat{y}(k+\mathbb{K}-1) - ... \\ -a_n \hat{y}(k+\mathbb{K}-n). \end{aligned} \tag{6.18}$$

ARX models are limited to a prediction horizon no larger than the number of dead samples, m_k, as beyond this point inputs that relate to the output have not yet been collected. Section 6.6 will compare AR and ARX models with the same prediction horizons to achieve a fair evaluation of each models performance. The parameters of an ARX model can be formed as the solution to a recursive least squares problem as with the AR model, enabling the use of this dynamic model in real time.

6.6 Results

This section presents the comparisons between the predicted wave excitation force, found using the method described in section 6.5, and the estimated wave excitation force, found using the method given in section 6.4. The true value of wave excitation force is calculated using the non-causal convolution integral given by (6.5). Each estimation run is evaluated using a Goodness Of Fit (GOF). The GOF is computed by using the Normalized Mean Square Error (NMSE), given by the expression

$$GOF = 100\% \left(1 - NMSE\right) = 100\% \left(1 - \frac{||s(t) - \tilde{s}(t)||_2}{||s(t) - \bar{s}(t)||_2}\right), \tag{6.19}$$

where $s(t)$ is the time domain reference signal, the bar notation denotes the mean value, $\tilde{s}(t)$ is the estimated signal, and the notation $||\bullet||_2$ represents the L2-norm of a vector [69]. The GOF is represented as a percentage as shown in (6.19), where 100% is a perfect match between predicted and true.

6.6.1 Time Domain Predictions

Figure 6.4 shows a two second ahead prediction using both AR and ARX models. As seen in this figure, while the AR model predicts the largest peaks better than the ARX model, the ARX prediction is more aligned with the phase of the true signal.

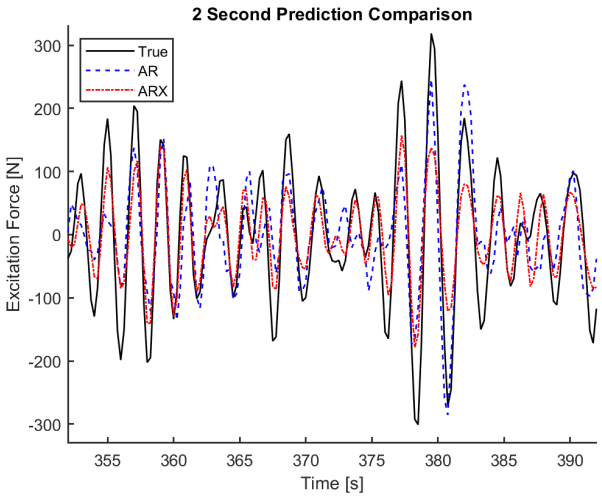

Figure 6.4: Comparison of AR and ARX prediction for a two second horizon during a wave climate with a significant wave height of 175 mm and a peak period of 2.37 seconds (Run No. 5). AR GOF = 56.3% and ARX GOF = 73.5%

These predictions were performed for a forty second time span with a sampling rate of 4Hz to show the variability in the irregular waves. Run number 5 from Table 6.1 was chosen as it is the lowest frequency wave in which the ARX model can be implemented for the 2 seconds of prediction. These two tests, as well as those in sections 6.6.2 and 6.6.3, are performed using the same 150 second training time before the evaluation time period. It was found that the autoregressive functions can adapt to the current wave climate from a standard initialization in this training time.

6.6.2 Comparison of ARX and AR models

Figure 6.5 shows the average GOF of the AR and ARX models as a function of prediction horizon. The ARX model provides a significant performance increase over the AR model as the prediction horizon increases. Sixteen different irregular wave climates are used to determine the mean GOF in Fig. 6.5. The prediction horizons that were evaluated are shown with circles on Fig. 6.5. The confidence intervals shown in this section represent two standard deviations (95%) from the mean GOF for the sixteen different wave climates. The confidence interval overlap between the AR and ARX predictions in Fig. 6.5 show that the lowest performing ARX runs can be surpassed by some of the highest performing AR runs. However, the mean performance of each method shows that the ARX is able to more accurately predict the wave excitation force.

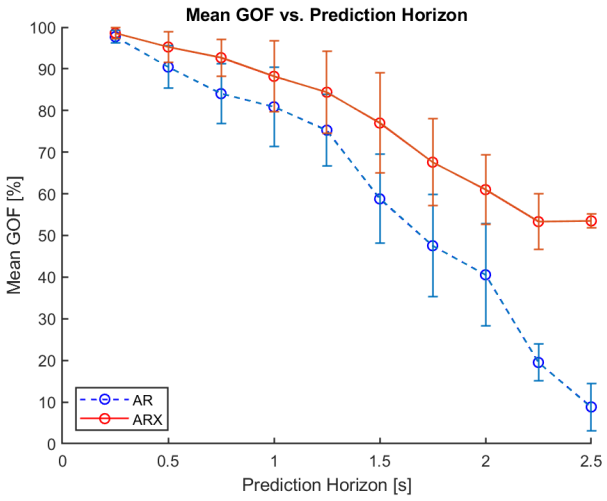

Figure 6.5: Comparison of AR and ARX prediction for an increasing time horizon. Error bars are included to show a 95% confidence interval for the runs used to calculate each mean GOF.

As shown in Table 6.1 the dead time for many runs are not large enough to utilize the ARX model with the horizon shown in Fig. 6.5. This is taken into account by removing the

run from the GOF calculation when the horizon has exceeded the dead time. If the selected horizon means that the ARX model is not viable to be included when calculating the mean ARX performance then the AR model for that wave run is not used to calculate the mean AR performance. This is meant to provide a comparison of only equivalent situations rather than biasing the performance evaluation toward the ARX model.

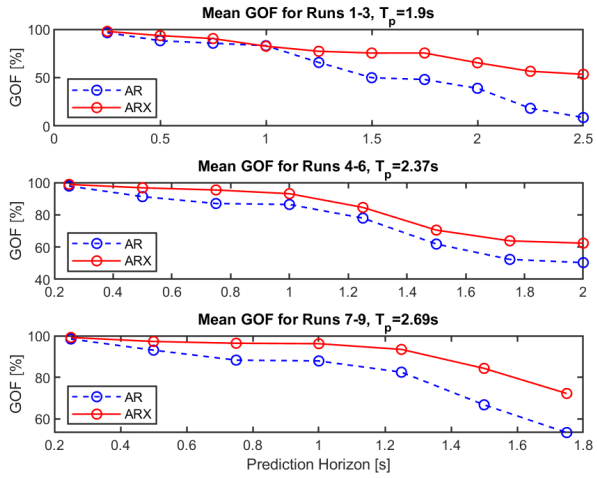

Figure 6.6: Comparison of average performance of AR and ARX models for runs that have been grouped by wave period.

The wave periods of 1.9s, 2.37s, and 2.69s each had 3 runs with significant wave heights of 50mm, 175mm, and 300mm. The three subplots of Fig. 6.6 each show the mean GOF of all of the run with 1.9s, 2.37s, and 2.69s wave periods. The prediction horizons that were evaluated are shown with circles on Fig. 6.6. The maximum prediction horizon is dependent on the peak period of the wave as discussed in section 6.3. Figure 6.6 shows the superior performance of the ARX model. For small prediction horizons the discrepancy between the AR and ARX models is small, due to the AR model being capable of reasonable prediction at short time horizons.

6.6.3 Enhancement of AR with Short-term ARX

One of the key advantages that the AR model has over the ARX model is that there is no fixed limit to the maximum prediction horizon. Figures 6.5 and 6.6 have required that prediction of the AR model stop at the dead time as the ARX model is unable to perform predictions past the dead time, even though in some cases the AR prediction was still accurate enough to be useful to a control algorithm.

Figure 6.7 shows an implementation of the standard AR model and modified ARX+AR model. As with Fig. 6.5 the prediction horizons that were evaluated are shown with circles on Fig. 6.7, and 95% confidence intervals for each method are shown. This modification implements the AR model in series after the ARX model. This implementation requires both models to be trained recursively as time progresses. The ARX model is used to predict to the maximum horizon, the dead time, and then the AR model utilizes the predicted excitation force values and predicts a further 1/2 second beyond the dead time. The $\mathbb{K}$-step ahead prediction using both the ARX and AR models in series is given by (6.13), where the index of the output variable determines how each output is predicted. Let the output variable be indexed using a single index k', so $y(k')$ is the output used in (6.13). For every output with an index in the range, $k < k' \leq m_k$ then the value of $y(k')$ is calculated using (6.16) and for every value of $k' > m_k$ then $y(k')$ is computed using (6.13). Figure 6.7 shows that the mean performance of the series model consistently outperforms the AR model alone. This modification shows that even with a strict limit on prediction horizon the ARX model may still contribute to effective prediction.

6.6.4 Model Orders and Froude Scaling

Overall, the ARX model outperforms the AR model as established by the GOF of various different prediction horizons. However the ARX model is computationally more complex than the AR model. The number of difference equation coefficients for the various runs presented in this section were $n = 20$ and $m = 50$, as previously described. There is room

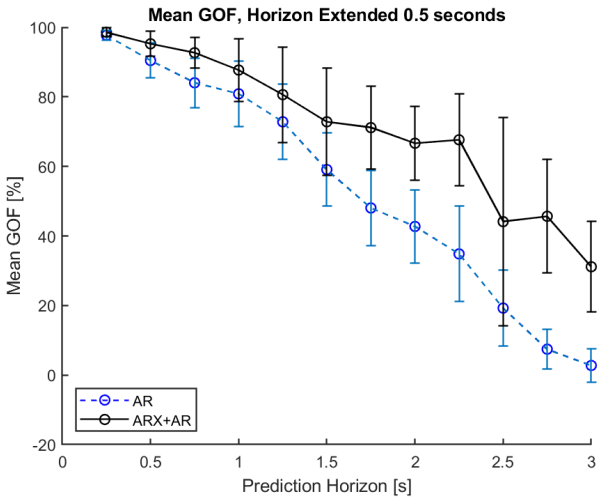

Figure 6.7: Comparison of AR and series ARX+AR models for predictions 0.5 seconds past that of Fig. 6.5. Error bars are included to show a 95% confidence interval for the runs used to calculate each mean GOF.

for performance improvement through the use of an optimization method to determine the best choice of n and m for each wave climate. However, for this work the general application of the autoregressive models was employed to evaluate the effectiveness of each model on a range of wave climates, rather than assessing the ability of each model to be tuned for a particular wave climate.

These wave tank tests were performed on 1:10 scale objects, as such the timescales are scaled down using the Froude method of dimensional analysis. The two second ahead prediciton of Fig. 6.4 when scaled up appropriately replicates a wave with a peak period of 7.5 seconds and a significant wave height of 1.75 meters, much closer to the waves experienced in an ocean deployment. As the wave is scaled an equivalent scaling of the prediction horizon would be 6.3 seconds. This prediction horizon is significant when benchmarked with the work of [47, 62] which show that predictions around one period can be used to improve power performance.

6.7 Conclusion

This work demonstrates that for WECs in a wave farm, information from up-wave WECs can be used to improve the prediction capabilities of down-wave WECs. This work implements wave excitation force prediction using only methods that would be viable during ocean deployments and do not require extensive measurement infrastructure.

This paper presents an experimental validation of wave excitation force prediction using both ARX and AR models. Irregular wave tank tests on two 1:10 scale bodies were used for this work. Time domain models were constructed using a nonlinear lumped parameter model for each body in the wave tank. Using the continuous time models the wave excitation force was modeled as a harmonic disturbance to the system of differential equations. An extended Kalman filter was implemented to observe discrete time measurements and provide an estimated wave excitation force. Using the estimated excitation force two different autoregressive models were implemented to predict the future wave excitation force. A comparison between an AR model that uses only past outputs and an ARX model that takes into account both past inputs and outputs was presented.

Current literature, [47, 62] shows that a predicted wave excitation force can result in a significant increase in the power production of WECs. This work shows that up-wave information can be used to increase the effective wave excitation force prediction horizon. This leads naturally to the conclusion that up-wave information in a WEC array could be used to increase the power production some WECs in a wave energy farm.

This implementation of wave excitation estimation and prediction work stands alone as a work that uses only physical measurements and methods that can be implemented in real time to show the prediction capabilities of WECs. This work shows that up-wave information can be very beneficial to the prediction capabilities of WECs. ARX models may offer enhanced capabilities to WECs in wave farms beyond that of the standard adaptive prediction capabilities currently studied in the industry.

Chapter 7

CONCLUSION

In this work the various dynamic models of Wave Energy Converters (WECs) are evaluated. Sensitivity analysis to changes in the models are performed as well as comparisons of the magnitudes of various forces to give insight into the effect on WEC performance. An investigation was performed on the magnitude of the viscous drag in comparison to the radiated wave force, since it is typical for WEC models to omit the viscous drag in favor of the radiated wave force to retain a linear model, despite viscous drag being shown to produce up to a 30% change in simulated power production [8]. The viscous drag force was found to be worth inclusion in the dynamics of a heaving semi-submerged float for high energy sea states. An extended Kalman filter, from existing literature, was applied to a nonlinear WEC model in simulated waves in order to show that the viscous drag coefficient can be identified as an estimated state in the dynamic model.

It is shown that an extended Kalman filter can effectively estimate the wave excitation force using only the dynamic response of the heaving object as measured outputs. With estimated wave tank excitation forces, autoregressive models are used to predict the wave excitation force. Both the wave excitation force estimation and prediction were evaluated with experimental response of a 1:10 scale mooring study performed in a wave tank. The estimation and prediction work using wave tank experiments provides an evaluation of excitation force prediction methodologies that can be implemented in real time without significant measurement infrastructure.

7.1 Analysis of WEC Models

This work begins by developing a first principles model of a scaled WEC deployment in Lake Washington. The model is validated in the frequency and time domain. The WEC relied on Magnetostriction to generate electricity which meant that the rate of change in tension between the float and the heave plate was directly proportional to the generated power. A sensitivity analysis was performed to gain insight into this specialized type of WEC. Fluid drag on the heave plate was essential to ensure that the power take off unit was never in a slack state. However, the float buoyancy and heave plate mass were shown to have the greatest effect on the power production of this device.

This work then proceeds to perform an analysis of the Cummins equation, the most prolific WEC model, modified with a Morison drag term. The goal was to quantify the contribution of each modeled force on the dynamics of a wave energy float, which will play a significant role in the overall dynamics and power generation of point absorbing WECs. A comparison of analytical and numerical methods for calculating the wave radiation force for simple geometries is given, showing only small differences in the computed forces. An evaluation of an experimentally determined model shows that at a more energetic wave environment viscous drag tends to be more dominant than the force corresponding to the radiated waves. This same conclusion is shown to be true when simulating the dynamics of semi-submerged floats with the modified Cummins equation.

To address the uncertainty in viscous drag coefficient, present in the Morison drag modification, an implementation of an extended Kalman filter is used to estimate dynamic states and the viscous drag coefficient. Several lumped parameter models representing those used throughout the WEC industry are evaluated and a potential based model with a Morison drag term is shown to be the most effective. Numerical tests were performed to evaluate the range of conditions that can be estimated. It was shown that a drag coefficient could be identified with a wide range of noise and sampling rate. Additionally, it is shown that with a sufficiently detailed model a time-varying drag coefficient can be estimated.

7.2 Excitation Force Estimation and Prediction

Use of optimal control strategies for WECs relies on time domain date values of the wave excitation force. This force is difficult to obtain experimentally and requires a non-causal convolution integral to calculate analytically. A Kalman filter is used to provide an estimate of the wave excitation force using the WEC body dynamics as the measured variables. Two different wave excitation force models are used with an extended Kalman filter to provide the estimated data. Both a direct estimation of the wave excitation force and a disturbance model of the wave excitation force are evaluated using a 1:10 scale wave tank test. A simple approximation method of determining the incident wave velocity was implemented to enable the relative velocity calculations for the nonlinear Morison drag term. Systematic methods for determining process noise and disturbance frequencies are given in this work. A wide range of wave tank data with irregular waves is used to evaluate the wave excitation force prediction and estimation. The method which models the wave excitation force as a disturbance model of summed sinusoidal components is shown to outperform the direct method of estimation.

Predicted wave information is currently used in model predictive control to obtain up to 90% of the ideal constrained optimum power production [50]. To further enable optimal control strategies which rely on foreknowledge of the wave excitation force autoregressive models were used to predict the wave excitation force as a function of past excitation force estimations. These estimations were obtained from experimental datasets using only the body dynamics of the WEC. It is shown that incorporating the estimated wave excitation force of an up-wave WEC can provide a significant improvement in the prediction capabilities of a down-wave WEC. This prediction performance increase is brought about using only methods that can be implemented in real time.

This work reduces the barriers to the development of WECs through its critical look into the significance of each force in the traditional dynamic models. The capability of WECs to identify and update dynamic variables will reduce the widespread uncertainty in

the WEC modeling community, particularly in reference to the viscous drag coefficient which is widely used but often unknown. It is widely accepted that a prediction horizon offers a key to increasing the power production of WECs which is essential to enable the commerical viability of WECs. The experimental implementation of wave excitation force prediction and estimation using viable deployment methods, described in this work, enables some functional use of optimal control systems in this field, which offer more efficient power generation for wave energy converters.

7.3 Future Work

This work demonstrates the value of up-wave data for prediction, which directly enables the optimal control methodologies available to wave farms. However, the implications for overall power production from enhanced prediction capabilities of a wave farm is not well known and would be an excellent avenue of future research. As WECs are spaced closer to each other the ability of down-wave WECs to predict their wave excitation forces is improved, however it is often understood that close spacing of WECs will degrade the power production of the individual WECs. An optimization of the layouts and spacing of a wave farm, taking into account the increased control capabilities afforded by close spacing, would provide necessary insight for WEC developers.

Additionally, the cost effectiveness of external measurement infrastructure should be studied. Measurement devices deployed to enhance the prediction capabiliteis of WECs may provide a cost effective way to increase the power production of each WEC. It is feasible that, even with the additional cost of measurement devices, the enhanced prediction enables more effective control which would in turn lead to increased survivability of each WEC, thereby decreasing the overall cost of energy for a wave farm.

Future work should also include a continued analysis of the limitations of autoregressive functions for wave excitation force prediction. From the literature it is clear that there are certain applications for which up-wave data is beneficial while it is shown to be ineffective in other cases. It would be a significant contribution to the WEC industry to quantify the

conditions in which up-wave and autoregressive methods can be applied and be expected to result in significant power production performance increases.

BIBLIOGRAPHY

[1] Seabased AB. Seabased AB website: http://www.seabased.com/en/, 2013.

[2] O. Abdelkhalik, S. Zou, R. Robinett, G. Bacelli, and D. Wilson. Estimation of excitation forces for wave energy converters control using pressure measurements. *International Journal of Control*, 90(8):1793–1805, 2016.

[3] M. Garcia Abril, F. Paparella, and J. V. Ringwood. Excitation force estimation and forecasting for wave energy applications. In *International Federation of Automatic Control*, pages 14692–14697. Elsevier, 2017.

[4] S. Adee. This renewable energy source is swell: Oceanlinx begins building third-generation ocean-swell-to-energy generator. IEEE Spectrum, October 2009.

[5] International Energy Agency. Ocean energy systems. OES website: https://www.ocean-energy-systems.org/, 2020.

[6] Wave Dragon ApS. Wave dragon. Wave Dragon Website: www.wavedragon.net/, 2005.

[7] A. Babarit and et. al. Nemoh, 2017.

[8] A. Babarit, J. Hals, M.J. Muliawan, A. Kurniawan, T. Moan, and J. Krokstad. Numerical benchmarking study of a selection of wave energy converters. *Renewable Energy*, 41:44-63, 2012.

[9] S. Beatty. Self-reacting point absorber wave energy converters. Doctoral Dissertation, 2015.

[10] S. Beatty, M. Hall, B. Buckham, P. Wild, and B. Bocking. Experimental and numerical comparisons of self-reacting point absorber wave energy converters in regular waves. *Ocean Engineering*, 2015.

[11] M.R. Belmont, J. Christmas, J Dannenberg, T. Hilmer, J Duncan, J.M. Duncan, and B. Ferrier. An examination of the feasibility of linear deterministic sea wave prediction in multidirectional seas using wave profiling radar: Theory, simulation, and sea trials. *Journal of Atmospheric and Oceanic Technology*, 31(7):1601–1614, 2014.

[12] Majid A. Bhinder, Aurélien Babarit, Lionel Gentaz, and Pierre Ferrant. Potential time domain model with viscous correction and cfd analysis of a generic surging floating wave energy converter. *International Journal of Marine Energy*, 10:70-96, June 2015.

[13] Bret Bosma, Florent Thiebaut, and Wanan Sheng. Comparison of a catenary and compliant taut mooring system for marine energy systems. In *European Wave and Tidal Energy Conference*, 2015.

[14] Ted K. A. Brekken. On model predictive control for a point absorber wave energy converter. In *IEEE Trondheim Power Tech*, 2011.

[15] C.E. Brennen. A review of added mass and fluid inertial forces. Technical report, Naval Civil Engineering Laboratory, 1982.

[16] A. Brown. *The Effects of Ocean Variability and Breaking Waves on Wave Energy Converter Reliability and Survivability*. PhD thesis, University of Oregon, 2014.

[17] A. Brown and J. Thomson. Phase-resolved heave plate dynamics for wave energy converters. In *Proceedings of the 4th Marine Energy Technology Symposium*, 2016.

[18] K. Budal and J. Falnes. Interacting point absorbers with controlled motion. *Power from sea waves*, pages 381–399, 1980.

[19] Oregon State University Northwest National Marine Renewable Energy Center. Energy from waves. Website: http://nnmrec.oregonstate.edu/education/energy-waves, 2017. Figure used with permission.

[20] S. Chakrabarti. *Handbook of Offshore Engineering, Volumes 1-2*, chapter 4, pages 137-161. Elsevier, 2005.

[21] S.K. Chakrabarti and D.C. Cotter. Hydrodynamic coefficients of a moored semisubmersible in waves. *Journal of Offshore Mechanics and Arctic Engineering*, 114(1):9–15, 1992.

[22] Chi-Tsong Chen. *Linear System Theory and Design*. Oxford University Press, fourth edition, 2013.

[23] A. Combourieu, M. Lawson, A. Babarit, K. Ruehl, A. Roy, R. Costello, W. Laporte, and H. Bailey. Wec^3: Wave energy converter code comparison project. In *Proceedings of the* 11^{th} *European Wave and Tidal Energy Conference*, 2015.

[24] John L. Crassidis and John L. Junkins. *Optimal Estimation of Dynamic Systems*. Chapman and Hall/CRC Applied Mathematics and Nonlinear Science. CRC Press, 2nd edition, 2011.

[25] J. Cruz, editor. *Ocean Wave Energy Current Status and Future Prespectives*. Springer, 2008.

[26] W. Cummins. The impulse response function and ship motions. *Schiffstechnik*, 1962.

[27] J. Davidson, S. Giorgi, and J. Ringwood. Identification of wave energy device models from numerical wave tank data-part 1: Numerical wave tank identification tests. *IEEE Transactions on Sustainable Energy*, 2016.

[28] Andrew F. Davis. Github repository, 2020.

[29] Andrew F. Davis and Brian C. Fabien. Modeling and analysis of the time domain forces of a wave energy conveter model. In *Proceedings of the 3rd Marine Energy Technology Symposium*, 2015.

[30] Andrew F. Davis and Brian C. Fabien. Systematic identification of drag coefficients for a heaving wave follower. *Journal of Ocean Engineering*, 168, 2018.

[31] Andrew F. Davis and Brian C. Fabien. Wave excitation force estimation of wave energy floats using extended kalman filters. *Journal of Ocean Engineering*, 198, 2020.

[32] Andrew F. Davis, Jim Thomson, Tim R. Mundon, and Brian C. Fabien. Modeling and analysis of a multi degree of freedom point absorber wave energy converter. In *Proceedings of the 33rd International Conference on Ocean, Offshore and Arctic Engineering*, volume 8A, 2014.

[33] A. Day, A. Babarit, A. Fontane, Y. He, M. Kraskowski, M. Murai, I. Penesis, F. Salvatore, and H. Shin. Hydrodynamic modelling of marine renewable energy devices: A state of the art review. *Ocean Engineering*, 2015.

[34] A. de Andres, R. Guanche, J. Armesto, F. Vidal, and I. Losada. Time domain model for a two-body heave converter: model and applications. *Ocean Engineering*, 2013.

[35] A.D. de Andrés, R. Guanche, J.A. Armesto, F. del Jesus, C. Vidal, and I.J. Losada. Time domain model for a two-body heave converter: Model and applications. *Ocean Engineering*, 75:116–123, 2013.

[36] T. et. al. Dewhurst. Dynamics of a floating platform mounting a hydrokinetic turbine. *Marine Technology Society Journal*, 47(4):45–56, 2013.

[37] Benjamin Drew, Andrew R. Plummer, and Mehmet Sahinkaya. A review of wave energy converter technology. *Proceedings of the Institution of Mechanical Engineers, Part A: Journal of Power and Energy*, 2009.

[38] Wave Star Energy. Wavestar. Wavestar website http://wavestarenergy.com/, 2017.

[39] Brian C. Fabien. *Nonlinear Approaches in Engineering Applications*, chapter Equilibrium of a Submerged Body with Slack Mooring, pages 211–236. Springer, 2012.

[40] N. Faedo, O. Olaya, and J. V. Ringwood. Optimal control, MPC and MPC-like algorithms for wave energy systems: An overview. *IFAC Journal of Systems and Control*, 1:37–56, 2017.

[41] A. F. Falcao. Wave energy utilization: A review of technologies. *Renewable and Sustainable Energy Reviews*, 14:720–724, Apr. 2010.

[42] J. Falnes. *Ocean waves and oscillating systems: linear interactions including wave-energy extraction*, chapter 2-5. Cambridge University Press, 2002.

[43] J. Falnes. A review of wave-energy extraction. *Marine Structures*, 2007.

[44] M. Folley, editor. *Numerical Modelling of Wave Energy Converters State-of-the-art techniques for single devices and arrays*, chapter 3,7,12. Elsevier, 2016.

[45] M. Folley and T. Whittaker. Spectral modelling of wave energy converters. *Coastal Engineering*, 57:892-897, 2010.

[46] F. Fusco and J. V. Ringwood. Short-term wave forcasting for real-time control of wave energy converters. *IEEE Transactions on Sustainable Energy*, 1:99–106, 2010.

[47] Francesco Fusco and John V. Ringwood. A study of the prediction requirements in real-time control of wave energy converters. *IEEE Transactions on Sustainable Energy*, 3(1), 2012.

[48] M. Garcia-Abril, F. Paparella, and J.V. Ringwood. Excitation force estimation and forecasting for wave energy applications. *IFAC-PapersOnLine*, 50:14692–14697, July 2017.

[49] S. Giorgi, J. Davidson, and J. Ringwood. Identification of wave energy device models from numerical wave tank data-part 2: Data-based model determination. *IEEE Transactions on Sustainable Energy*, 2016.

[50] J. Hals, J. Falnes, and T Moan. Constrained optimal control of a heaving buoy wave-energy converter. *Journal of Offshore Mechanics and Arctic Engineering*, 133, February 2011.

[51] Y. Hong, R. Waters, C. Bostrom, M. Eriksson, J. Engstrom, and M. Leijon. Review on electrical control stategies for wave energy converting systems. *Renewable and Sustainable Energy Reviews*, 31:329–342, 2014.

[52] Yu Hsiang, Kelley Ruehl, and et. al. Wec-sim user manual, 2017.

[53] A. Hulme. The wave forces acting on a floating hemisphere undergoing forced periodic oscillations. *J. Fluid Mech.*, 121:443-463, 1982.

[54] Gabriel Ibarra-Berastegi, Jon Sáenz, Alain Ulazia, Paula Serras, Ganix Esnaola, and Carlos Garcia-Soto. Electricity production, capacity factor, and plant efficiency index at the mutriku wave farm (2014-2016). *Ocean Engineering*, 147:20–29, 2018.

[55] L. Johanning, G.H. Smith, and J. Wolfram. Mooring design approach for wave energy converters. *Proceedings of the Institute of Mechanical Engineers, Part M: Journal of Engineering for the Maritime Environment*, 2006.

[56] G.J. Komen, L. Cavaleri, M. Donelan, K. Hasselmann, S. Hasselmann, and P.A.E.M. Janssen. *Dynamics and Modelling of Ocean Waves*. Cambridge, 1994.

[57] E. Kristiansen, A. Hijulstad, and O. Egeeland. State-space representation of radiation forces in time-domain vessel models. *Ocean Eng.*, 32:2195-2216, 2005.

[58] A. Kurniawan, J. Hals, and T Moan. Assessment of time domain models of wave energy conversion systems. In *Proceedings of the* 9^{th} *European Wave and Tidal Energy Conference*, 2011.

[59] M. Lawson, Y. Yu, A. Nelessen, K. Ruehl, and C. Michelen. Implementing nonlinear buoyancy and excitation forces in the wec-sim wave energy converter modeling tool. In *Proceedings of the* 33^{rd} *International Conference on Ocean, Offshore and Arctic Engineering*, 2014.

[60] C.H. Lee and Newman J.N. *WAMIT User Manual*. WAMIT Inc. Version 7.0.

[61] Guang Li, George Weiss, Markus Mueller, Stuart Townley, and Mike R. Belmont. Wave energy converter control by wave prediction and dynamic programming. *Renewable Energy*, 48, 2012.

[62] Liang Li, Zhiming Yuan, Yan Gao, and Xinshu Zhang. Wave force prediction effect on the energy absorption of a wave energy converter with real-time control. *IEEE Transactions on Sustainable Energy*, 10(2):615–624, 2019.

[63] Y. Li and Y. Yu. A synthesis of numerical methods for modeling wave energy converter-point absorbers. *Renewable and Sustainable Energy Reviews*, 16:4352-4364, 2012.

[64] B Ling and B. Batten. Using extended kalman filters for real-time estimation of excitation forces on a wave energy converter. In *Proceedings of the 3rd Marine Energy Technology Symposium*, 2015.

[65] Bradley A. Ling. Real-time estimation and prediction of wave excitation forces for wave energy control applications. Master's thesis, Oregon State University, June 2015.

[66] Lennart Ljung. *System Identification Theory For The User*. Pretence Hall, second edition, 1999.

[67] Orcina Ltd. Orcaflex documentation. Orcina Website: https://www.orcina.com/SoftwareProducts/OrcaFlex/Documentation/Help/.

[68] Aleix Maria-Arenas, Aitor J. Garrido, Eugen Rusu, and Izaskun Garrido. Control strategies applied to wave energy converters: State of the art. *energies*, 12(16), 2019.

[69] Mathworks. Matlab documentation. MATLAB Website: https://www.mathworks.com/help/ident/ref/goodnessoffit.html, 2019.

[70] M. E. McCormick. *Ocean wave energy conversion*. Dover Publications, 2007.

[71] M.E. McCormick. *Ocean Engineering Wave Mechanics*, chapter 2, pages 24–35. John Wiley and Sons, 1973.

[72] R. K. Mehra. On the identification of variances and adaptive kalman filtering. *IEEE Transactions on Automatic Control*, 15(2):175–184, 1970.

[73] J. Morison, M. O'Brien, J. Johnson, and S. Schaaf. The force exerted by surface waves on piles, 1950.

[74] A. Mérigaud and J. V. Ringwood. Incorporating ocean wave spectrum information in short-term free-surface elevation forecasting. *IEEE Journal of Oceanic Engineering*, 44(2):401–414, April 2019.

[75] B. et al Nair. Low-cost utility-scale wave energy enabled by magnetostriction. In *Marine Energy Technology Symposium (GMREC), Washington, DC (2013)*, Washington, DC, 2013.

[76] Oliver Nelles. *Nonlinear System Identification From Classical Approaches to Neural Networks and Fuzzy Models*. Springer, 2000.

[77] J.N. Newman. *Marine Hydrodynamics*, chapter 6, pages 39-45. MIT Pres, 1977.

[78] H.-N. Nguyen and P. Tona. Wave excitation force estimation for wave energy converters of the point absorber type. *IEEE Transactions on Control Systems Technology*, 2017.

[79] NNMREC. Marine and hydrokinetics open data project, 2017.

[80] Inc. Ocean Power Technologies. Pb3. Ocean Power Technologies website: http://www.oceanpowertechnologies.com/, 2017.

[81] T. Ogilvie. Recent progress towards the understanding and prediction of ship motions. In *Proceedings of the 5th Symposium on Naval Hydrodynamics*, pages 3-128, 1964.

[82] Emre Ozkop and Ismail H. Altas. Control, power and electrical components in wave energy conversion systems: A review of the technologies. *Renewable and Sustainable Energy Reviews*, 67:106–115, January 2017.

[83] Francesco Paperella, Kieran Monk, Victor Winands, M.F.P. Lopes, Daniel Conley, and John V. Ringwood. Up-wave and autoregressive methods for short-term wave forecasting for an oscillating water column. *IEEE Transactions on Sustainable Energy*, 6(1):171–178, 2015.

[84] Yerai Peña-Sanchez, Marina Garcia-Abril, Francesco Paparella, and John V. Ringwood. Estimation and forecasting of excitation force for arrays of wave energy devices. *IEEE Transactions on Sustainable Energy*, 9(4), October 2018.

[85] PMEC. Pacific marine energy center, 2020.

[86] Oscilla Power. Triton wec. Oscilla Power website: https://oscillapower.com/triton-wec/, 2016.

[87] Pelamis Wave Power. Pelamis. Pelamis wave power Website: https://www.pelamiswave.com/, 2017.

[88] M. P. Retes et al. A review of non-linear approaches for wave energy converter modelling. In *Proceedings of the 11th European Wave and Tidal Energy Conference*, Sept. 2015.

[89] S. H. Salter. Wave power. *Nature*, 249:720–724, 1974.

[90] M. P. Schoen, J. Hals, and T. Moan. Wave prediction and robust control of heaving wave energy devices for irregular waves. *IEEE Transactions on Energy Conversion*, 26(2):627–638, June 2011.

[91] J.T. Scruggs, S.M. Lattanzio, A.A. Taflanidis, and I.L. Cassidy. Optimal causal control of a wave energy converter in a random sea. *Applied Ocean Resarch*, 42:1–15, 2013.

[92] Christopher J. Sharp. Wave energy converter array optimization: Array economic analysis and preliminary results of a genetic algorithm approach introducing cost factors. Master's thesis, Oregon State University, 2015.

[93] Wanan Sheng. Wave energy conversion and hydrodynamics modelling technologies: A review. *Renewable and Sustainable Energy Reviews*, 109:482–498, July 2019.

[94] R. Taghipour, T. Perez, and T. Moan. Hybrid frequency-time domain models for dynamic response analysis of marine structures. *Ocean Engineering*, 35:685-705, 2008.

[95] J.H. Todalshaug, G.S. Ásgeirsson, E. Hjálmarsson, J. Maillet, P. M Ïller, P. Pires, M. Guérinel, and M. Lopes. Tank testing of an inherently phase controlled wave energy converter. In *Proceedings of the* 11^{th} *European Wave and Tidal Energy Conference*, 2015.

[96] Nathan Tom and Ronald W. Yeung. Nonlinear model predictive control applied to a generic ocean-wave energy extractor. *Journal of Offshore Mechanis and Arctic Engineering*, 136(4), 2014.

[97] Nathan Tom and Ronald W. Yeung. Experimental confirmation of nonlinear-model-predictive control applied offline to a permanent magnet linear generator for ocean-wave energy conversion. *IEEE Journal of Oceanic Engineering*, 41(2):281–295, 2015.

[98] Andreas Uihlein and David Magagna. Wave and tidal current energy - a review of the current state of research beyond technology. *Renewable and Sustainable Energy Reviews*, 58:1070–1081, 2016.

[99] US Army Corps of Engineers. *Costal Engineering Manual - Part II, Water Wave Mechanics. pp. 85-92.*

[100] A. Wacher and K. Neilsen. Mathematical and numerical modeling of the aquabuoy wave energy converter. *Mathematics-in-Industry Case Studies Journal*, 2:16–33, 2010.

[101] F. M. White. *Fluid Mechanics*, chapter 7, pages 450–483. McGraw-Hill Book Company, 2006.

[102] T. Whittaker, A. Lewis, and G. Thomas. Performance of the limpet wave power plant - prediction, measurement and potential:. In *5th European Wave Energy Conference Proceedings*, pages 97–104, 2003.

[103] A.S. Zurkinden, F. Ferri, S. Beatty, J.P. Kofoed, and M.M. Kramer. Non-linear numerical modeling and experimental testing of apoint absorber wave energy converter. *Ocean Engineering*, 2014.

Appendix A

A KALMAN FILTER FOR STATE OBSERVATION

Content from the following appendix can be found in the publication of Chapter 4 [30].

A Kalman filter can be used as a state observer for a system where the dynamics are imperfectly known. The filter uses the measured outputs of a system and an imperfect state model to determine a statistically significant estimate of the state dynamics. With proper adaptation, a Kalman filter can be used for parameter estimation as well as state estimation. The derivations of the Kalman filter used in this work can be found in [24].

While all numerical work requires debugging, several key issues needed to be resolved to successfully implement the extended Kalman filter for this work. The way the gain and update equations affect the radiation force states needed to be modified to ensure that small changes to the radiation states did not introduce unstable dynamics, this is discussed in Section 4.4.1. Section 5.4 describes a modification that is performed on the extended Kalman filter to ensure that the covariance matrix was symmetric. Finally a description of the method used to obtain the process noise covariance matrix for the WEC model is given in Section 5.4.3. Overcoming each of these three issues was vital to enabling state and parameter identification with this EKF for the point absorbing WEC models.

A.1 The Extended Kalman Filter

A nonlinear continuous time model with discrete time experimental data points can be observed using a Continuous-Discrete Extended Kalman Filter (EKF). The EKF is a nonlinear adaptation of the Kalman filter which observes a dynamic system in which zero-mean Gaussian white noise is assumed in both the dynamics and measurement. The model that is

observed by the extended Kalman filter is given by

$$\dot{\mathbf{x}}(t) = \mathbf{f}(\mathbf{x}(t), \mathbf{u}(t), t) + G(t)\mathbf{w}(t) \tag{A.1}$$

$$\tilde{\mathbf{y}}(t) = \mathbf{h}(\mathbf{x}(t), t) + \mathbf{v}(t) \tag{A.2}$$

where $\mathbf{f}$ is the nonlinear state dynamics, $\mathbf{h}$ is the nonlinear output function, $\mathbf{G}(t)$ is a vector that describes the noise of each state, $\mathbf{w}(t)$ is zero-mean Gaussian white noise with a variance $Q(t)$, and $\mathbf{v}(t)$ is zero-mean Gaussian white noise with a variance of $R(t)$. The states, $\dot{\mathbf{x}}(t)$, and output, $\tilde{\mathbf{y}}(t)$, are written in bold font to symbolize vector quantities. The tilde symbol, $\tilde{\bullet}$, modifier on the output represents that this is an experimentally measured quantity. Correct quantification of the process noise is essential for the EKF to function properly. However, determining the process noise is often left to design experience or intuition. Systematic approaches to understanding the noise parameters are discussed below. Since the EKF deals with nonlinear systems that must be integrated to determine state dynamics reasonable initial conditions must be used to ensure filter stability [24].

After the model and initializations are given the filter will begin to iterate through three steps known as the gain, update and propagation. A subscript k will be used to identify indexed variables that are being recomputed throughout the algorithm.
The Kalman gain is computed by

$$K_k = P_k^- H_k^T(\hat{\mathbf{x}}_k^-)[H_k(\hat{\mathbf{x}})P_k^- H_k^T(\hat{\mathbf{x}}) + R_k]^{-1} \tag{A.3}$$

where P_k is the noise covariance matrix and H is the linearized version of the output function described in (A.2). The superscript minus sign, $-$, represents an a priori value, meaning, values that are estimated by the previous step but prior to the update step. In the update step the Kalman gain and the experimental measurements are used to correct the states and covariances. The linearized output function, H_k, is first used in the gain step and therefore should be computed in this step if it has not already been computed.

The update step computes the a posteriori values of the states and covariance (signified with a superscript +). The Kalman gain and experimental measurements determine the aposteriori values with the equations

$$\hat{\mathbf{x}}_k^+ = \hat{\mathbf{x}}_k^- + K_k[\tilde{\mathbf{y}} - \mathbf{h}(\hat{\mathbf{x}}_k^-)], \tag{A.4}$$

$$P_k^+ = [\tilde{I} - K_k H_k(\mathbf{x}_k^+)]P_k^-[\tilde{I} - K_k H_k H_k]^T + K_k R_k K_k^T \tag{A.5}$$

where the hat notation, $\hat{\bullet}$, represents a value estimated by the EKF and I is the identity matrix with the dimension of the number of states in the system. Equation (A.5) is the Joseph stabilized version of the covariance update equation which is used when the stability of the covariance matrix is an issue. As a precaution (A.5) was used in the current work to ensure a positive semi-definite covariance matrix. The identity matrix I is given the $\tilde{I}$ notation to denote the block diagonal identity matrix that is described in section 4.

The propagation step is where the the states and noise covariance are integrated with a timestep small enough to ensure realistic model dynamics between the experimental measurements. The estimated state and covariance dynamics are computed by

$$\dot{\hat{\mathbf{x}}}(t) = \mathbf{f}(\hat{\mathbf{x}}(t), \mathbf{u}(t), t) \tag{A.6}$$

$$\dot{P}(t) = F(t)P(t) + P(t)F^T(t) + G(t)Q(t)G^T(t) \tag{A.7}$$

where F is the linearized state dynamics that is computed when needed in the propagation step. The gain, update and propagation steps are computed in a loop for every time step where an experimental datapoint is available. Estimated values are saved at each time step for use in postprocessing and comparison.

To use the EKF for system identification it is necessary to append an additional state to the first state dynamics. This appended state will have no dynamics and will only change as the result of the update step of the extended Kalman filter. By not including any dynamics, only the update step will result in a change in the estimated parameter.

The covariance matrix can be used to judge the certainty of the state measurements. The diagonal elements of the covariance matrix $P(t)$ are the variance of the estimated state value. A common use for the variance is to plot the 3 standard deviation, 3σ error bounds on each side of the estimated states. This is meant to show the 99.7% confidence interval that the "true" value lies within the error bounds. While the state estimations may appear to be very good when compared to smooth numerical data, there will always be a lower bound of the noise covairiance provided by the Cramér-Rao inequality given by $P \geq (H^T R^{-1} H)^{-1}$ [24]. Since the value of R is very small the 3σ confidence interval has the capacity to be very small. However, the covariance dynamics progress very slowly and the oscillating body velocity tends to keep the 3σ confidence interval relatively large.

A.2 Process Noise

The true process noise of a system is in reality unknown so it is typical to undergo a tuning process in order for Kalman filters to produce reasonable state estimates. To validate the process noise tuning process there are several tests to verify the effectiveness of Kalman filters. One such test is the "test for whiteness" which the error between measurement and estimated value is checked using an autocorrelation function. If the autocorrelation between the error and the measured data is low, then the error is considered only to be white noise, thereby verifying the filter. The consider Kalman filter is a method that bypasses the tuning of noise parameters by taking into account the error in the parameters and including these in the parameter covariance and gain calculations [24].

Another method of determining the noise parameters is to include the process noise values as a state in the dynamics. The modification that needs to be made when varying the process noise variance as an identified parameter is to ensure that the value is held constant during the propagation step when computing the covariance dynamics between time steps.

A.3 Fixed-Interval Smoother

To refine the estimates even further than the EKF a Rauch-Tung-Striebel (RTS) fixed-interval smoother can be used. The RTS filter essentially begins refining the estimate where the EKF ends, the smoother computes the dynamics and covariance beginning at the final time and proceeding to the initial time. After the EKF has finished looping through all of the measurement data the final state values are saved and used as the initial conditions of the RTS smoother. The RTS filter computes the gain, smoother covariance, and smoother estimate by

$$K_s(t) = G(t')Q(t')G^T(t')P^{-1}(t') \tag{A.8}$$

$$\dot{P}_s(t') = -\left[F(t') + K(t')\right]P_s(t') - P_s(t')\left[F(t') + K(t')\right]^T + G(t')Q(t')G^T F(t') \tag{A.9}$$

$$\dot{\hat{\mathbf{x}}}_s(t') = -\left[F(t') + K(t')\right]\left[\hat{\mathbf{x}}_s(t') - \hat{\mathbf{x}}(t')\right] - \mathbf{f}(\hat{\mathbf{x}}(t'), \mathbf{u}(t'), t') \tag{A.10}$$

respectively. The t' notation denotes that for the smoother the time span begins at the final time and ends at the initial time, and the subscript s denotes the smoother results of Kalman gain, covariance, and states. In addition to requiring all of the data to be collected an additional covariance and dynamics integration is required to implement the RTS smoother, making this a step only viable for post processing data. Since the purpose of this work is to observe the progression of identification from an initial guess to the true value, no smoothing algorithm is used.

A.4 Process noise Covariance

Since it is common to need to guess the process noise covariances of Kalman filters, or tune them to get reasonable or accurate state dynamics, the Kalman filter can have at times a great deal of ambiguity. To give a reasonable approximation or initial value for the process noise covariance, the following estimation is used.

Since a wave following wave energy converter tends to track very well with the surface of

a wave then the incident wave motion is used to quantify the process noise of the dynamic model. If a sinusoidal incident wave is applied to the WEC then the response of the WEC, if it is acting as a wave follower, will be sinusoidal with a magnitude very close to that of the input. With this in mind the standard deviation of the input wave is used as the standard deviation of the process noise for the position state. Since wave spectra actually have a Rayleigh distribution rather than a Gaussian distribution it was an approximation to directly use the standard deviation of the incident wave elevation. This approximation turns out in fact to be a reasonable starting point for a parameter that is ambiguous, and is not without precedent in literature [56]. For the standard deviation of the velocity state the input output relationship of a magnitude one sinusoidal wave to a magnitude of the output velocity was determined. Since the relationship of interest is an incident wave displacement to the output a WEC velocity the amplitude response between the two is used to scale the standard deviation of the incident wave position and this value is used for the velocity. In the development of this work this relationship was found to be 5/2, meaning that for a 1 meter sinusoidal input wave the body velocity will be sinusoidal with an amplitude of $\frac{5}{2}\frac{m}{s}$. This amplitude response was found by simulating a regular wave input to the WEC model with a sufficiently long timespan to ensure that the transient response was no longer influencing the dynamics. The standard deviation of the input wave elevation was calculated using the time domain data collected in [13]. If the input-output transfer function is needed, [32] provides a discussion on linearizing WEC equations of motion to determine the WEC transfer function.